JEOL news

0.01

0.10

1.00

Interface Studies by Cs-Corrected STEM

Yuichi Ikuhara[†,††,†††], Naoya Shibata[†], Teruyasu Mizoguchi[†]
and Takahisa Yamamoto[†,††]

[†]Institute of Engineering Innovation, The University of Tokyo
[††]Nanostructures Research Laboratory, Japan Fine Ceramics Center
[†††]WPI Advanced Institute for Materials Research, Tohoku University

Contents

Cover micrograph

HAADF-STEM image of Y-doped Σ31 [0001] tilt grain boundary in alumina, taken with JEM-2100F with Cs corrector (top) and an electron density map around Y atoms segregated in Σ31 Al_2O_3 grain boundary, obtained by the first principles calculation (bottom). (See page 4)

Introduction

Grain boundaries and interfaces of crystals have peculiar electronic structures, caused by the disorder in periodicity, providing the functional properties, which cannot be observed in a perfect crystal [1, 2]. In the vicinity of the grain boundaries and interfaces around the order of 1 nanometer, dopants or impurities are often segregated, and they play a crucial role in the material properties. We call these dopants "function providing elements", which have the characteristics to change the macroscopic properties of the materials drastically.

To obtain a guideline for designing material by the atomic scale modification, an understanding of the atomistic mechanism for the functional properties is required as well as precise measurement of the state of trace elements segregated in the nanoscale region. In recent nano-characterization technologies, there has been remarkable progress by Scanning Transmission Electron Microscopy (STEM) utilizing the spherical aberration (Cs) corrector [3]. The technique enables us not only to identify the location of the dopants but also to analyze the local electronic state for the single atomic column on grain boundaries and interfaces. In this paper, we focus our attention on grain boundaries and interfaces of various ceramics, to which "function providing elements" are doped, and introduce our latest results of the microstructure analysis by STEM. Furthermore, by the first principles calculation based on these observation results, the mechanism of the "function providing elements" will be described as well.

2-11-16 Yayoi, Bunkyo-ku, Tokyo 113-8656, Japan

E-mail: ikuhara@sigma.t.u-tokyo.ac.jp

Scanning Transmission Electron Microscopy (STEM)

STEM is a technique to scan a specimen by an electron probe, which is focused down to 1 nm or less on the sample. The STEM image is formed with the collected scattered electrons in each probe position by the Annular Dark Field (ADF) detector at the bottom of the sample on the monitor in synchronism with the scanning probe [4]. The atomic resolution image can be obtained by focusing the electron probe down to below the atomic column interval. The advantages of this method are those: there is no inversion of the image contrast with the defocusing and the change in the sample thickness, and thus the positions of the atomic columns can be determined directly from the image. These excellent characteristics are very useful to determine the complicated atomic structures in the grain boundaries and interfaces. In addition, the intensity of the image obtained by detecting the electrons scattered to higher angles is known to correspond to approximately the square of the atomic number Z. The contrast of High Angle Annular Dark Field (HAADF)-STEM is therefore called "Z-contrast" as well, making it possible to observe the element distribution at an atomic column level in the region where local composition is changed. **Figure 1** shows an example of HAADF-STEM image for $SrTiO_3$ projected along the [001]. As seen in Fig. 1, the contrast of Sr atoms (Z=38) is brighter than that of Ti atoms (Z=22), which indicates that atomic species can be discriminated in the one image. Moreover, in recent years, by combining STEM method with the Cs correction technology, drastic improvement in resolution has become possible. At present, with the STEM using the Cs corrector, the electron probe diameter of 0.1 nm or less has been already

Fig.1 HAADF-STEM image of SrTiO$_3$ projected along the [001] direction, in which the contrast of Sr atoms (Z=38) is brighter than that of Ti atoms (Z=22).

achieved [5]. Furthermore, since the intensity of the electron probe can be increased by the Cs correction technology, there are advantages that the S/N ratio of the STEM image will be increased and hence the image quality also can be improved drastically. STEM method using the Cs corrector is thus expected as a powerful tool to characterize the atomic structures in grain boundaries and interfaces.

Grain Boundary of Pr-doped ZnO Varistor[6, 7]

As an example of the grain boundary segregation in electroceramics, Pr doped ZnO grain boundary is shown in this section. Since ZnO ceramics show high nonlinear current-voltage characteristics by doping secondary elements such as Pr and Bi, they are widely used for varistors. It has been reported that Pr and Bi etc., doped to ZnO ceramics segregate in grain boundaries and it is believed that they have an important role for providing varistor properties. However, their segregation behaviors have not been understood in detail at an atomic level. It is therefore required to characterize an atomic level analysis of the Pr segregation in ZnO grain boundaries to clarify the atomistic mechanism of the varistor properties.

Figure 2 shows a HAADF-STEM image of the Pr-doped Σ7 grain boundary (JEOL JEM-2100F (200 kV) with Cs corrector (CEOS), Univ. Tokyo) [6]. Here, Σ represents the degree of geometrical coherency at grain boundaries [1]. The small Σ number indicates high coherency, and the large Σ number indicates low coherency at grain boundaries. As described above, in HAADF-STEM image, the atomic column position emerges as white dots. Pr that has the higher atomic number than Zn, shows the brighter contrast. Accordingly, the

Fig.2 HAADF-STEM image of Pr-doped ZnO Σ7 grain boundary, showing that Pr segregation sites can be observed as bright spots indicated by the arrows [6].

Fig.3 The stable atomic structure of Pr-doped ZnO Σ7 grain boundary obtained by the first principles calculation (green circle: O, blue circle: Zn, red circle:Pr) [7].

bright spots, indicated by the arrows at the grain boundary, show the segregated Pr atoms. It can be recognized from the image that Pr does not have the wide distribution but segregates only at the special atomic sites. With substit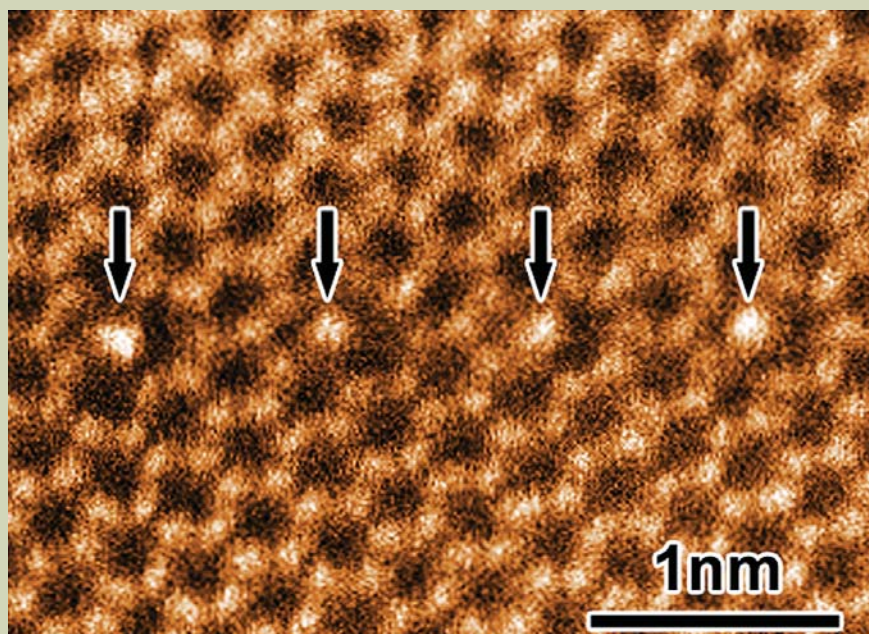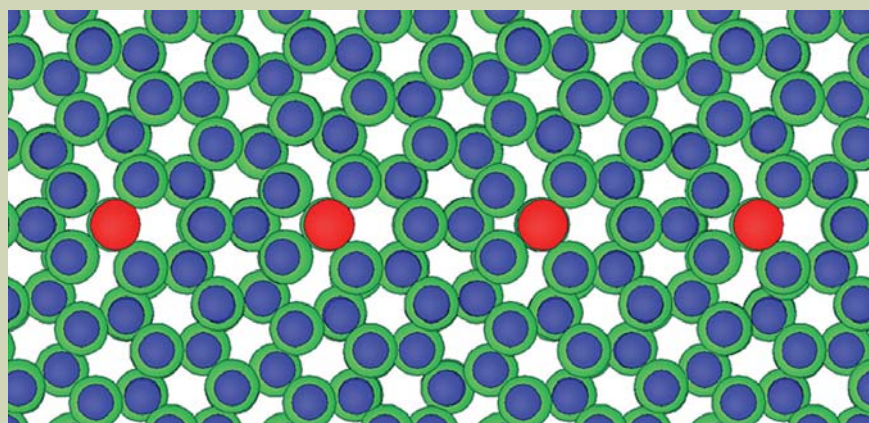uting Pr atoms, suggested from the HAADF-STEM image, to the Zn sites in the Σ7 grain boundary, the most stable atomic structure was calculated by the first principles method as shown in **Fig. 3** [7]. It is confirmed from Fig. 3 that the experimentally observed Pr atoms segregate to the most stable position in the grain boundary. In addition, by the systematic first principles calculations, it was found that due to Pr presence in the grain boundary, acceptor type defects such as Zn vacancy and interstitial O atom are easily formed as well [6, 7]. These defect formations must be related with the mechanism of the varistor properties, which is believed to be an important role of Pr addition. Furthermore, it has been shown by the similar calculations that Pr segregates preferentially at the Zn sites (the locally tensile sites), in which the bonding length at the grain boundary is long [7].

Grain Boundary of Y-doped Alumina Ceramics[8]

It has been known that the high temperature strength of alumina ceramics is improved drastically by doping small amount of rare earth elements such as Y and Lu [8, 9]. Although it has been proposed that these minor doping elements segregate in the grain boundaries in the alumina polycrystal and prevent grain boundary sliding at high temperature, there are many unknown issues regarding the intrinsic mechanism yet. Here, the grain boundary structure of the Y-doped alumina was observed by STEM method. The results demonstrate the grain boundary strengthening mechanism by Y. **Figure 4** shows HAADF-STEM image of the Y-doped Σ31 alumina grain boundary (JEOL JEM-2100F (200 kV) with Cs corrector (CEOS), Univ. Tokyo) [8]. Here, Σ31 grain boundary can be classified into a general grain boundary. It can be recognized that very strong contrast is observed at the particular atomic sites along the grain boundary. It corresponds to the position of Y atoms segregated in the grain boundary cores, which indicates that Y atoms segregate selectively and periodically only at the special sites in the grain boundary cores. **Figure 5** shows the results of the theoretical analysis by the first principles calculation based on this structure, showing the electron density distribution around the Y atoms segregated in the center of the seven member ring [8]. From Fig. 5, it is recognized that the electron distribution is oriented around Y atoms to form covalent-like chemical bonds in the seven member ring, which is confirmed to be significant by comparing with the fact that the bonds without segregation are mainly ionic bonding [8]. In this way, it has become evident that due to the segregation of rare earth elements in the grain boundaries, surrounding chemical bonds change drastically, which has the effect to improve the grain boundary strength. In other words, it is believed that the effect of rare earth element doping to alumina ceramics is originated from the change in the local chemical bonding state at the grain boundary.

Dislocation Structure of Sapphire[10]

To understand the mechanical properties of sapphire, many studies have been performed for the dislocations so far. It has been shown that the basal dislocation is dissociated to two partial dislocations. However, there are many unknown matters concerning the structure at the atomic level, and the atomistic mechanism of dislocation glide has not been quantitatively understood yet. Since sapphire is composed of Al and O, an analysis of sublattice including the oxygen is required to understand its dislocation core structure at the atomic level. Therefore, using the Cs-corrected STEM, the dislocation core structure including the oxygen column was directly observed by combining BF and HAADF-STEM techniques.

Figure 6 shows (a) the crystal structure model of sapphire crystal viewed from [1$\bar{1}$00] direction, (b) the HAADF-STEM and (c) the Bright Field (BF) STEM images (VG HB603U STEM (300 kV) with Cs corrector (Nion), ORNL) [10]. By STEM, the BF and the HAADF image can be obtained from the same area simultaneously. As shown in the
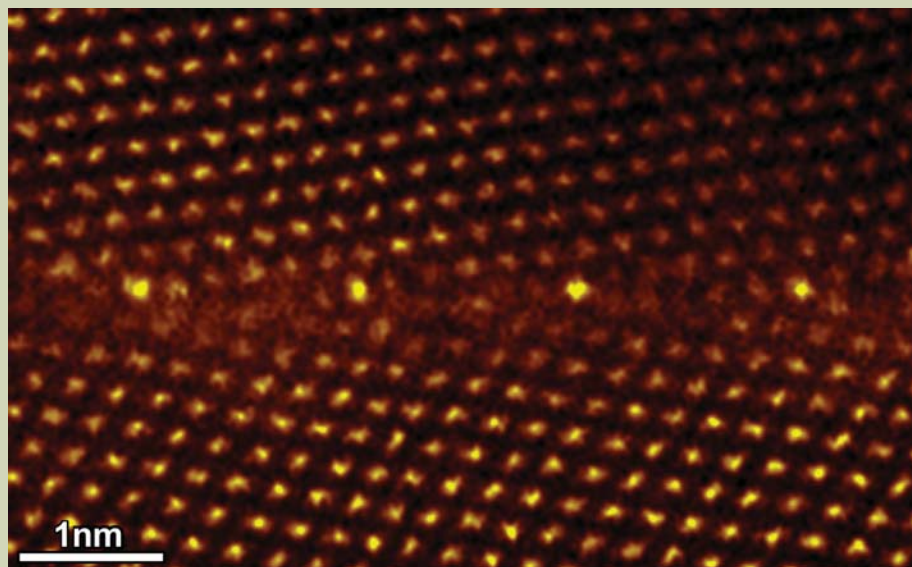

Fig.4 HAADF-STEM image of Y-doped Σ31 [0001] tilt grain boundary in alumina. The brightest columns indicate the presence of the heavy Y ions.
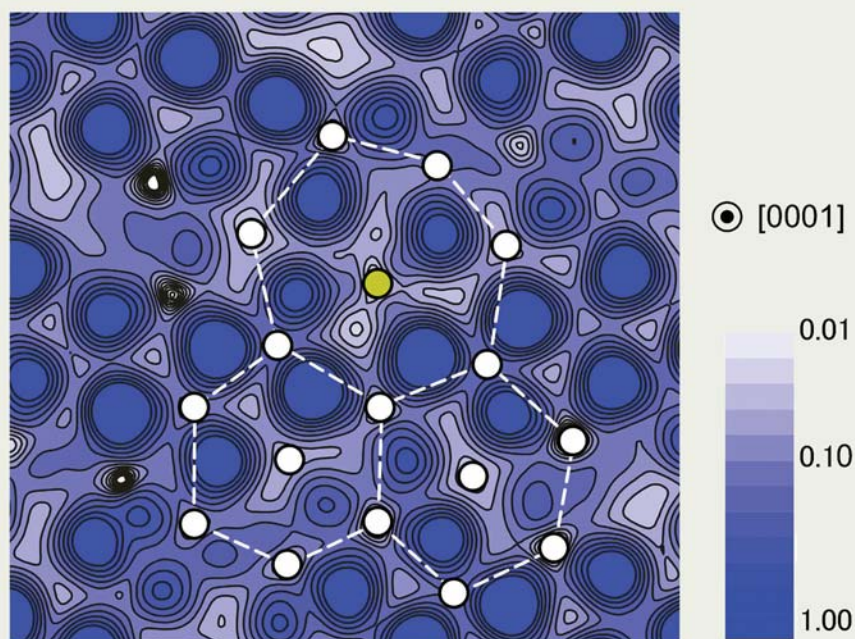

Fig.5 Electron density map around Y atoms segregated in Σ31 Al$_2$O$_3$ grain boundary, which was obtained by the first principles calculation [8].

crystal structure model, the atomic columns of Al and O can be distinguished with the present incident axis. In the HAADF-STEM image shown in (b), the positions of the O columns and the Al columns are apparently discriminated. Although the S/N ratio of the HAADF-STEM image is lower than the one of the BF-STEM image of (c), the atom position can be determined directly, since the image is the image under incoherent conditions. On the other hand, the S/N of the BF-STEM image is pretty high, and the BF-STEM image is optically equivalent to the image obtained by high-resolution transmission electron microscopy

(HRTEM) due to the reciprocity theorem. Although, the contrast of BF-STEM image varies widely according to the defocusing and the thickness of the sample, accordingly, by taking the BF-STEM image and the HAADF-STEM image simultaneously to compare their contrast, the correspondence of the contrast of the BF-STEM image and the atom position can be determined directly. Under the present observation condition, the position of the bright contrast in the BF-STEM image directly corresponds to the atomic column position. The structure determination including so far as the light element like oxygen thus becomes

possible by simultaneous observation utilizing the image formation by both HAADF and BF STEM imaging.

The basal dislocation of sapphire has the Burgers vector of $\mathbf{b}=1/3<11\bar{2}0>$, but it has been confirmed that the dislocation core is dissociated by climb mechanism along the [0001] direction and is composed of partial dislocations of $\mathbf{b_1}=1/3<01\bar{1}0>$ and $\mathbf{b_2}=1/3<10\bar{1}0>$ and stacking faults on the {11$\bar{2}$0} plane [11]. **Figure 7** shows the BF-STEM image of each dislocation edge of the dissociated partial dislocations (VG HB603U STEM (300 kV)). In the BF-STEM image, since the oxygen column
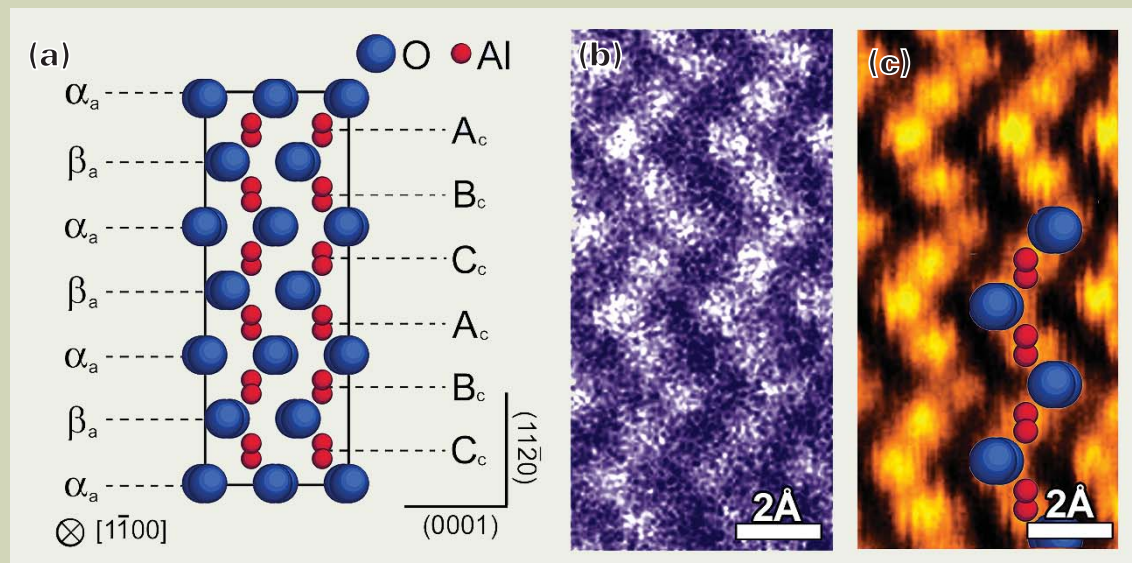

Fig.6 (a) Atomic structure model of sapphire projected along [1$\bar{1}$00] direction, (b) HAADF and (c) BF- STEM images of a sapphire single crystal viewed from [1$\bar{1}$00] direction [10].
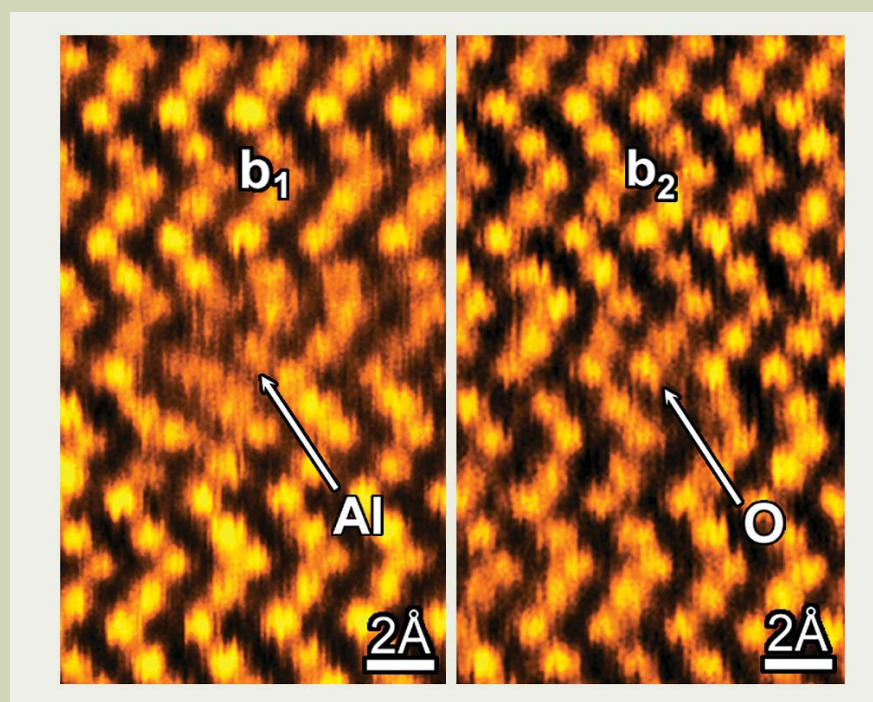

Fig.7 BF-STEM images of the core structures of the dissociated basal dislocations (b₁ and b₂), indicating that each core terminates at Al and O, respectively [10].

and the aluminum column can be identified, the atomic columns at the dislocation edge can be directly determined. As apparent from the experimental image, two partial dislocations terminate at the aluminum and the oxygen atomic columns, respectively. It is thus shown that each partial dislocation core has the structure with local composition shift of aluminum surplus or oxygen surplus from the stoichiometric ratio.

In case of ionic crystals, although the structure like this has been considered to be energetically unstable, the present results first demonstrate that the nonstoichiometric local structure can exist in the crystal. If the perfect dislocation is composed of two partial dislocations, the stoichiometric ratio is satisfied in total. In other words, the stoichiometry is maintained when the basal dislocation glides. By the direct observation of the dislocation core structure like this, the gliding mechanism of the basal dislocation of sapphire can be understood [10], which will bring a great breakthrough to the study of ceramics dislocation in future. The development of the new functional materials utilizing the ceramics dislocation also has already developed [12]. It is expected that STEM observation, which combines the BF image with the HAADF image, will become a useful method in future.

Interface Structure of SrTiO₃/Nb-SrTiO₃/SrTiO₃ Superlattice[13]

It has been known that some oxide superlattices can be used as thermoelectric device. For example, a high-density two-dimensional electron gas confined within a unit cell layer thickness (0.3905 nm) in $SrTiO_3$ exhibits high thermoelectric properties, which is about 5 times larger than that of the bulk $SrTiO_3$ [13].

Figure 8 shows HAADF-STEM image of the $SrTiO_3$/Nb-doped $SrTiO_3$/$SrTiO_3$ superlattice film (JEOL JEM-2100F (200 kV) with Cs corrector (CEOS), Univ. Tokyo) [13]. As described above, it is recognized that Sr (Z=38) columns are observed brightly compared with the Ti (Z=22) columns in $SrTiO_3$. In this case, Nb-doped $SrTiO_3$ layers are observed at every 24 unit cell as stripe contrast (Fig. 8(a)). Figure 8 (b) and (c) show the magnified HAADF-STEM image around the Nb-doped $SrTiO_3$ layer and a line profile of the image intensity of the Sr atomic row and the Ti atomic row in the same region. From these figures, it is recognized that the image intensity does not change in the Sr atomic row; however, the image intensity becomes high in the Ti atomic row at the Nb-doped $SrTiO_3$ layer. Taking into consideration that the atomic number of Nb is 41, it is considered that Nb exists at the Ti sites by substitution. On the other hand, since the atomic numbers of Nb and Sr are close, whether Nb exists in the Sr sites or not cannot be judged only by the contrast of the HAADF-STEM image. Then, the solution energy of Nb was calculated by the first principles PAW (Projector Augmented-Wave) method. It is then clarified that the solution energy of Nb to the Sr sites is 7.6 eV higher compared with the one to the Ti sites. This result also shows the solubility of Nb to the Ti sites.

Figure 9 shows the spectra of Ti-$L_{2,3}$ ELNES (Energy Loss Near Edge Structure) obtained from the $SrTiO_3$ layer and the Nb-doped $SrTiO_3$ layer in the $SrTiO_3$/Nb-doped $SrTiO_3$/$SrTiO_3$ superlattice. The upper figure corresponds to the experimental spectra, and the bottom figure corresponds to the theoretically calculated spectra. Although four peaks (t_{2g}, e_g split) are apparent in the spectra obtained from the $SrTiO_3$ layer, it is recognized that the peaks are broadened in the spectrum from the Nb-doped $SrTiO_3$ layer. Comparing the theoretical ELNES calculated by the first principles relativistic multi-electron method with the experimental ELNES, it is found that the change in the experimental spectra is due to the transition from Ti^{4+} to Ti^{3+} which is accompanied by the Nb doping.

Direct Observation of Li ion site in lithium battery[14]

Li battery is widely used for the battery of cellular phone and personal computer. Recently, it is also intensively studied for the application of the automobile battery. The properties of Li battery is strongly dependent on the positive electrode active material, and cobalt or nickel-compounds such as $LiCoO_2$ or $LiNiO_2$ have been mainly used as industrial products so far. However, it has been pointed out that they have problems on the stability, lifetime and reliability. $LiFePO_4$ with the stable olivine structure is therefore expected as the lithium battery for the next generation. Since the properties of the positive electrode active material is related to the behavior of Li ions in the crystal, direct visualization of Li site is needed to understand the mechanism of the properties. But, it is impossible to directly observe Li atoms even by HAADF-STEM technique because the atomic number 3 for Li is too small to scatter electrons. We therefore exchanged a part of Li sites with Fe atoms in
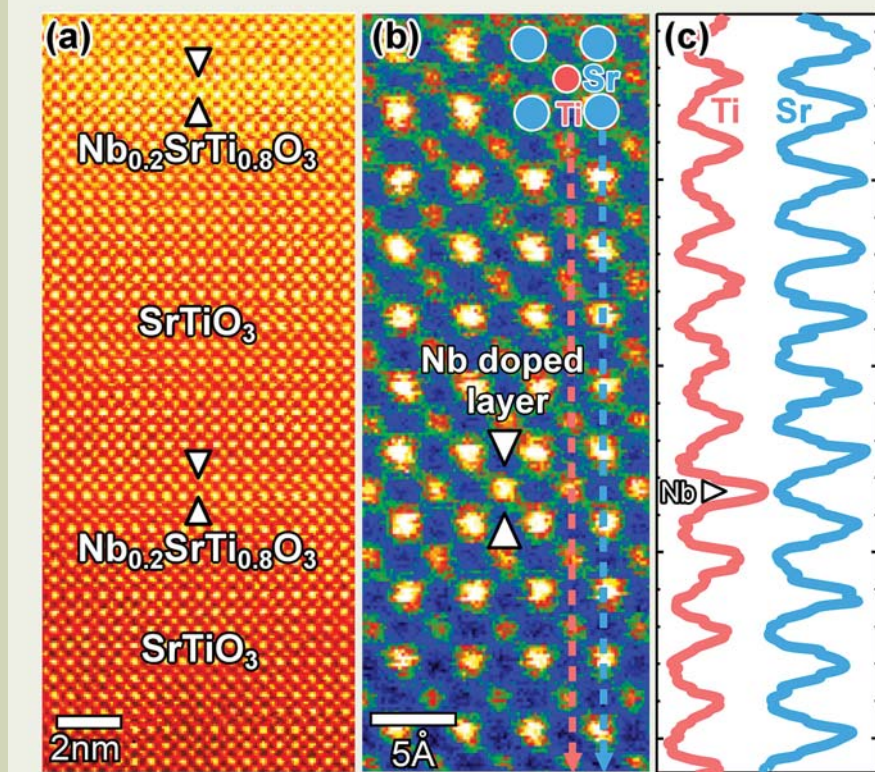

Fig.8 (a) HAADF-STEM image of SrTiO₃/ Nb-SrTiO₃ superlattice, (b) magnified image of the region (a) and (c) image intensity profile of Ti and Sr layers [13].

LiFePO$_4$ crystal by chemical modification-annealing technique, and tried to directly observe the Li sites by HAADF-STEM. **Figure 10** shows HAADF-STEM image for the LiFePO$_4$ crystals observed along the [010] direction (JEOL JEM-2100F (200 kV) with Cs corrector (CEOS), Univ. Tokyo). In the sample, about 15% of Li sites were substituted by Fe atoms [14]. In Fig. 10, the model crystal structure composed of Fe, Li, P, O is shown, and the inset shows the simulated HAADF image for the olivine with 15% Li-Fe exchange. As can be seen in the image, Li sites, which is substituted by Fe atoms, can be observed as weak spots in the center of hexagonal framework composed of Fe and P. It is also found that such exchange defects appear to be locally aggregated rather than homogeneously dispersed in the crystal. In addition, the distribution of the exchange defect was not homogeneous in the vicinity of the grain boundaries, which indicates that the direct visualization of Li sites will clarify the behavior of lithium ions, conductor and breakdown mechanism of lithium battery in the future.

Conclusion

Various kinds of dopants have been used for industrial materials to improve the functional and mechanical properties. However, many of such dopants have been considered and selected on the basis of the long-term experience and empirical background, and it is hence unclear for the effect of the function providing dopants on the atomistic mechanism. If the atomistic mechanism can be fully understood, it will be possible to reasonably design material by controlling atoms, electrons and function providing elements in the materials. The appearance of Cs corrected STEM enables us to determine the location of the dopants and the local electronic state at a single atom level.

In this paper, we introduced our recent results obtained for ceramic grain boundary and interface by Cs corrected STEM. Several examples are demonstrated for the gain boundaries of varistor and structural ceramics, dislocation in alumina, oxide superlattice, lithium battery and so on. These results indicate that the atomistic mechanism of the properties can be unraveled by the combination of STEM characterization and the first principles calculations. This approach must be a breakthrough for new materials science and engineering in the next generation.

Acknowledgements

References

[1] Y.Ikuhara Ed. "Physics of Ceramics" Nikkan-Kogyo -Shinbun Pub.Co. (1999).
[2] Y.Ikuhara, *J.Ceram.Soc.Jpn.,* **110,** 139 (2002).
[3] M. Haider, H. Rose, S. Uhlemann, B. Kabius and K. Urban, *J. Electron Microsc.,* **47,** 395 (1998).
[4] S. J. Pennycook and D. E. Jesson, *Phys. Rev. Lett.,* **64,** 938 (1990).
[5] P.D. Nellist, M.F. Chisholm, N. Dellby, O.L. Krivanek, M.F. Murfitt, Z.S. Szilagyi, A.R. Lupini, A.Y. Borisevich, W.H. Sides and S.J. Pennycook, *Science,* **305,** 1741 (2004).
[6] Y. Sato, J. P. Buban, T. Mizoguchi, N. Shibata, M. Yodogawa, T. Yamamoto, and Y. Ikuhara, *Phys. Rev. Lett.,* **97,** 106802 (2006).
[7] Y. Sato, T. Yamamoto and Y. Ikuhara, *J. Am. Ceram. Soc.,* **90,** 337 (2007).
[8] J.P. Buban, K. Matsunaga, J. Chen, N. Shibata, W.Y. Ching, T. Yamamoto and Y. Ikuhara, *Science,* **311,** 212 (2006).
[9] H.Yoshida, Y.Ikuhara and T.Sakuma, *Acta.Mater.,* **50,** 2955 (2002).
[10] N. Shibata, M.F. Chisholm, A. Nakamura, S.J. Pennycook, T. Yamamoto and Y. Ikuhara, *Science,* **316,** 82 (2007).
[11] A. Nakamura, T. Yamamoto and Y. Ikuhara, *Acta Mater.*, **50,** 101 (2002).
[12] A.Nakamura, K.Matsunaga, J.Tohma, T.Yamamoto and Y.Ikuhara, *Nature Mater.,* **2,** 453 (2003).
[13] H. Ohta, S.W. Kim, Y. Mune, T. Mizoguchi, K. Nomura, S. Ohta, T. Nomura, Y. Nakanishi, Y. Ikuhara, M. Hirano, H. Hosono and K. Koumoto, *Nature Mater.*, **6,** 129 (2007).
[14] S-Y Chung, S-Y Choi, T.Yamamoto and Y.Ikuhara, *Phys.Rev.Lett.,* **100,** 125502 (2008).
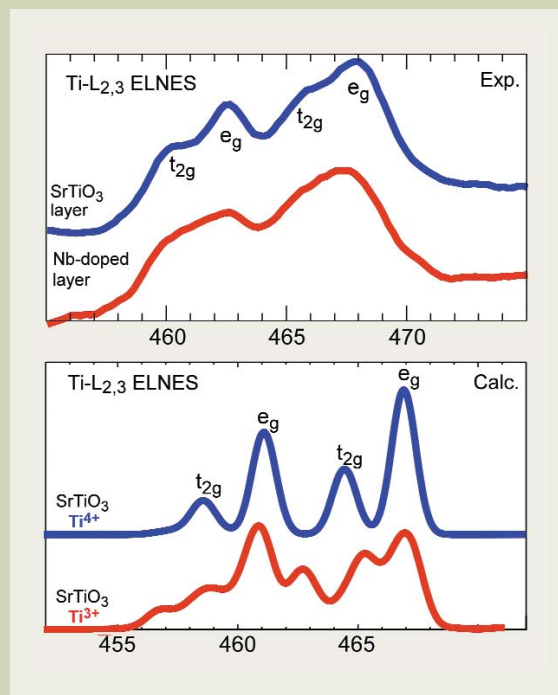
Fig.9 (top) Experimental and (bottom) theoretically calculated Ti-L$_{2,3}$ ELNES obtained from the SrTiO$_3$ layer and the Nb-doped SrTiO$_3$ layer in the SrTiO$_3$/Nb-doped SrTiO$_3$ superlattice. The calculations were made by the first principles relativistic multielectron method.
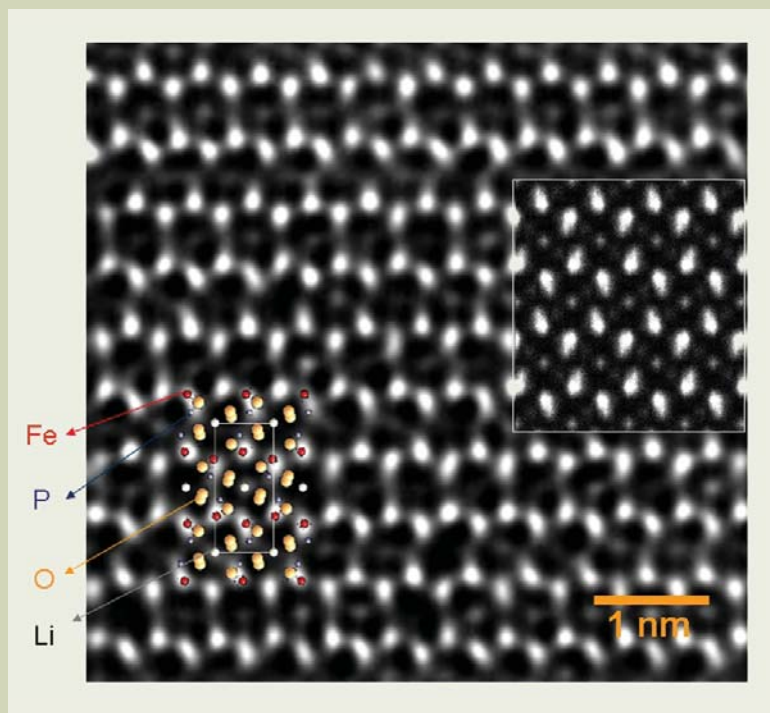
Fig.10 HAADF-STEM image for the LiFePO$_4$ crystals, in which a part of Li sites was substituted by Fe atoms, showing that some of the Li columns have a bright contrast in significant intensity [14]. The inset shows the simulated HAADF image for the olivine with 15% Li-Fe exchange.

Field Emission AES Characterization of Corrosion Products Formed on Copper in Chloride Containing Solutions

Y. Van Ingelgem, I. Vandendael, J. Vereecken, H. Terryn and A.Hubin

Vrije Universiteit Brussel V.U.B.
Dept. Metallurgy, Electrochemistry and Materials Science
Materials and Chemistry Group

During the first 24 h of immersion of a pure copper surface in a NaCl containing solution, this surface is in constant evolution. The reactions going on the surface are still not known; discrepancies are found between different studies published. This work uses Field Emission Auger Electron Spectroscopy to localize and identify the reaction products that can be formed on copper surfaces in this type of environments. Identification was based on identification of elements. A more profound analysis of the compounds present on the surface was performed by applying Target Factor Analysis on the recorded spectra

Introduction

The first 24 hours it is immersed in a 0.5 M NaCl solution, a copper surface undergoes a series of transformations. A corrosion product layer is formed that acts as a barrier layer between the aggressive solution and the substrate, offering some protection to the material. This barrier layer itself is subsequently attacked and localized corrosion is observed. The evolution can be divided into three stages. In the first hour, a homogeneous corrosion layer is formed over the entire surface. In the next hours, the thickness of this layer keeps on increasing. After two hours local corrosion starts to appear, piercing the formerly grown oxide layer in certain places. This attack is localized mostly at the grain boundaries. After 20 hours of immersion almost all these local attack sites gradually get covered anew by the constantly growing corrosion product layer. Electrochemical Impedance Spectroscopy (EIS) studies conducted on these surfaces generate a response that is a combination of the response of both reactions, making it impossible to discriminate between global and local reaction properties [1,2]. Knowing the reaction products present on different parts of the surface would however represent a great deal of information if one needs to identify the reactions taking place on this surface.

Extensive studies have already been carried out on these surfaces, but still some lack of clarity remains, illustrated by some yet unidentified features in electrochemical impedance spectra (EIS) recorded on these surfaces[1,2,3]. From the various works it

Pleinlaan 2 1050 Brussels Belgium

E-mail: yvingelg@vub.ac.be

becomes clear that multiple species have been identified to form on the surface. Among them Cu_2O [4-8] CuCl [5,6,8,9-13] or CuO [14-19]. Auger spectroscopy was already used in various works dedicated to the study of copper corrosion. A number of papers has been published on the identification of copper oxides, formed on various substrates [20-23]. Also a limited amount of literature exists on the identification of copper chlorides [24]. Lineshape analysis was used in a number of works as a tool to discriminate between different copper compounds, concentrating however on thermally formed oxides and chloride compounds grown in modified vacuum conditions.

The study presented in this work uses Field Emission AES (FE-AES) to identify different copper compounds on the same surface. All of these were formed during the corrosion process of copper in aqueous chloride containing solutions. Lateral distributions of the composition were visualized by Auger imaging. Identification of the compounds was done by comparing the recorded high resolution FE-AES spectra on corroded surfaces with spectra obtained from reference materials. With the acquired reference spectra Target Factor Analysis (TFA) was carried out to analyze the chemical composition of the corrosion products. Both the in-depth product distribution in the uniform corrosion layer and the distribution of the products in and around a local corrosion site were studied.

Experimental

Surface analysis was done using a JEOL JAMP-9500F scanning Auger microprobe. Settings were such that an electron beam of 10 kV and 1 nA at an angle of incidence of 30 with respect to the sample surface normal was applied. Measurements were performed using an energy resolution dE/E of 0.06 % . The spectra during depth profiles and line profiles were obtained using a step of 0.1 eV. When carbon was detected at the surface, the materials were sputtered with the attached ion gun for several seconds using 1 keV Ar^+-ions in order to remove the impurities. Depth profiles were obtained using 1 keV Ar^+-ions. The ion gun was calibrated on Ta/Ta_2O_5 samples and had a sputter rate of 3nm/min. The spectra were corrected for the work function of the equipment (ef = 4.5 eV). Signal intensities were calculated by subtracting the peak signal from the background signal in the direct spectrum.

SEM images were obtained using the secondary electron detector attached to the FE-AES.

Chemical reagent products from different producers were used as reference materials: Pro Analysi CuO from Merck, 99.99 % pure Cu_2O from Aldrich and Pro Analysi CuCl from Merck. All were under the form of small crystals or powder. The reference material samples were obtained by pressing the powder or crystals into very soft polished Electrolytic Tough Pitch (ETP) copper obtained from Cumerio (Olen BE). Reference spectra of copper were obtained from the very pure ETP copper.

The material studied was a 99.9 % pure copper, obtained from Goodfellow. Samples were cut from a 20.6 mm diameter rod. Prior to attack the samples were prepared by a metallurgical procedure [25]. This was polishing subsequently with 320 grit SiC paper, 9 and 3µm diamond paste and finally 0.04 µm colloidal silica.

The samples were immersed in 0.5 M NaCl solutions for various periods of time. The solvent was deionized and non-deaerated water.

Fig.1 Cu LVV AES spectra recorded on different reference samples.

Fig.2 a and b SEM image of a copper surface after1 and 3 hours of immersion in a 0.5 M NaCl solution.

Fig.3 Evolution of corrosion product layer thickness after different immersion times in the NaCl solution.

Results and Discussion

Cu LVV spectra on different copper compounds are shown in **Figure 1** The analysis of the compounds present on the corroded copper surface was based on reference spectra obtained from various reference materials, as mentioned in the experimental part. The spectra presented here were subsequently used in the TFA procedures applied to derive the chemical composition in different points on the surface. It was chosen to perform the TFA analysis using the Cu spectra as this element is the only one present in all compounds expected to be found on the surface. Besides, these spectra showed also the most visible difference in peak shape when comparing different compounds.

The spectrum of pure copper is the sharpest, presenting 4 distinguishable contributions in the energy window of interest. The copper chloride presents the broadest peak found. Both copper oxides generate a single peak contribution, somewhat broader than the pure copper main peak, but with a maximum at clearly different energy positions.

Figure 2 a and b show a SEM image of the copper surface after 1 and 3 hours of immersion in the 0.5 M NaCl solution. Images of copper surfaces formed after different times of immersion show the same tendency: the surface undergoes local and global attack at the same time. Global attack creates a corrosion product layer, somewhat porous in nature. Local attack is more severe and creates holes in the surface. In these holes also a corrosion product layer is formed. Depth profiles recorded on both types of location show that the general corrosion layer is thicker than the one formed inside local attack sites.

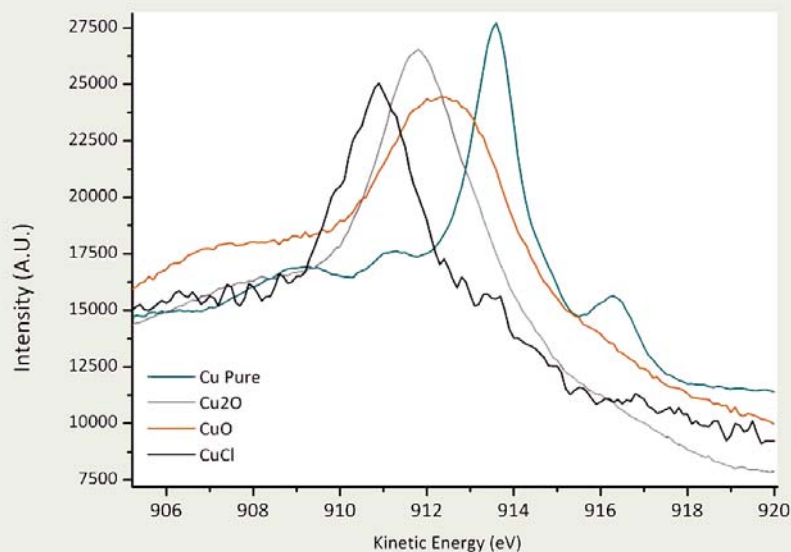**Figure 3** shows the thickness of the general

Fig.4 In depth evolution of the composition of a corrosion product layer. This surface has resided for 7 hours in the NaCl containing solution.
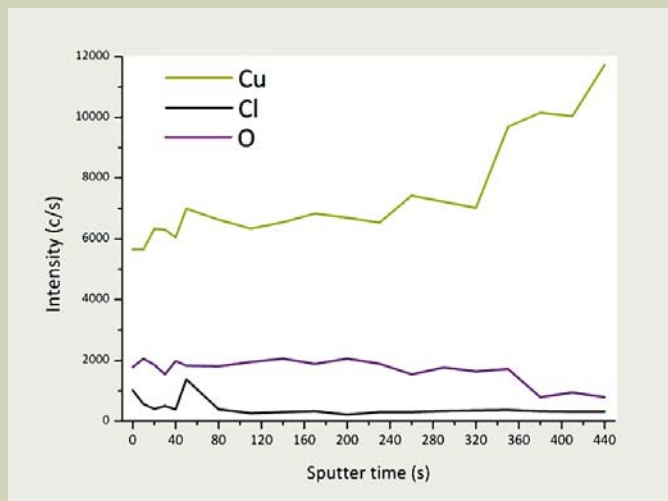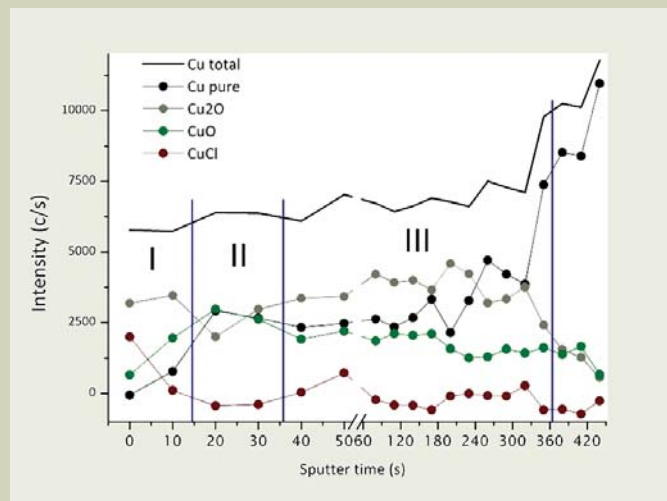

Fig.5 Result of the TFA analysis of the Cu LVV spectrum recorded in Fig. 4.

corrosion product layer formed after different immersion times in the NaCl solution. From the evolution, it can be concluded that the layer thickness increases with time.

Also a high resolution depth profile was recorded on a corroded copper surface. **Figure 4** shows the evolution of the composition evolution resulting from a depth profile obtained from the general corrosion layer. This layer was formed on a copper surface immersed during 7 hours in the chloride containing solution. From this figure it is clear that, in the general corrosion product layer, chloride is only present in the outermost layers. Deeper in the layer only copper and oxygen can be identified. After sputtering for a longer time, also the oxygen signal intensity decreases to zero.

Figure 5 shows the results of the TFA analysis performed on the Cu LVV spectrum recorded in the depth profile of Figure 4. As mentioned before, the spectra shown in Figure 1 were used as factors in this analysis. From the calculations it became clear that the corrosion product layer can be divided into 3 zones, as indicated on the figure. Most of the layer is represented by zone III. This zone, situated closest to the pure metal, consists of mostly Cu_2O, but CuO can be found as well. Above this zone, a zone with a very high CuO content is found. Zone I, the outermost layer, knows a very high content of copper chlorides. This is in line with the composition depth profile in Figure 4 and indicates the reliability of the TFA analysis performed.

Over the entire thickness of the corrosion product layer also a pure Cu contribution is present. This presence is attributed to the porous nature of the corrosion product layer.

A more detailed study of the lateral distribution of corrosion products over the surface was performed by recording spectrum line profiles that span global corrosion layers as well as local attack sites. The intensity line profile on a copper surface after 6 hours of immersion in the 0.5 M NaCl solution as well as the location where it was recorded can be found in **Figure 6**. To remove carbon contamination from the surface, a light sputtering was applied to the surface before performing the measurement. This treatment however also removed the very thin layer of copper chloride components that was present on the surface. Depth profiles performed on this sample showed that less chlorides were present than on the sample in figure 4, as the immersion time was shorter. The line profile shows nevertheless the presence of higher concentrations of chlorides in and around local attack sites.

The results of the TFA analysis performed on the Cu LVV spectrum recorded in this experiment are shown in **Figure 7**. In points on the general corrosion layer on the surface only 2 contributions can be identified by the analysis: a major contribution of Cu_2O and a less prominent amount of CuO. The places where local corrosion has taken place are indicated by an arrow in Figure 6. In these locations the composition differs significantly from the one at the general corrosion layer.

A first observation is the dominating presence of a pure copper contribution at the edges of the local attack sites. This can be attributed to the high speed nature of the local attack, resulting in the formation of very thin layers of corrosion products at these locations. In the local attack sites copper chloride compounds are found as well, as could be expected from the composition line profile shown in Figure 6. CuO and Cu_2O are also present in the local attack sites. The relation between both compounds differs however from the one on the surrounding general corrosion product layer. In the sites indicated by the arrows, the contribution of CuO is more dominant, while the Cu_2O concentration is lower. This confirms again that corrosion products formed during global and local corrosion reactions differ substantially.

Conclusions

This work describes the study of corrosion products formed on commercially pure copper after immersion in chloride containing solutions. This was done using FE AES combined with a TFA analysis. In these solutions global corrosion as well as local attack reactions take place on the same surface. The more profound analysis of the composition of the general corrosion product layer learned that this porous layer consists of copper chlorides as well as oxides. The TFA analysis of this layer showed that it can be divided into 3 zones. The outermost zone consisted mainly of copper chlorides. Cu_2O was the oxide that was most prominently present in the corrosion product layers. CuO could also be found, being the most prominent compound right underneath the chloride rich layer. The porosity of the layer resulted in a permanent pure copper contribution throughout the layer.

The places where localized corrosion occurred showed a different composition. In these positions more chlorides were detected than in the surrounding areas. Also CuO was present more prominently than Cu_2O in these places. A combination of the observations led to the conclusion that the corrosion reaction products formed during local attack and global corrosion reactions differ substantially.

The results of this study, the identification of the corrosion products, will be combined with electrochemical investigations to enable the identification of the corrosion reactions taking place on the studied locations.
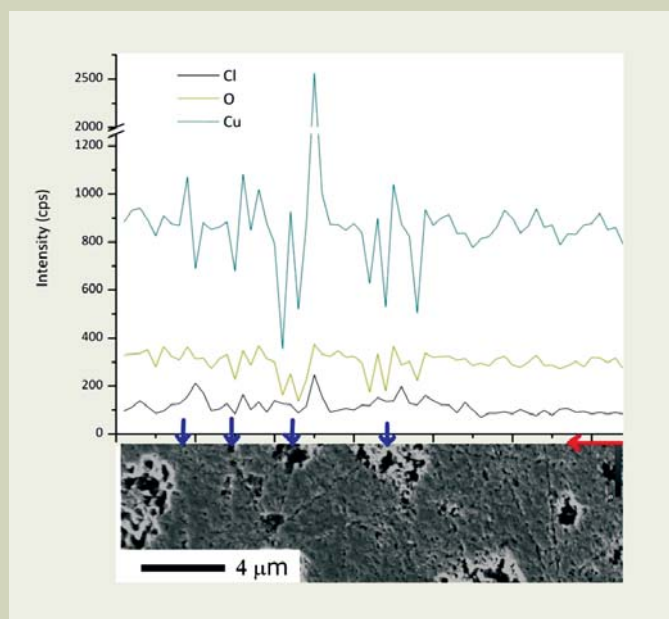
Acknowledgement

Fig.6 Concentration line profile recorded on a Cu surface after 6 hours of immersion in the NaCl solution. The analysis was performed on the line indicated by the red arrow. The blue arrows indicate local corrosion sites.
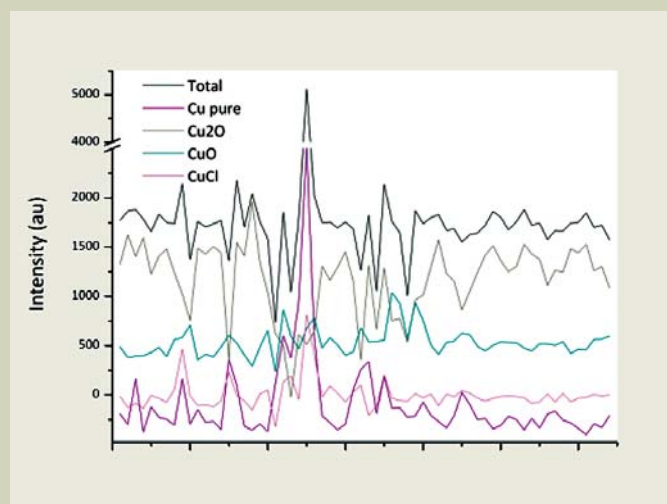

Fig.7 Result of the TFA analysis performed on the Cu LVV spectrum performed in Fig.6.

References

[1] Y. Van Ingelgem, A. Hubin and J.Vereecken, Investigation of the first stages of the localized corrosion of pure copper combining EIS, FE-SEM and FE-AES, *Electrochimica Acta,* **52** (27) (2007) 7642–7650.

[2] Y. Van Ingelgem, E. Tourwé, J. Vereecken and A. Hubin, Application of multisine impedance spectroscopy, FE-AES and FE-SEM to study the early stages of copper corrosion, Electrochimica Acta In Press, Corrected Proof (doi:10.1016/j.electacta.2008.01.052) .

[3] G. Kear, B. D. Barker and F. C. Walsh, Electrochemical corrosion of unalloyed copper in chloride media–a critical review,*Corrosion Science* **46** (1) (2004) 109–136.

[4] K. Efird, Potential-pH diagrams for 90-10 and 70-30 Cu-Ni in sea water, *Corrosion,* **31** (3) (1975) 77–83.

[5] C. Deslouis, B. Tribollet, G. Mengoli and M. M. Musiani, Electrochemical behavior of copper in neutral aerated chloride solution. i. steady-state investigation, *Journal Of Applied Electrochemistry,* **18** (1988) 374–383.

[6] C. Deslouis, B. Tribollet, G. Mengoli and M. M. Musiani, Electrochemical behavior of copper in neutral aerated chloride solution. ii. impedance investigation, *Journal Of Applied Electrochemistry,* **18** (1988) 384–393.

[7] B. Trachli, M. Keddam, H. Takenouti and A. Srhiri, Protective effect of electropolymerized 3-amino 1,2,4-triazole towards corrosion of copper in 0.5 M NaCl, *Corrosion Science,* **44** (5) (2002) 997–1008.

[8] G. Bech-Nielsen, M. Jaskula, I. Chorkendorff and J. Larsen, The initial behavior of freshly etched copper in moderately acid, aerated chloride solutions, *Electrochimica Acta,* **47** (27) (2002) 4279–4290.

[9] G. Bengough, R. Jones and R. Pirret, *Journal of the Institute of Metals,* **23** (1920) 65–158.

[10] G. Bengough, R. May, *Journal of the Institute of Metals,* **32** (1924) 81–269.

[11] K. Kinoshita, D. Landolt, R. Muller and C. Tobias, Stoichiometry of anodic copper dissolution at high current densities, *Journal of the Electrochemical Society,* **117** (10) (1970) 1246–1251.

[12] J.-P. Diard, J.-M. Le Canut, B. Le Gorrec and C. Montella, Copper electrodissolution in 1 M HCl at low current densities. II. Electrochemical impedance spectroscopy study, *Electrochimica Acta,* **43** (16-17) (1998) 2485–2502.

[13] A. El Warraky, H. El Shayeb and E.Sherif, Pitting corrosion of copper in chloride solutions, Anti-Corrosion Methods and Materials **51** (1) (2004) 52–61.

[14] H. H. Strehblow and B. Titze, The investigation of the passive behaviour of copper in weakly acid and alkaline solutions and the examination of the passive film by ESCA and ISS, *Electrochimica Acta,* **25** (6) (1980) 839–850.

[15] M. De Chialvo, R. Salvarezza, D. Vasquez Moll and A. Arvia, Kinetics of passivation and pitting corrosion of polycrystalline copper in borate buffer solutions containing sodium chloride., *Electrochimica Acta,* **30** (11) (1985) 1501–1511.

[16] C. Breslin and D. Macdonald, The influence of UV light on the dissolution and passive behavior of copper-containing alloys in chloride solutions, *Electrochimica Acta,* **44** (4) (1998) 643–651.

[17] R. Babic, M. Metikos-Hukovic and A. Jukic, Corrosion, passivation, and anodic film - a study of copper passivity by electrochemical impedance spectroscopy, *Journal of the Electrochemical Society,* **148** (4) (2001) B146.

[18] F. Falkenberg, K. Fushimi and M. Seo, Study on initiation of localised corrosion on copper thin film electrode by combinational use of an EQCM with a liquid-phase ion gun, *Corrosion Science,* **45** (11) (2003) 2657–2670.

[19] W. A. Badawy, K. M. Ismail and A. M. Fathi, Effect of Ni content on the corrosion behavior of Cu-Ni alloys in neutral chloride solutions, *Electrochimica Acta,* **50** (18) (2005) 3603–3608.

[20] P. Stefanov and T. Marinova, Adsorption of oxygen and formation of an oxide phase on a Cu(100) surface, *Applied Surface Science,* **31** (4) (1988) 445–450.

[21] A. Losev, K. Kostov and G. Tyuliev, Electron-beam induced reduction of CuO in the presence of a surface carbonaceous layer - an XPS HREELS study, *Surface Science,* **213** (2-3) (1989) 564–579.

[22] T. Conard, J. Ghijsen, J. M. Vohs, P. A. Thiry, R. Caudano and R. L. Johnson, Copper-oxide interface formationa vibrational and electronic investigation by electron spectroscopies, *Surface Science,* **265** (1-3) (1992) 31–38.

[23] M. Yoshitake, S. Bera and Y. Yamauchi, AES and LEED study of well-ordered oxide film grown on cu-9at.824–828.

[24] K. N. El'tsov, G. Y. Zueva, A. N. Klimov, V. V. Martynov and A. M. Prokhorov, Reversible coverage-dependent Cu + clads-]CuCl transition on Cu(111)/Cl2 surface, *Surface Science,* **1251** (1991) 753–758.

[25] Struers metalog, http://www.struers.fr/modules/emetalog.

Characterization of Coherent Precipitates in Mg-RE(-Zn) (RE: Gd, Y) Alloys by the Combination of HRTEM and HAADF-STEM

Kenji Hiraga and Masahiko Nishijima

Institute for Materials Research, Tohoku University

Mg-based alloys containing rare earth elements have been paid much attention as industrial materials, because of their low density and high recyclability. These alloys show remarkable precipitation hardening by aging of supersaturated solid solutions at low temperatures, and so it is important to elucidate microstructures of precipitates. We have studied structures of fine precipitates in Mg-Gd, Mg-Y and Mg-Gd-Zn alloys by the combination of HRTEM and HAADF-STEM, and obtained some valuable information, which can not be accomplished by only HRTEM or HAADF-STEM. In this paper, we review recent results about crystal structures and morphology of precipitates in the Mg-Gd, Mg-Y and Mg-Gd-Zn alloys.

Introduction

Utilization of Mg-based alloys is spreading in automotive, aerospace and electronic industries, because of their low density and high recyclability. High strength of the Mg-based alloys is performed using precipitation hardening by aging of supersaturated solid solutions of the alloys at low temperatures. Magnesium-based alloys containing rare earth elements such as Y, Gd, Nd, and Dy have a wide solubility limit of a few atomic percent at high temperatures and a very narrow solubility at low temperatures. Therefore, by aging of supersaturated solid solutions of Mg-RE (RE: rare earth metals) alloys, prepared by quenching from high temperatures, at low temperatures of about 200 ℃, precipitates enriched by rare earth elements appear in the Mg-matrix. Some reports on transmission electron microscopy (TEM), high-resolution transmission electron microscopy (HRTEM) and electron diffraction analysis of Mg-RE alloys have proposed that a β'' phase at the early stage of aging and β' phase at a peak hardness are precipitated [1-8]. However, there are some questions for previous reports, because HRTEM is not a powerful tool for investigation of fine precipitates being coherent to the matrix. On the other hand, high-angle annular detector dark-field scanning transmission electron microscopy (HAADF-STEM) is expected to enable us to image individual rare earth atoms, projected along the incident beam, in the Mg matrix, as single Cu layers in Guinier-Preston zone (GP-zone) in the Al-Cu system have been identified [9].

Recently, the authors have studied coherent

2-1-1 Katahira, Aoba-ku, Sendai, 980-8577, Japan

hiraga@imr.tohoku.ac.jp

precipitates in some Mg-RE alloys by the combination of HAADF-STEM and HRTEM, and resolved some doubts in previous reports. The purpose of the present paper is to review our recent results [10-13] and to demonstrate the power of HAADF-STEM for investigation of fine precipitates in Mg-based alloys containing heavy elements.

Experimental Procedure

Mg-RE(-Zn) alloys were prepared by melting construction metals by high frequency induction heating under an Ar gas in carbon crucibles. The alloys were homogenized at 520 ℃ for 2 hrs and then quenched in water, and finally were aged at 200 ℃. TEM specimens were cut from the alloys, and thinned by mechanical polishing and finally by ion-milling. TEM and HRTEM observations were performed by a 400 kV electron microscope (JEOL JEM-4000EX) with a resolution of 0.17 nm, and HAADF-STEM images were taken by a 300 kV electron microscope (JEOL JEM-3000F) equipped with a field emission gun in the scanning transmission electron microscope mode. In HAADF-STEM observations, a beam probe with a half width of about 0.2 nm was scanned on samples.

Short-range ordering in the early stage of aging in Mg-Gd alloy

Diffuse reflections in electron diffraction patterns have been found in the early stage of aging for many Mg-RE alloys, as can be seen in **Figure 1**(a) that is an electron diffraction pattern of the Mg-5at%Gd alloy aged at 200 ℃ for 5 hrs, taken with the incident beam parallel to the [001]m direction of the Mg-matrix.

Diffuse reflections are observed at 1/2 0 0-typed positions between strong reflections of an Mg-hexagonal lattice. Since the 1/2 0 0-typed positions correspond to ones of superlattice reflections of the $D0_{19}$ (Mg_3RE) structure, the diffuse reflections have been considered to result from fine precipitates of the Mg_3RE phase.

Figures 1(b) and (c) show HRTEM and HAADF-STEM images, respectively, corresponding to the diffraction pattern of Fig. 1(a). Structural modulations producing the diffuse reflections in Fig. 1(a) are represented as weak and fine contrast modulations in lattice fringes of the Mg-matrix in the HRTEM image of Fig. 1(b), but it is impossible to elucidate structural modulations from Fig. 1(b). On the other hand, the HAADF-STEM image of Fig. 1(c) can reproduce individual Gd atoms, projected along the incident beam, as bright dots without the disturbance of the Mg-matrix. Contrasts of the bright dots correspond to occupation probabilities of Gd atoms in atom columns along the incident beam, and arrangements of bright dots show those of Gd atoms projected along the incident beam. The arrangement of the bright dots in Fig. 1(c) indicates a short-range ordered state without the existence of fine precipitates with periodic arrangements in wide regions. The bright dots are mainly arranged with an interval of about 0.37 nm, which corresponds to a second nearest neighbor distance in a hexagonal close-packed (hcp) structure, and form characteristic local arrangements such as hexagonal arrangements indicated by arrows and zigzag lines with an interval of about 1.1 nm, indicated by arrowheads. The hexagonal arrangement of Gd atoms can be seen in the $D0_{19}$ structure, which is formed by ordering of Gd atoms located at second nearest neighbor positions in the hcp structure, as shown in **Figure 2**(c). In the $D0_{19}$ structure, the ordering
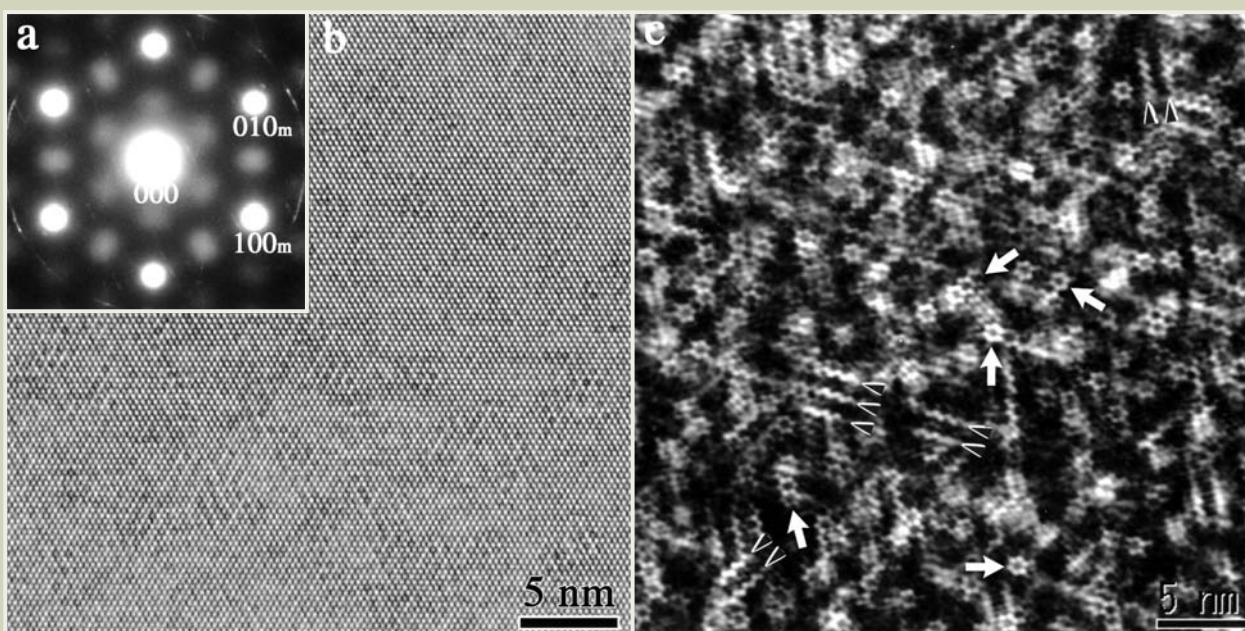
Fig.1 Electron diffraction pattern (a), HRTEM image (b) and HAADF-STEM image (c) of an Mg-5at%Gd alloy aged at 200 °C for 5 hrs, taken with the incident beam parallel to the [001]$_m$ direction of the hexagonal Mg-matrix.
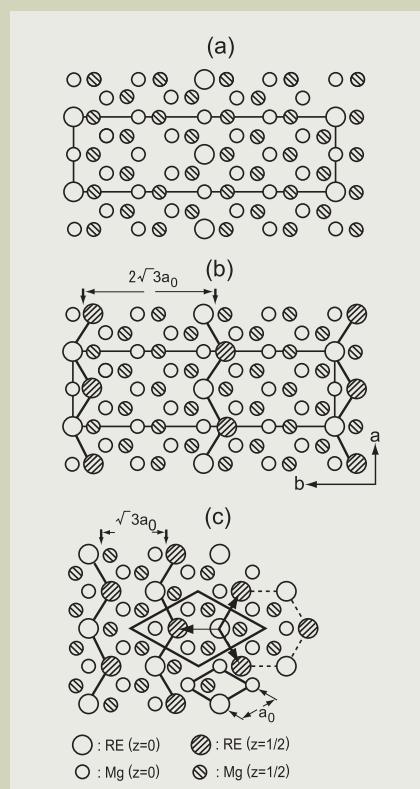

Fig.3 HAADF-STEM image of a β' phase, taken with the incident beam parallel to the [001] direction of the orthorhombic β' phase structure.

Fig.2 Structure models of previous work [14] (a) and our recent work [10] (b) of the β' phase, and of D0$_{19}$ (Mg$_3$RE) structure (c).
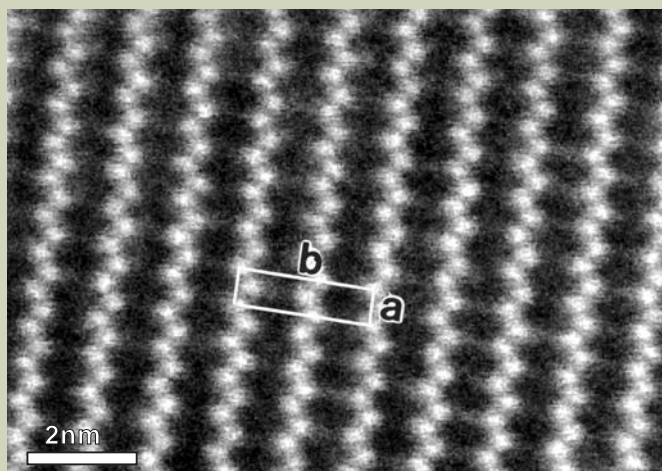
of Gd atoms forms a hexagonal arrangement with a side length of $(2a_0\sqrt{3})/3=0.37$ nm, where a_0 is a lattice parameter of a Mg hexagonal lattice, as can be seen in Fig. 2(c). The zigzag lines with an interval of 1.1 nm correspond to those of Gd atoms with an interval of $2a_0\sqrt{3}$ in the Mg$_7$Gd structure of the β' phase, as shown in Figure 2(b). That is, nuclei of the Mg$_7$Gd structure occur in the short-rage ordered state by aging at 200 °C for 5 hrs.

The present observations clearly verify that precipitates of a β'' phase with a D0$_{19}$ structure, proposed by many previous papers [6-9], do not exist in the early stage of aging, showing diffuse reflections in electron diffraction patterns, and that a short-range ordered state in

Gd-enriched regions is formed and nuclei of the Mg$_7$Gd structure occur in the short-range ordered region.

Crystal structure of the β' phase

The β' phase of an ordered structure with an orthorhombic unit precipitates in many Mg-RE alloys aged at a peak hardness condition. **Figure 3** shows an HAADF-STEM image of the β' phase in the Mg-5at% Gd alloy aged at 200 °C for 100 hrs, taken with the incident beam parallel to the c-axis of the orthorhombic structure. The deformation of a unit cell indi-

cated by white lines from a rectangle in Fig. 3 results from the sample drift during scanning of the incident beam. In the image of Fig. 3, zigzag arrays of bright dots along the a-axis are observed. From this image, a structure model of the β' phase can be directly derived as Fig. 2(b). In the model of Fig. 2(b), Gd atoms are arranged with face-centered symmetry in z=0 and z=1/2 planes in an orthorhombic unit cell of a=2a$_0$=0.64 nm, b=4a$_0\sqrt{3}$=2.22 nm and c=c$_0$=0.52 nm, where a$_0$ and c$_0$ are lattice constants of a hexagonal unit of the Mg-matrix. In the atomic arrangement of Fig. 2(b) projected along the c-axis, zigzag arrays of Gd atoms, indicated by thick line, along the a-axis correspond to those of bright dots in Fig. 3.
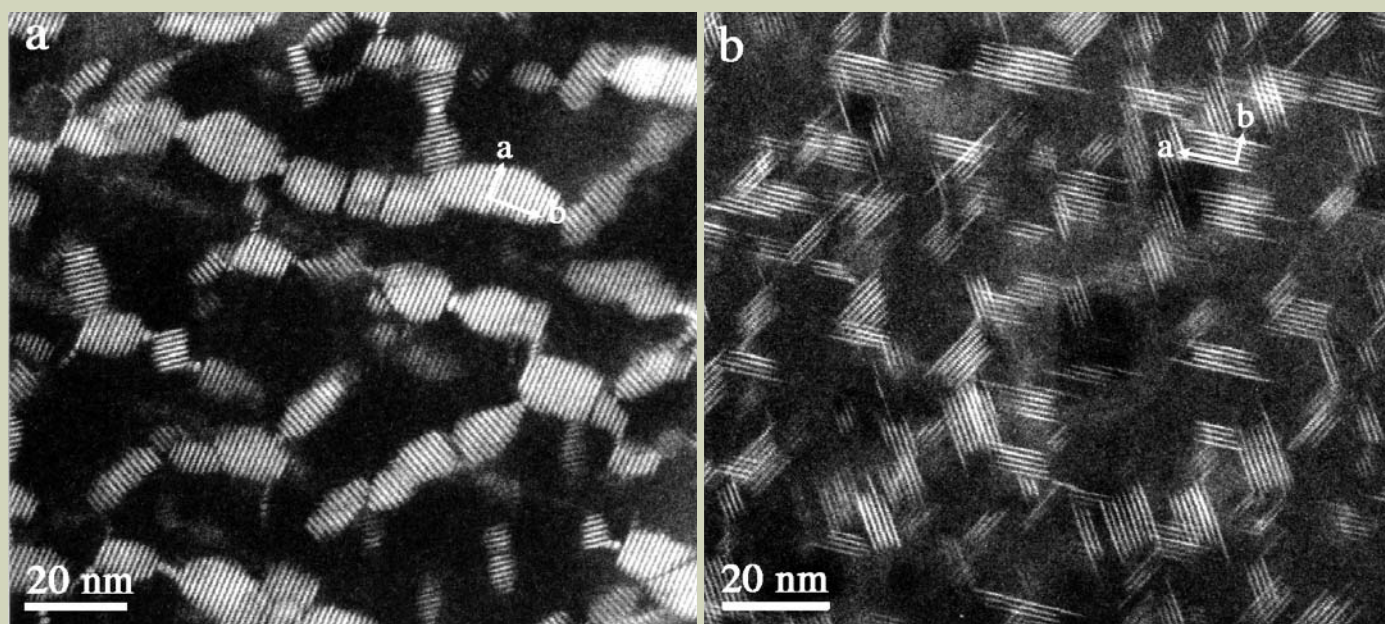
Fig.4 HAADF-STEM images of β' precipitates in an Mg-5at%Gd alloy aged at 200 °C for 10 hrs (a) and Mg-2at%Y alloy aged at 200 °C for 150 hrs (b), taken with the incident beam parallel to the [001]$_m$ direction of the hexagonal Mg-matrix.

Fig.5 HRTEM images of β' precipitates in an Mg-5at%G alloy aged at 200°C for 100 hrs (a) and Mg-2at%Y alloy aged at 200 °C for 150 hrs (b), taken with the incident beam parallel to the [001]$_m$ direction of the hexagonal Mg-matrix.
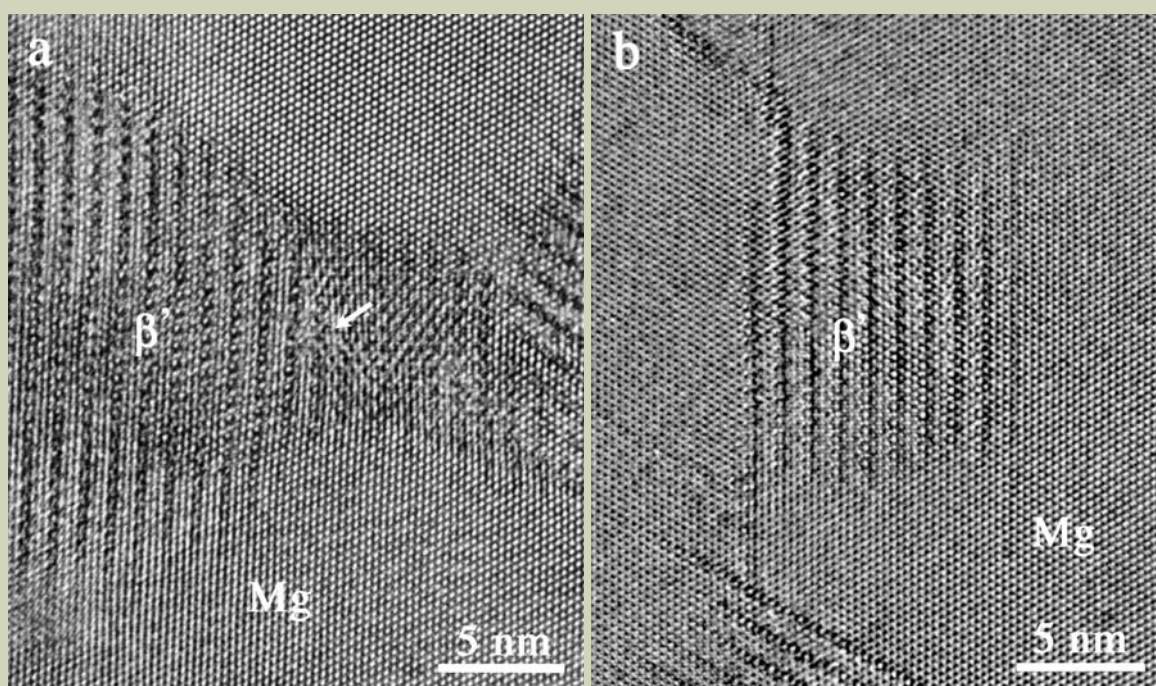
The structure model has an atomic ratio of Mg$_7$Gd, which shows a good correspondence to a composition of the β' phase (88 at%Mg and 12 at%Gd) evaluated by EDS. It should be noted here that the present structural model of the β' phase is apparently different from a previous model (Figure 2(a)) proposed by HRTEM observations [14]. As for the atomic arrangement in the z=0 plane, both the models are the same, but the z=1/2 plane in the previous model is formed by only Mg atoms without any Gd atoms, and so a composition of the previous model becomes Mg$_{15}$Gd. Obviously, the previous model can not explain the zigzag arrays of bright dots in the HAADF-STEM image of Fig. 3 and also the evaluated compo-

sition of the β' phase (88 at%Mg and 12 at%Gd). We have confirmed that the β' phase in an Mg-Y alloy has the same structure as Fig. 2(b) [12].

Morphology of β' precipitates in Mg-Gd and Mg-Y alloys

Figure 4 is HAADF-STEM images of β' precipitates in Mg-5at%Gd (a) and Mg-2at%Y alloys (b), taken with the incident beam parallel to the [001]$_m$ direction of the Mg-matrix. Bright lattice fringes in Fig. 4 correspond to zigzag arrays of bright dots in Fig. 3 *viz.*, zigzag arrays of Gd or Y atoms along the a-

axis in the β' structure in Fig. 2(b). In Fig. 4, one can see three variants of β' precipitates with different directions of a- and b-axes, which are equivalent directions in the Mg-hexagonal lattice, and also can notice that morphologies of the β' precipitates in Fig. 4(a) and 4(b) are extremely different. In Fig. 4(a), the precipitates with an oval shape, which corresponds to the section of rod-shaped precipitates with a rod-axis along the c-axis, with a long radius along the b-axis and short one along the a-axis are joined along the b-axis. Successive joining of rod-shaped precipitates are performed along the b-axis, and consequently produces planar-shaped precipitates extended over an about 100 nm length along
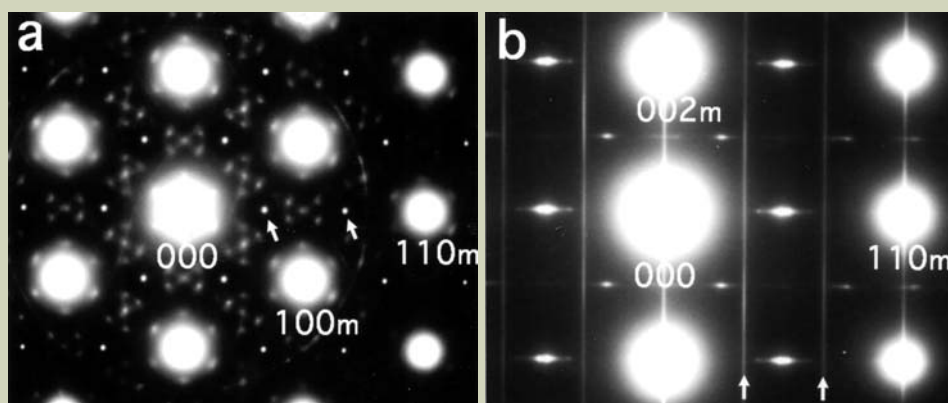
Fig.6 Electron diffraction patterns of the Mg-2at%Gd-1at%Zn alloy aged at 200 °C for 150 hrs, taken with the incident beam parallel to the $[001]_m$ (a) and $[110]_m$ (b) directions of the hexagonal Mg-matrix. 1/3 1/3 0-typed extra reflections indicated by arrows in (a) and streak reflections indicated by arrows in (b) are observed in addition to superlattice reflections of β' phases between strong reflections indexed by a hexagonal lattice of the Mg-matrix.
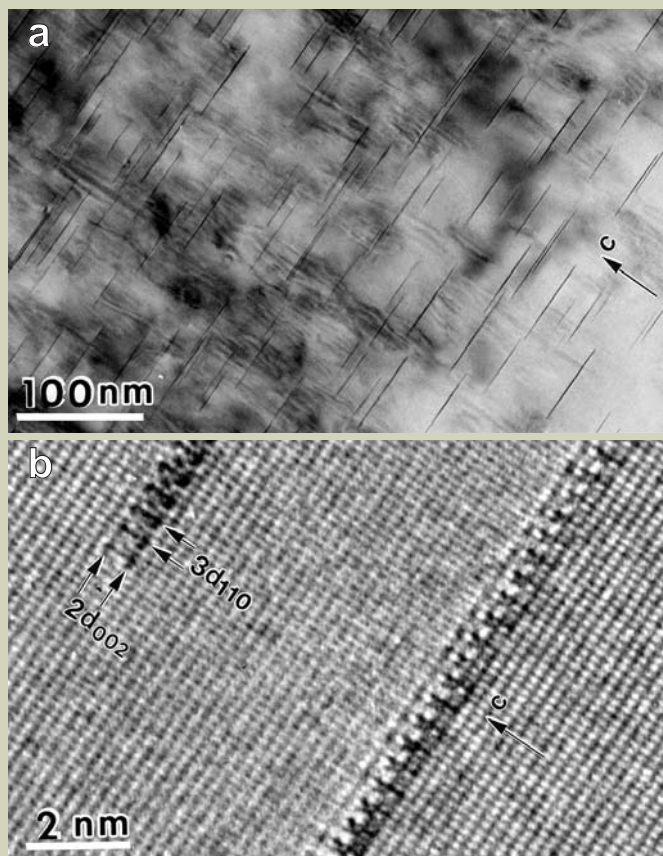

Fig.7 TEM (a) and HRTEM (b) images of the Mg-2at%Gd-1at%Zn alloy aged at 200 °C for 150 hrs, taken with the incident beam parallel to the $[110]_m$ direction of the hexagonal Mg-matrix. Line contrasts perpendicular to the c-axis in (a) are GP-zones. The HRTEM image of two GP-zones embedded in the Mg-matrix in (b) shows an ordered arrangement of bright and dark dots, with intervals of $2d_{002}$ and $3d_{110}$ spacings of a hexagonal lattice of the Mg-matrix, in the GP-zones.
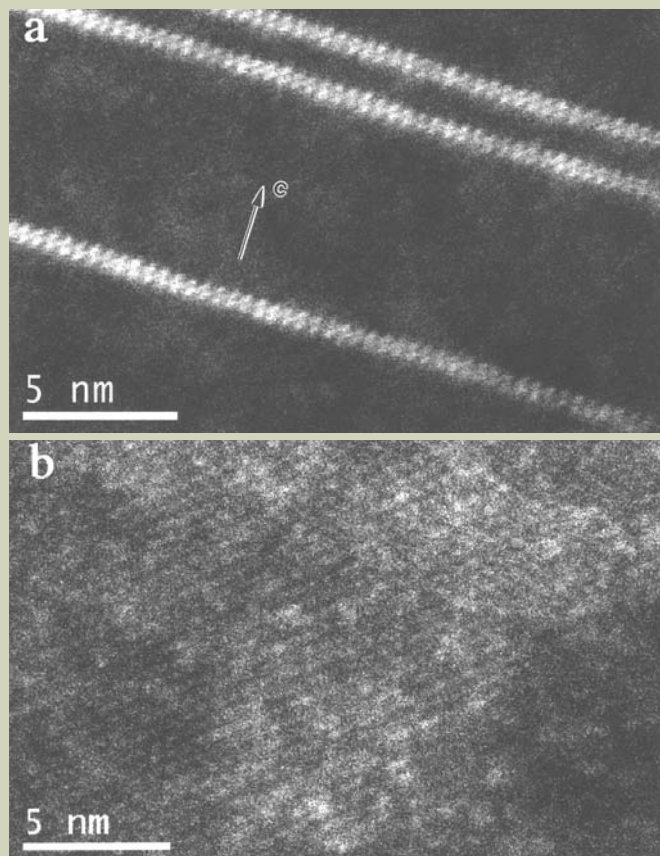

Fig.8 HAADF-STEM images of GP-zones in the Mg-2at%Gd-1at%Zn alloy aged at 200 °C for 150 hrs, taken with the incident beams parallel to the $[110]_m$ (a) and $[001]_m$ (b) directions of the hexagonal Mg-matrix. Dumbbells of two bright dots are periodically arranged along GP-zones in (a), and weak bright dots in (b) are arranged with a hexagonal lattice. The bright dots correspond to Gd and/or Zn atoms projected along the $[110]_m$ (a) and $[001]_m$ (b) directions.

$[110]_m$-typed directions of the Mg-matrix, as can be seen Fig. 4(a). Remains of junctions of the rod-shaped precipitates can be seen as concaves and dark fringes in Fig. 4(a). On the other hand, precipitates in the Mg-2at%Y alloy has no definite shape, being due to independent growth of Y-enriched atomic planes. Surfaces normal to the b-axis in the precipitates have definite facets parallel to the (010) plane, but those normal to the a-axis have no definite facets and the independent growth of Y-enriched atomic planes are observed.

The difference in morphologies of the β' precipitates in Mg-Gd and Mg-Y alloys can be understood by values of lattice misfits between the β' phases and the Mg-matrix. That is, it is

considered to result from the difference between lattice parameters of a and b for the Mg$_7$Gd and Mg$_7$Y structures. Lattice parameters of the orthorhombic β' phase in the Mg-5at%Gd alloy aged at 250 °C for 100 hrs were estimated as a=0.650 nm, b=2.272 nm and c=0.521 nm [12], which are remarkable differences from $2a_0$=0.6418 nm, $4a_0\sqrt{3}$=2.2232 nm and c_0=0.5210 nm. On the other hand, lattice parameters of the orthorhombic β' phase in the Mg-2at%Y alloy are nearly a=$2a_0$=0.6418 nm and b=4 $a_0\sqrt{3}$=2.2232 nm.

Figure 5 shows HRTEM images of β' precipitates embedded in the Mg-matrix in Mg-5at%Gd (a) and Mg-2at%Y (b) alloys. Lattice fringes in the β' precipitates and Mg-matrix

are continuously bound up without any interface dislocations. That is, the β' phases precipitates with being fully coherent to the Mg-matrix. However, a relatively large lattice misfit between the β' phase and Mg-matrix in the Mg-Gd alloy (Fig. 5(a)) produces lattice distortions in the both crystals. Consequently, the lattice distortions due to the lattice misfit are relaxed by the appearance of dislocations in the β' precipitates, as indicated by an arrow in Fig. 5(a). On the other hand, a small lattice misfit between the β' phase of the Mg-Y alloy and Mg-matrix produces no lattice distortions at interfaces between the β' precipitates and Mg-matrix, and permits individual growth of Y-enriched atomic planes along the a-axis, as
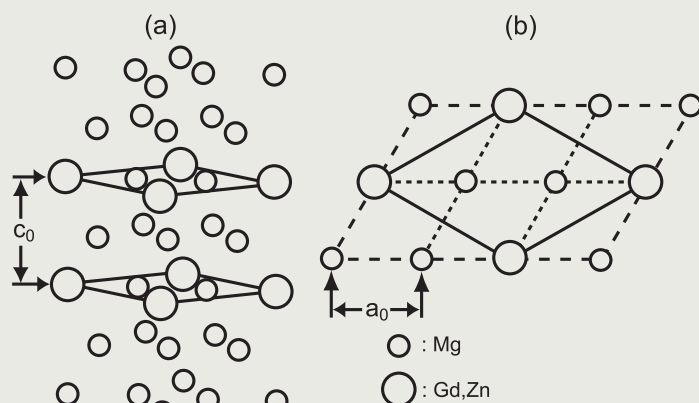
Fig.9 Structural model of the GP-zone. Gd and/or Zn atoms are located in two close-packed planes sandwiching a close-packed plane of Mg atoms, as shown in (a), and occupy at an ordered positions, as shown in (b). a_0 and c_0 are lattice parameters of a hexagonal structure of the Mg-matrix.

can be seen in Fig. 5(b).

Guinier-Preston zone in Mg-Gd-Zn alloy

Figures 6(a) and (b) are electron diffraction patterns of the Mg-2at%Gd-1at%Zn aged at 200 ℃ for 150 hrs, taken with the incident beam parallel to the $[001]_m$ and $[1\bar{1}0]_m$ directions of the hexagonal Mg-matrix, respectively. In the diffraction patterns, 1/3 1/3 0-typed extra spots indicated by arrows in Fig. 6(a) and streak reflections indicated by arrows in Fig. 6(b) are observed in addition to superlattice reflections of β' precipitates between strong reflections of a hexagonal lattice of the Mg-matrix. From the comparison between Fig. 6(a) and Fig. 6(b), it can be concluded that the 1/3 1/3 0-typed extra spots in Fig. 6(a) correspond to sections of the streak reflections in Fig. 6(b), and that the streak reflections in Fig. 6(b) have a rod-shape.

In HRTEM images taken with the incident beam parallel to the $[001]_m$ direction of the hexagonal Mg-matrix, the β' precipitates are observed, but precipitates showing the 1/3 1/3 0-typed extra reflections in Fig. 6(a) can not be recognized.

Figures 7(a) and (b) show a TEM and an HRTEM images of the Mg-2at%Gd-1at%Zn alloy, respectively, taken with the incident beam parallel to the $[1\bar{1}0]_m$ direction of the hexagonal Mg-matrix. Planar faults producing the streak reflections in Fig. 6(b) are observed as line contrasts perpendicular to the c-axis in Fig. 7(a). The line contrasts are GP-zones formed by two close-packed planes with an ordered arrangement of Gd and/or Zn atoms, as will be shown later. On the other hand, the β' precipitates are observed as blurred bright and dark contrasts in Fig. 7(a). The HRTEM image of Fig. 7(b) shows that the GP-zones precipitate coherently in the Mg-matrix, and bright and dark dots in the GP-zones show an ordered arrangement with intervals of $2d_{002}$ and $3d_{110}$ spacings of a hexagonal lattice of the Mg-matrix.

Figures 8(a) and (b) show HAADF-STEM images of the GP-zones, taken with the incident beams parallel to $[1\bar{1}0]_m$ and $[001]_m$ directions of the Mg-matrix, respectively. In Fig. 8(a), dumbbells of bright dots with an interval of about 0.5 nm are periodically arranged with an interval of about 0.5 nm along the GP-zones. It is reasonably considered that these intervals correspond to those of $2d_{002}=c_0=0.52$ nm and $3d_{110}=3a_0/2=0.48$ nm, respectively, as shown in Fig. 7(b), and that the bright dots represent Gd and/or Zn atoms projected along the $[1\bar{1}0]_m$ direction. On the other hand, the image of Fig. 8(b) shows a hexagonal arrangement of weak bright dots, with an interval of about 0.6 nm. The weak contrast in Fig. 8(b) is due to only two layers of Gd and/or Zn atoms of the GP-zone embedded in about 100 atomic layers of the Mg-matrix. That is, the result demonstrates that HAADF-STEM makes it possible to observe an image contrast of two layers of Gd and/or Zn atoms embedded in the Mg-matrix with a few tens of nm in thickness. Although many GP-zones embedded in the Mg-matrix produce the 1/3 1/3 0-typed extra spots in Fig. 6(a), it is impossible to form the image contrast of the GP-zone in the HRTEM observation.

From the images of Fig. 7(b), 8(a) and 8(b), we can directly derive a structural model of the GP-zone, as shown in **Figure 9.** In the model, Gd and/or Zn atoms occupy at ordered positions in two close-packed planes sandwiching a close-packed plane of Mg-atoms. The bright dots in Figs. 8(a) and 8(b) represent Gd and/or Zn atoms projected along the incident beam parallel to the $[1\bar{1}0]_m$ and $[001]_m$ directions, respectively. The atomic arrangement of the GP-zone is similar to that of plate-like precipitates found in Mg-2.4wt%RE-0.4wt%Zn-0.6wt%Zr alloys [15], and also can be seen in the crystal structure of a precipitate phase in rapidly solidified Mg-2at%Ce-1at%Zn and Mg-2at%Ce alloys [16].

Conclusion

We have reviewed recent results for microstructures of coherent precipitates in Mg-based alloys containing rare earth elements, studied by the combination of HRTEM and HAADF-STEM. Direct observations of individual rare earth atoms projected along the incident beam by HAADF-STEM enable us to determine directly arrangements of rare earth atoms in a hexagonal Mg-lattice. On the other hand, HRTEM images show crystallographic relationships between lattices of precipitates and the Mg-matrix. Therefore, it can be concluded that the combination of HRTEM and HAADF-STEM is the most powerful tool for characterization of fine precipitates being coherent with the matrix crystals.

References

[1] Rokhilin L L: Phys. Met. Metall., **55,** 98 (1983).
[2] Antion C, Donnadieu P, Perrad F, Deschamps A, Tassin C and Pisch A: *Acta Mater.,* **51,** 5335 (2003).
[3] Nie J F, Gao X and Zhu S M: *Scripta Mater.,* **53,** 1049 (2005).
[4] M. Hisa, J. C. BARRY and G. L. Dunlop: *Proc. of the third International Magnesium Conf.* (The Institute of Materials, London, 1997) pp. 369-379.
[5] Kamado S, Kojima Y, Ninomiya R and Kubota K: *Proc. of the third International Magnesium Conf.* (The Institute of Materials, London, 1997) pp. 327-342.
[6] Vostry P, Smola B, Strulikova I, von Buch F and Mordike B L: *phy. stat. sol.,* (a) **175,** 491 (1999).
[7] Smola B, IStulikova I, von Buch F and Mordike B L: *Mater. Sci. and Eng.,* **A324,** 113 (2002).
[8] Apps P J, Karimzadeh H, King J F and Lorimer G W: *Scripta Mater.,* **48,** 1023 (2003).
[9] Konno T J, Kawasaki M and Hiraga K: *Phil. Mag.,* **B81,** 1713 (2001).
[10] Nishijima M, Hiraga K, Yamasaki M and Kawamura Y: *Mater. Trans.,* **47,** 2109 (2006).
[11] Nishijima M and Hiraga K: *Mater. Trans.,* **48,** 10 (2007).
[12] Nishijima M, Yubuta K and Hiraga K: *Mater. Trans.,* **48,** 84 (2007).
[13] Nishijima M, Hiraga K, Yamasaki M and Kawamura Y:*Mater. Trans.* **49,** 227 (2008).
[14] Honma T, Ohkubo T, Kamado S and Hono K: *Acta Mater.,* **55,** 4137 (2007).
[15] Pong D -H, Hono K and Nie J F: *Scripta Mater.,* **48,** 1017 (2003).
[16] Nishijima M, Hiraga K, Yamasaki M and Kawamura Y: *Mater. Trans.,* **48,** 476 (2007).

Quantitative Electron Microscopy Using Digital Data Processing

Kazuo Ishizuka† and Eiji Okunishi††

†HREM Research Inc
††Electron Optics Division, JEOL Ltd.

Digital equipments for electron microscopy, such as a CCD camera, come into wide use, and performance of a personal computer becomes more powerful than that of a main computer a decade ago. Thus, quantitative electron microscopy becomes a reality, where digital data obtained by using an electron microscope is analyzed quantitatively. Quantitative electron microscopy makes it possible to deduce information from an observed data, which is hard to be detected before by using human eyes. This report will introduce quantitative electron microscopy by making use of the data taken with JEOL JEM-2100F using some of the plug-ins developed at HREM Research for DigitalMicrograph (Gatan).

Introduction

Current hot topics of high-resolution electron microscopy are high-resolution STEM-HAADF imaging and spherical aberration correction of an objective lens using a multi-poles corrector. There are two types of corrector, one is for a probe forming objective lens in a STEM mode, and the other is for an imaging objective lens in a CETM mode. When a spherical aberration is corrected, we can expect in principle an improvement of resolution. However, it does not simply mean that getting an atomic resolution image becomes easier using a Cs-corrected microscope than using a conventional microscope. Especially in a CTEM mode a sample for high-resolution microscopy is well approximated as a phase object. Thus, when a spherical aberration is corrected in CTEM, at a just defocus our sample only gives a weak scattering contrast (amplitude contrast). Furthermore, to realize an improvement of resolution we will be faced with unprecedented demands for stability of microscope and skills of operating a microscope and preparing a good sample.

On the other hand, digital equipments for electron microscopy, such as a CCD camera, come into wide use, and performance of a personal computer becomes more powerful than that of a main computer a decade ago. Thus, quantitative electron microscopy becomes a reality, where digital data obtained by using an electron microscope is analyzed quantitatively. Quantitative electron microscopy may enhance periodic structure by reducing a periodic noise from an image; improve resolution of a STEM-HAADF image or an EELS spectrum using deconvolution technique; and measure lattice distortion from a single lattice image. Moreover, procedures to reconstruct a wave front and correct spherical aberration from a series of CTEM images have been proposed [1-3], and corresponding software are now commercially available.

This report will introduce quantitative electron microscopy using plug-ins developed at HREM Research for DigitalMicrograph (Gatan [4]). Although we cannot introduce all of our plug-ins due to space limitations, we hope that we can demonstrate effectiveness of quantitative electron microscopy, and encourage the reader to apply quantitative microscopy on their data at hand.

Resolution Improvement of STEM-HAADF Image

A STEM-HAADF image can be approximately expressed by using a convolution integral between an instrument function, a probe function here, and an object function [5]. Deconvolution is a procedure to estimate the object function from an experimental data and the instrument function. Eliminating an effect of the instrument function from an experimental image is equivalent to eliminating an effect of an objective lens from an experimental image, and thus corresponds to a Cs-correction in STEM by means of image processing software. Among various techniques proposed for deconvolution Maximum Entropy Method (MEM) and Richardson-Lucy Algorithm (RLA) are most popular. For STEM-HAADF imaging Pennycook and his coworkers applied a MEM technique developed in astronomy, where an object function is a point like star. They used a Gaussian and Lorentzian for a probe function, and concluded that a shape of the probe is not important [6]. However, our deconvolution procedure for DigitalMicrograph dedicated to STEM-HAADF (DeConvHAADF) [7] does not assume a point like object, and a good estimate of a probe function is essentially important. The MEM and RLA procedures adopted in DeConvHAADF deduce a solution by changing an estimate function iteratively in such a way that a convolution integral between the estimate function and the probe function reproduces the experimental image. Thus, we can estimate an object function with negligible noise, when we stop the iteration at an appro-
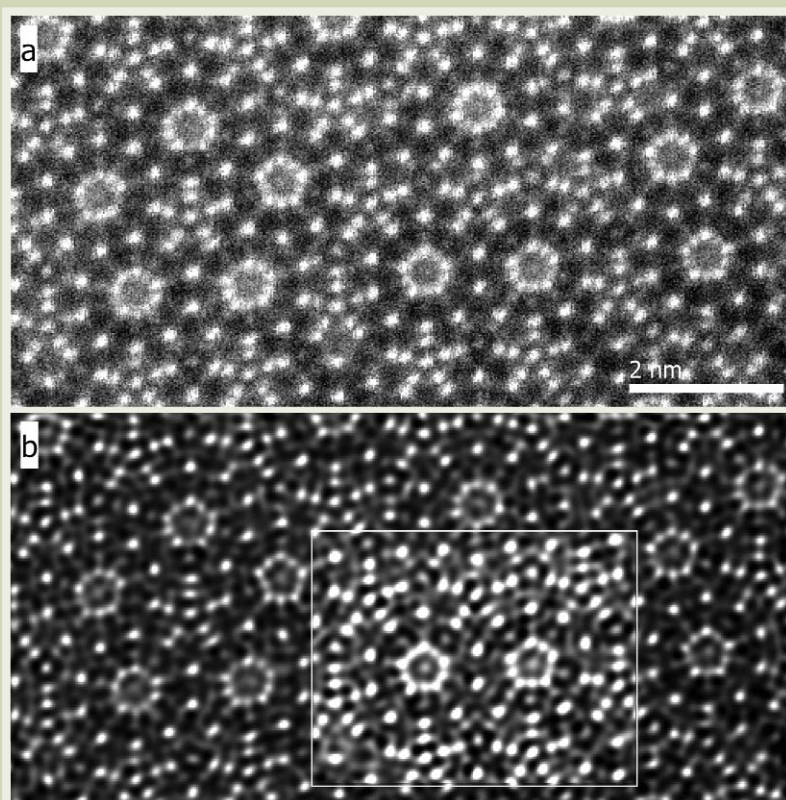
14-48 Matsukazedai, Higashimatsuyama 355-0055 Japan

E-mail : ishizuka@hremresearch.com

Fig.1 Resolution improvement of STEM-HAADF image using deconvolution.

(a) STEM-HAADF image of a decagonal quasi-crystal $Al_{64}Cu_{22}Co_{14}$ taken with JEM-2100F equipped with CEOS Cs-corrector for STEM.

(b) Result of a MEM deconvolution. Contrast is adjusted in a rectangle box to enhance weak peaks. Probe conditions: Cs=0mm, 24-mrad convergence angle, defocus=0; Gaussian demagnified source with FWHM of 2 pixels; Gaussian focus spread with FWHM of 5 nm.
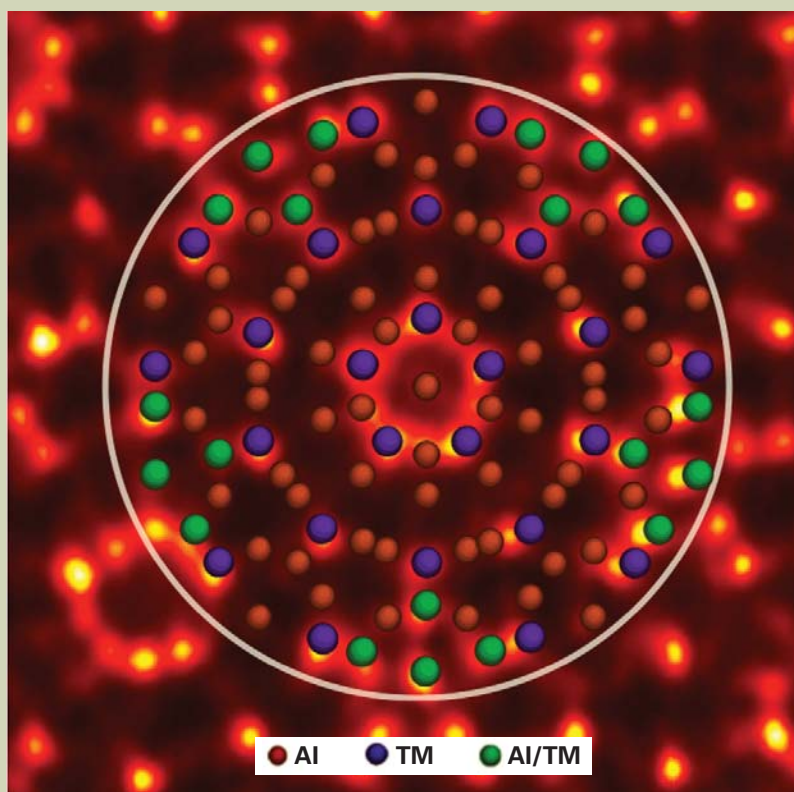

Fig.2 Model structure of decagonal quasi-crystal $Al_{64}Cu_{22}Co_{14}$.
Cluster model of five-fold symmetry with a diameter of about 2nm. Al represents aluminum, and TM a transition metals, namely Cu or Co. (reproduced from *JEOL News,* **Vol.42** (2007) 15 by permission)

priate stage of deconvolution.

Here, we will show an example of deconvolution applied to a STEM-HAADF image of a decagonal quasi-crystal $Al_{64}Cu_{22}Co_{14}$ (**Fig. 1**(a)) taken with JEOL JEM-2100F equipped with CEOS Cs-corrector for STEM [8]. If you are interested in details on a sample and its analysis, please consult an original article [9] by the authors who kindly provide this image for our analysis. In the case of Cs-corrected STEM we can extend a convergence angle for probe forming lens, and thus a resultant probe becomes so small that we have to take care of the size of a physical source demagnetized by a condenser system. Moreover, a large convergence angle means a depth of focus becomes small, and thus we have to consider a focus spread due to chromatic aberration. These two points have been ignored for STEM-HAADF imaging with a conventional STEM without a Cs-corrector. We improved recently a probe function of DeConvHAADF to include these two effects.

Figure 1 (b) shows the result of a MEM deconvolution using a probe obtained for Cs = 0 mm at a just focus with 24-mrad convergence angle. The demagnified source size is approximated by a Gaussian with FWHM of 2 pixels, while a focus spread by a Gaussian with FWHM of 5 nm. Contrast is adjusted in a rectangle box to enhance weak peaks. Salt-and-pepper noise in the experimental image is reduced, and blurred contrast becomes sharp. On the other hand some peaks appear at the places where the experimental image does not show clear evidence of their existence. However, we may note that the result of deconvolution including the latter peaks satisfies the experimental image, and seems to correspond to an expected average structure of decagonal quasi-crystal shown in **Fig. 2** [9].

Single Atom Detection by Noise Suppression

Figure 3 (a) shows a STEM-HAADF image of PtRu catalyst particles on carbon support taken with JEM-2100F equipped with CEOS Cs-corrector for STEM [9]. As you can see from this figure aperiodic material such as carbon film gives pixel-wise random noise in a STEM-HAADF image. We have demonstrated that deconvolution is effective to improve resolution of a STEM-HAADF image, namely to correct a spherical aberration of a probe forming lens. It is also effective to reduce the pixel-wise random noise as we will describe in this section. This is because an observed image is given by a convolution integral between an object function and a probe function, and thus each pixel of the observed image should not be absolutely random.

When we continuously observe PtRu catalyst particles, a bright spot occasionally migrates from a border of a PtRu particle. The bright spot is believed to be a single atom of Pt or Ru. **Figure 4** (a) is an intensity profile along the line connecting two bright spots indicated by red arrowheads in Fig. 3 (a). We can recognize the presence of these bright spots from a STEM image, when weak intensity is enhanced as in Fig. 3 (a). However, it is difficult to determine a strength and size of the

bright spot from the line profile, since a random noise is so severe. Figure 4 (b) corresponds to a line profile of the image, where the random noise is reduced by 3×3 local average. Here, the existences of the particles become clear, but a reduction of peak height and an increase of peak width (FWHM = 0.125 nm) are unavoidable. Figure 3 (b) reproduces a result of deconvolution of the image, where a raw image is pre-smoothed by convolution with a Gaussian of 3-pixel FWHM in order to reduce a random noise, and then the result was deconvoluted with both the probe function used for a quasi-crystal above and the Gaussian used for pre-smoothing simultaneously. Figure 4 (c) is a corresponding line profile obtained from Fig. 3 (b). Here, the random noise in the original image turns into a smoothly varying background, while the peak

heights become higher than those in the original image. An increase of the peak height is a consequence of peak sharpening (FWHM = 0.11 nm) due to deconvolution. Peak heights of these two peaks are close to each other, and also close to a peak height of a bight spot (indicated by a red arrowhead) at the border of a PtRu particle, which is probably a single atom. Therefore, these two spots seem to correspond to a single Pt atom.

If we assume a contrast ratio of Pt and Ru atom is proportional to a square of atomic number ratio (44/78), the contrast ratio of Pt and Ru becomes 0.32. Thus a peak height of Ru atom will be about two-times of a background variation of Fig. 4 (c). Then, a spot whose peak height is significantly higher than the background fluctuation, and also lower than Pt peaks, may correspond to a single Ru

atom as indicated by a yellow arrowhead.

Measurement of Lattice Distortion and Column Intensity

Occasionally, we want to quantitatively measure intensity of each column of a lattice image for such a case to identify constituent atoms of the columns. However, measuring intensities at many column positions manually to get a statistical estimation is a laborious work. On the other hand a number of techniques to measure lattice distortion from a single lattice image with accuracy of an order of 1% (absolute distortion of an order of pm) were proposed, and some of them were made available commercially. GPA (Geometrical Phase Analysis) [10] is one of such plug-in,
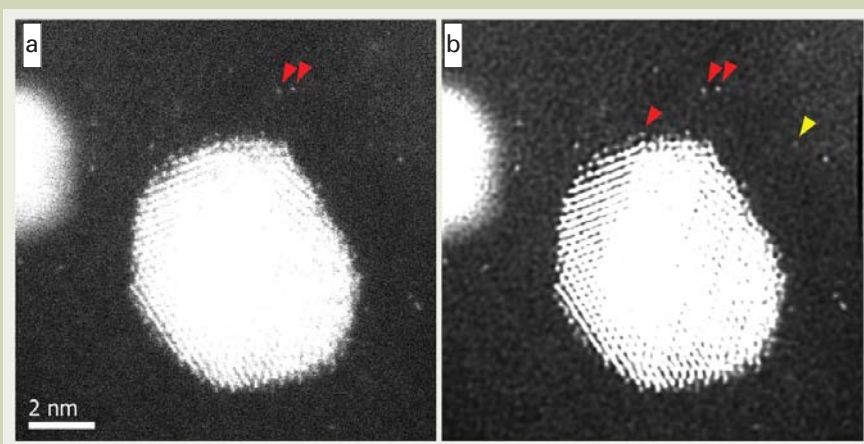

Fig.3 Noise reduction of STEM-HAADF image using deconvolution.

(a) STEM-HAADF image of PtRu catalyst particles on a carbon support taken with JEM-2100F equipped with CEOS Cs-corrector for STEM. The presence of the bright spots can be recognized from a STEM image, when weak intensity is enhanced. However, it is difficult to determine a strength and size of the bright spot, since a random noise is so severe.

(b) Result of a MEM deconvolution. A raw image was smoothed by convolution with a Gaussian of 3-pixel FWHM in order to reduce a random noise, then the result was deconvoluted with both the same probe function used for a quasi-crystal and the Gaussian used for pre-smoothing. Random noise is reduced, and the bright spots become clear. Red arrow head may represent a single Pt atom, while yellow arrow head a single Ru atom.
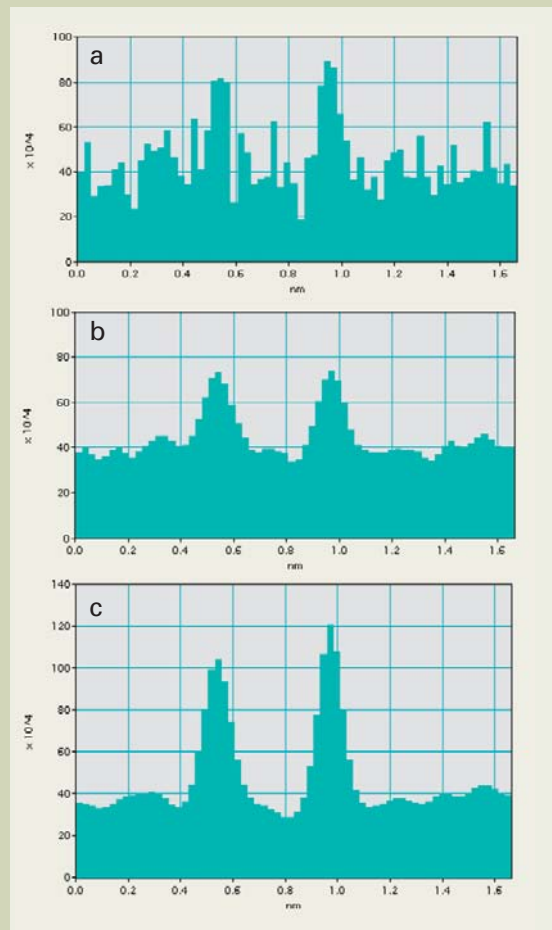
Fig.4 Intensity profiles over bright spots in STEM-HAADF image.

(a) Intensity profile along the line connecting two bright spots indicated by red arrowheads in Fig. 3 (a). It is difficult to determine a strength and size of the bright spot from the line profile, since a random noise is so severe.

(b) Line profile of the image where the random noise is reduced by local average. Here, the existences of the particles become clear, but a reduction of peak height and an increase of peak width are unavoidable.

(c) Line profile of the image where the random noise is reduced with MEM deconvolution. Here, the random noise turns into a smoothly varying background, while a peak height becomes higher than that in the original image. The peak heights of two peaks are close to each other, and these peaks probably correspond to single Pt atoms.

which will be briefly introduced in Other Plug-ins section. In this section we will introduce another strain measurement plug-in called PPA (Peak Pair Analysis) [11] in reference to a STEM-HAADF image of GaAs. PPA estimates lattice strain from a change of distance between column pairs after automatically determining column positions. Since PPA determines column positions, it is easy to get intensity statistics of different columns by automatically measuring intensity at each column position.

Figure 5 (a) shows a STEM-HAADF image of GaAs [100] taken with JEM-2100F equipped with CEOS Cs-corrector for STEM. If we look carefully the image with a help of red reference lines, we can detect slowly varying image distortion. A STEM-HAADF image often shows this kind of distortion owing to

such as specimen charge-up from electron irradiation, specimen change during observation and so on, even when probe scanning is stable. This kind of image distortion can be measured as a lattice deformation. Then, we can rectify image distortion using information on lattice deformation, when actual specimen deformation is negligible. Figure 5 (b) shows pseudo-color variations of x- and y-components of lattice vectors in two directions as a function of image position. Using this information we can rectify a deconvoluted image as shown in Fig. 5 (c). In this image all columns align along straight lines, and it is clear that slowly varying image distortion is corrected.

Since relative relations of all column positions are known, intensity of each column position within a specified region will be automatically measured, when we specify only one

column position for Ga and As. **Figure 6** (a) to (c) show histograms of peak intensities at Ga, As and both column positions, respectively. Average intensity at Ga is 3.42×10^6 (σ = 1.9 ×10^5), while at As is 3.84×10^6 (σ = 2.0 ×10^5). Thus, we can significantly discriminate intensities at Ga and As, and determine a polarity of GaAs from a STEM-HAADF image. Although we have to examine a size of background of this image, which is a recent hot topic of STEM-HAADF imaging [12], the relative intensity between Ga and As is 1.12, which is close to a square of atomic number ratio (33/31).

Verification of Cs-correction Using Software
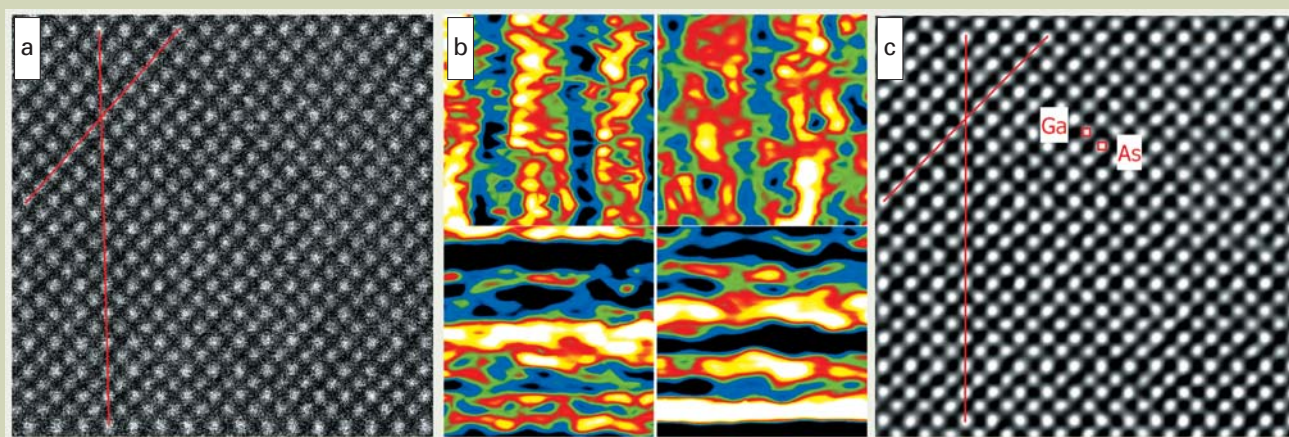
If spherical aberration is present, electrons

Fig.5 Measurement of lattice distortion and column intensity.

(a) STEM-HAADF image of GaAs [100] taken with JEM-2100F equipped with CEOS Cs-corrector for STEM. If we look carefully the image with a help of red reference lines, we can notice slowly varying image distortion.

(b) Pseudo-color display of variations of x- and y-components (left and right columns) of two lattice vectors close to horizontal and vertical directions (upper and lower rows) as a function of image position. FWHM's of these variations are about 2 pixels for lattice vectors of about 25 pixels. A variation of y-component of vertical lattice vector (lower right) is most significant, which corresponds to a change of a scan line distance.

(c) Deconvoluted image corrected for distortion using information on positional variation of lattice vectors as shown in (b). Atomic columns align on straight lines, and slowly varying image distortion is rectified. Here, intensity difference between Ga and As becomes more apparent than that in the original image.
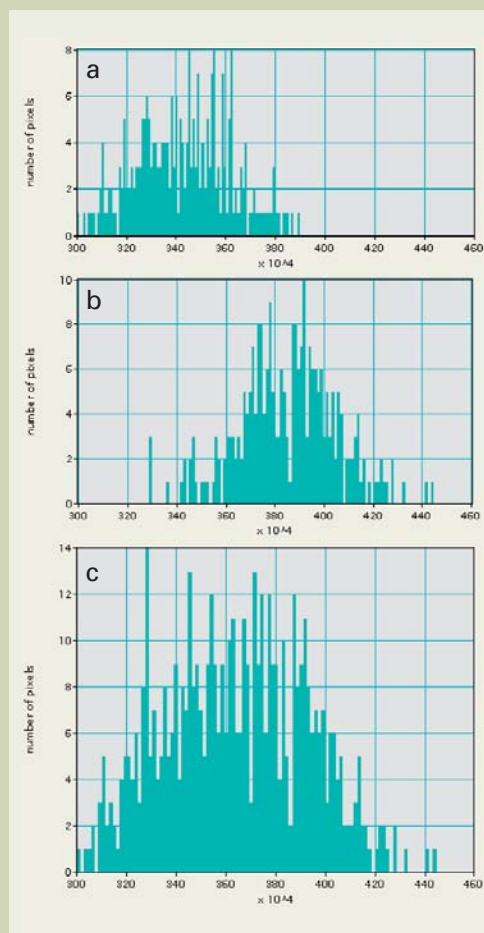

Fig.6 Intensity distributions of atomic columns of Ga and As.

Intensity of each column of Ga and As is automatically measured using information on relative lattice positions. (a), (b) and (c) show intensity histograms of Ga, As and both columns, respectively. Ga intensity is 3.42×10^6 (σ =1.9×10^5), while As 3.84×10^6 (σ =2.0×10^5).

scattered into high angle appear on the image plane displaced from an image corresponding to a transmitted wave. This is the reason why sets of lattice fringes appear outside of a particle, when we take an image of small particles. Likewise, lattice fringes extend into vacuum beyond a surface, or into other domain across an interface. One of the advantages of a Cs-corrected CTEM is such that this kind of image delocalization disappears, and a structure at a surface/interface becomes clear. Another advantage is such that a phase contrast from a specimen support, like a carbon film, which is a phase object, is suppressed, and observation of fine particles becomes easier. These advantages can be derived from correcting spherical aberration with software using a series of CTEM images. Moreover, software Cs-correction has further benefits over hardware Cs-correction as shown below.

Here, we will demonstrate that delocalization of lattice fringes on a CTEM image of Au particles disappear, and thus verify that software Cs-correction is in fact possible. We reconstruct here a wave front using FSR (Focal Series Reconstruction) function of FTSR (Focal and Tilt Series Reconstruction) plug-in. FTSR uses a specially designed Wiener filter[2] to estimate a wave front assuming the linear imaging that is valid when a transmitted wave is stronger than diffracted waves. Since the Wiener filter takes into account wave aberration, we can get a Cs-corrected wave front at a specimen exit surface.

Figure 7 (a) reproduces a CTEM image of nano-meter scale Au particles on carbon support taken with JEM-2100F (Cs = 0.5 mm). This image is selected from a through-focus series of 20 images (a defocus step is about 9 nm) to be used for Cs-correction, and a defocus value is about -46 nm (under focus). An

enlarged image (Fig. 7 (b)) of one spherical particle (about 6.5 nm) located at the center right clearly demonstrates sets of lattice fringes that appear outside of the particle. An expected displacement of a diffracted image for (311) reflection is 3.3 nm at this defocus. Figure 7 (c) and (d) are respectively an amplitude and phase distributions of the wave function at the specimen exit surface obtained from the through-focus series of 20 images. Spherical aberration was corrected assuming Cs = 0.5 mm. In addition, an estimated two-fold astigmatism of 5.9 nm was also corrected. Displaced lattice fringes observed in original images disappeared, and thus we can conclude that spherical aberration has been corrected successfully. The amplitude image corresponds to a just-focus image taken with a Cs-corrected CTEM. Here, phase contrast from carbon support is suppressed and thus observation of fine particles becomes as easy as a hardware Cs-corrected image.

The phase image shown in Fig. 7 (d) seems to be polluted when compared with the amplitude image. However, this is because carbon support film that is a phase object is faithfully observed here. The phase distribution of the wave function at the specimen exit surface obtained by using software is an aberration free image up to an information limit (diffraction limit), even though very low frequencies cannot be recovered. FTSR includes TSR (Tilt Series Reconstruction) function that uses the images obtained by tilting the beam at six directions. It is possible using TSR to reconstruct a wave front with a super resolution, which exceeds the information limit of an axial illumination.

When observing a phase object using a Cs-corrected CTEM the spherical aberration is not completely corrected, but adjusted from a few

microns to tens of microns, and then a defocus is tuned to a Scherzer focus corresponding to the adjusted Cs. This imaging condition in principle corresponds to a regular imaging condition proposed by Scherzer [13], although a spherical aberration is far smaller than that of a regular microscope. This means that an image taken at the Scherzer focus using a Cs-corrected CTEM is not an aberration free image. In order to observe a phase object using a Cs-corrected CTEM under an aberration free condition, wave front reconstruction using a series of through-focus images may be performed in the same way as applied to a regular CTEM. Here, attenuation of a phase contrast transfer function is also recovered at all frequencies except very low scatting angles, and thus an image with higher contrast than an unprocessed image will be obtained.

Observation of Oxygen with Software Cs-correction

It is widely accepted that a STEM-HAADF image can be interpreted easier than a CTEM image, since the contrast of a STEM-HAADF image does not reverse with a sample thickness nor defocus change, while a CTEM image does. Moreover discrimination of element is easy using a STEM-HAADF image, since a contrast is proportional to a square of atomic number. However, STEM-HAADF is not suitable to detect a light atom. It may be noted that if we correct aberration using software and estimate wave function at the specimen exit surface, the wave function does not depend on a defocus as a CTEM image. Moreover, if a specimen is thin enough, a phase distribution approximately reflects a projected potential of a specimen, and thus it becomes possible to detect a light atom and a
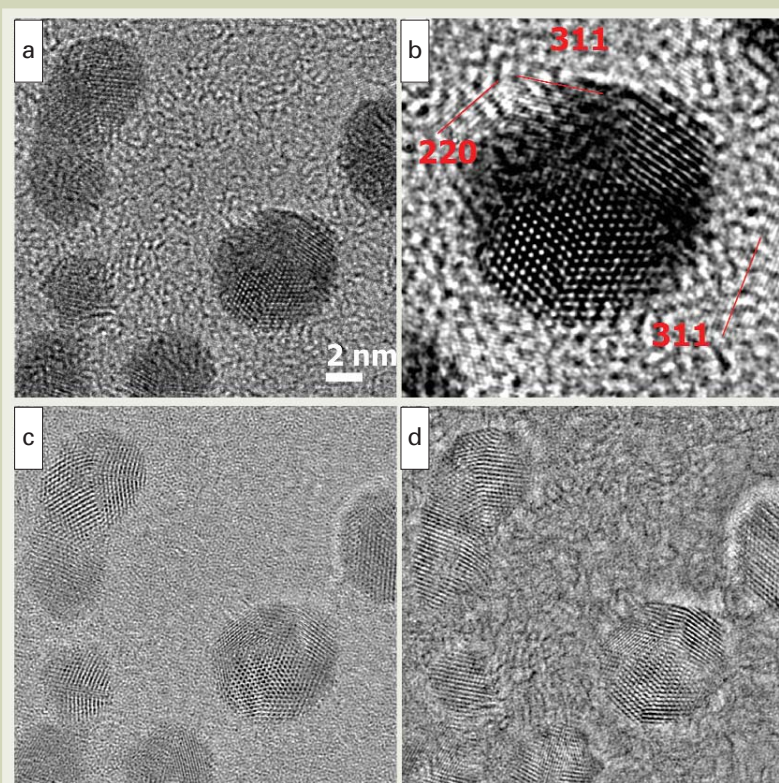

Fig.7 Verification of Cs-correction with software.

(a) CTEM image of nano-meter scale Au particles on carbon support taken with JEM-2100F (Cs=0.5mm). Defocus value of this image is about -46 nm, and sets of lattice fringes appear outside of particles.

(b) Magnification of a spherical particle (about 6.5 nm) at the center right of (a), where (311) and (220) lattice fringes that appear outside of the particle are evident. A plug-in, HREM-Filters Pro, is used to clarify the lattice fringes by suppressing aperiodic noise.

(c) and (d) Amplitude and phase distributions at the specimen exit surface obtained from the through-focus series of 20 images. Spherical aberration (0.5 mm) and estimated astigmatism (5.9 nm) are corrected here. Delocalized lattice fringes observed in the original images are vanished, which is a verification of spherical aberration correction. Amplitude image in (c) suppresses phase contrast from carbon support, and thus observation of fine particles becomes as easy as a hardware Cs-corrected image. On the other hand the phase image in (d) faithfully shows carbon support under the aberration-free condition.

specimen structure can be estimated more easily.

In this section we will try to detect oxygen in $SrTiO_3$. Figure 7 (a) shows an image of $SrTiO_3$ [001] taken with JEM-2100F (Cs = 0.5 mm) at around the Scherzer focus. A through-focus series of 20 images (a defocus step is about 9 nm) is acquired from this sample. Figure 7 (b) and (c) are respectively an amplitude and phase distributions of the wave function at the specimen exit surface obtained from the 20 through-focus images. They correspond to an area in the box indicated in Fig. 7 (a) close to the specimen edge. A spherical aberration of 0.5 mm is corrected in the same way as applied to the case of Au particles before. In addition, an estimated two-fold astigmatism of 4.9 nm was also corrected. The phase image close to the specimen edge shows a pattern corresponding to a structure model shown in the figure. Here, Sr and Ti-O columns show almost the same contrast. A weak contrast (red circle) at the center of a square made of Sr and Ti-O corresponds to oxygen. A dark contrast just inside of the sample along the sample edge is an equal thickness fringe. Since the first equal thickness fringe of this sample appears at a thickness of about 5 nm, a sample thickness should be less than 5 nm to obtain a phase image that simply reflects the model structure.

Brief Introduction of Other Plug-ins

Here, we will briefly introduce other plug-ins for quantitative electron microscopy developed at HREM Research for DigitalMicrograph.

♦ *DeConvEELS* improves an energy resolution of an EELS spectrum using the same principles used in DeConvHAADF [7, 14]

♦ *IWFR(Iterative Wave Function Reconstruction)* corrects spherical aberration for CTEM using a set of images. Contrary to FTSR this plug-in estimates a wave function at a specimen exit surface using an iterative algorithm. Normally, IWFR requires a fewer number of images to estimate the wave function than FTSR [3].

♦ *GPA(Geometrical Phase Analysis)* estimates lattice distortion from a single lattice image. Contrary to PPA this plug-in determines lattice distortion from phase distributions of the images separately calculated byinverse Fourier transform of different diffraction spots in a Fourier transform of the lattice image [10].

♦ *QPt(Quantitative Phase Technology)* estimates a phase distribution from two or three images based on the so-called transport intensity equation [15]. An electromagnetic field over a large area can be measured without an electron bi-prism and a vacuum reference area required by electron holography. On the other hand a spherical aberration can be corrected using phase information estimated from high-resolution images. Application of this technique to phase contrast microscopy of biological materials is anticipated in future [16, 17].

♦ *HREM-Filters* enhances periodic structure by reducing a contribution of aperiodic structure from the image (specimen support,quantum noise, etc). This plug-in is especially useful for the image of non-ideal periodic structure, where there are crystals with different orientations, a periodicity changes in direction, an image has distortion, and so on.). The periodicity is effectively enhanced by applying a Fourier filter, such as a Wiener filter, to each small area where a periodicity is uniform [18].

Conclusions

Quantitative electron microscopy using plug-ins developed for DigitalMicrograph (Gatan) has been demonstrated by making use of the data taken with JEM-2100F. By analyzing the data quantitatively we can deduce information from an observed data, which is hard to be detected by human eyes. Thus, we can add a new value to the observed data. We would like to encourage all the readers who have DigitalMicrograph on their microscope, to dig out useful information by quantitative electron microscopy from the data at hand.

The authors would like to thank to Prof. E. Abe, The University of Tokyo for giving us a permission to use a quasi-crystal data.

References

[1] W. Coene A. Thust, M.Op de Beeck, and D. van Dyck,, *Ultramicroscopy* **64** (1996)109.

[2] R. Meyer, A. Kirkland and W. Saxton, *Ultramicroscopy* **92** (2002) 89.;R Meyer, A.Kirkland and W.Saxton, *Ultramicroscopy* **99**(2004)115.

[3] L.J. Allen, W. McBride, N.L. O'Leary and M.P. Oxley, *Ultramicroscopy* **100** (2004) 91.

[4] Gatan, Inc. www.gatan.inc

[5] S.J. Pennycook and D.E. Jesson, *Ultramicroscopy* **37** (1991) 14.

[6] A.J.McGibbon, S.J.Pennycook and D.E. Jesson, *J. of Microscopy* **195** (1999) 44.

[7] K. Ishizuka, *Microsc Microanal* **11** (2005) 1430.

[8] M. Haider, H. Rose, S. Uhlemann, E. Schwan, B. Kabius and K. Urban, *Ultramicroscopy* **75** (1998) 53.

[9] S. Taniguchi and E. Abe, Phil. Mag. (2008) in press.

[10] M.J. Hytch, E. Snoeck and R. Kilaas, *Ultramicroscopy* **74** (1998) 131.

[11] P.L. Galindo, S. Kret, A.M. Sanchez, J-Y. Laval, A. Yanez, J. Pizarro, E. Guerrero, T. Ben, S. Molina.*Ultramicroscopy* **107** (2007) 1186.

[12] D.O. Klenov and S. Stemmer, *Ultramicroscopy* **106** (2006) 889.

[13] O. Scherzer, *J. Appl. Phy.* **20** (1949) 20.

[14] K. Ishizukia, K. Kimoto and Y. Bando, Microsc Microanal 9 (2003) 832;K. Ishizuka, *Kenbikyou* **39** (2004) 204 (in Japanese).

[15] M.R. Teague, *J. Opt. Soc. Am.* **73** (1983) 1434.

[16] K. Ishizuka and B. Allman, *J. Electron Microsc.* **54** (2005) 191.

[17] K. Ishizuka, *Microsc Microanal* **11** (2005) 2160; K. Ishizuka, *Kenbikyou* **40** (2005) 188 (in Japanese).

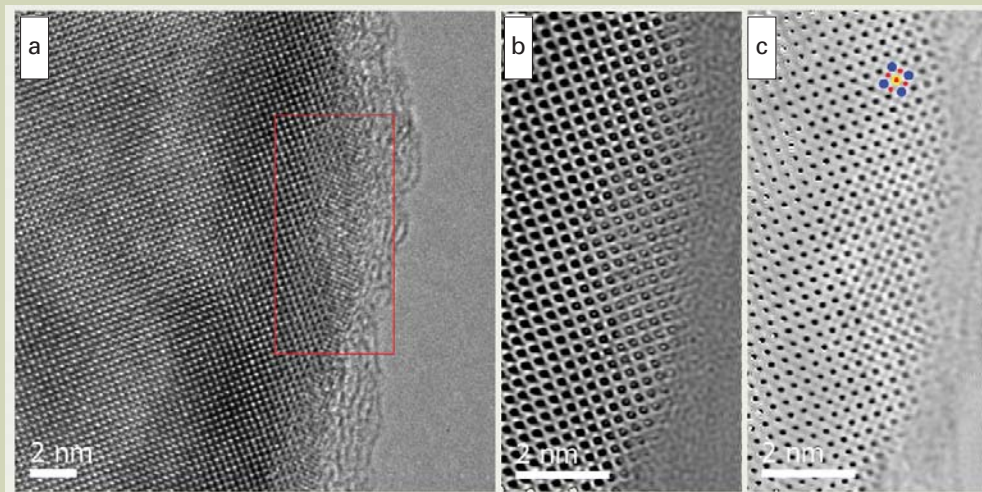[18] K. Ishizuka, P.H. C. Eilers, T. Kogure, *Microscopy Today* 2007, 16.

Fig.8 Observation of oxygen with software Cs-correction.

(a) CTEM image of $SrTiO_3$ [001] taken with JEM-2100F (Cs=0.5 mm) close to the Scherzer focus. An equal thickness fringe is observed just inside of the sample along the sample edge.

(b) and (c) Amplitude and phase distributions at the specimen exit surface obtained from the through-focus series of 20 images. They correspond to an area inside of the rectangle box shown in (a). Contrast corresponding to the model structure is observed in the phase image close to the specimen edge, whose thickness is less than the one yielding the equal thickness fringe. In the structure model, blue, yellow and red circles represent Sr, Ti and oxygen, respectively. Weak contrast at the center of the square made of Sr and Ti-O corresponds to oxygen.

Case Study on Failure Analysis by Electron Beam Absorbed Current Method

Y. Ueki, J. Kinashi, Y. Tasaki, T. Nabeya, T. Kawaguchi, M. Todome, H. Wakamatsu and T. Miyazaki

Test System Development Dept., TOSHIBA Microelectronics Corp

In LSI failure analysis, the electron beam absorbed current method is becoming widely used as a technique for localizing open/short failure in LSI-interconnects.

This paper reports several results where this method was used for the LSI failure analysis and some knowledge of usage which was acquired through these studies.

Keywords: Failure Analysis, Electron Beam Absorbed Current, LSI-interconnects, Failure localization.

Introduction

With recent shrinking of feature size and increasing number of metal layers in integrated circuits, determination of the physical root cause by failure analysis is becoming extremely difficult. Especially, due to the multi-layered structures, the case of the failure factor existing in dielectric layer such as Via that connect two metal layers has been increased. In this case, localization of failure site by the layer analysis (Top-Down surface observation for each layer) seldom reaches to the physical root cause, thus cross-sectional observation is required. For cross-sectional observation, improvement of accuracy for precise failure site localization, where a cross-sectional imaging and analysis should be performed, leads to the improvement of determination for physical root cause.

As a method for localizing open/short site in LSI-interconnects, utilizing electron beam ability for focusing, transmission and absorption, the advantage of Resistive Contrast Imaging (RCI) has been reported. In Japan, this method is called "Electron Beam Absorbed Current method." Thus, in this papaer, we describe this method as the Electron Beam Absorbed Current method [1-8].

In this paper, using a JEOL Beam Tracer, authors report the results of appllication of the Electron Beam Absorbed Current method to localize LSI failure sites and some knowledge of usage acquired through our study.

Flowcharts for Localizing Failure Sites

In localizing the LSI failure sites, suitable

methods are applied depending on failure modes. In general, for DC failure, Optical Beam Induced Resistance Change (OBIRCH) and an emission microscope, for SCAN failure, a softaware diagnosis tool, for function failure other than SCAN failure, an emission microscope and for memory failure, a fail-bitmap technique are used. In recent years, Dynamic Laser Stimulation (DLS) analysis has started to be used for localizing AC failure [9], [10]. These techniques and tools enable us to localize the failure site from the entire chip level down to the functional block and cell level. A rough guideline for the area of localization using these methods is about a 100 μm square. However, to perform a cross-sectional observation, the area of localization should be achieved at least down to a 100 nm square. For example, in case of LSI interconnects failure, it is necessary to localize accurate failure sites along interconnect with 100 nm width, or specify just one Via that connects interconnects fixtured in different layers. In case of cell failure, it is necessary to specify one defective transistor within multiple trangistors.

Figure 1 shows the flowcharts for localizing failure sites down to 100 nm square range. For interconnects failure, the Electron Beam Absorbed Current method is used, and for cell failure, Nano-probing analysis is applied.

Analysis Examples Using Electron Beam Absorbed Current Method

Some examples using the Electron Beam Absorbed Current method in Fig.1, are demonstrated to localize AC contacts and short-failure in LSI-interconnects.

Short-failure in LSI interconnects

Figure 2 shows an analysis example of func-

tion failure in a half-pitch(hp) 130 nm System on a Chip (SoC) product. The analysis result using an emission microscope indicated two anomalous emissions on the chip. Then, the interconnect that connects with each cell at an anomalous emission site was referred with layout diagram. Then it was found that the total length of this interconnect was 3 mm and also, the target analysis area was spread to a wide area of 1.25 mm × 0.65 mm. In this analysis, the Electron Beam Absorbed Current method was used to localize the area down to a 100 μm square, so that physical analysis can be performed. As a result, an extra interconnect, which is different from defective interconnect was detected on an absorbed current image. This result suggested that a short-site exists on the defective interconnect. The absorbed current image and the short candidate site on layout data are shown on **Fig 3**.

The layer analysis was performed till the top surface of Al interconnect for the short candidate site, but no abnormal phenomenon was observed. However, the absorbed current image suggested a high possibility of the existence of a failure in this site. Thus, we polished the Al interconnect but left barrier metal and observed the layer again. As a result, a particle at the bottom of barrier metal on M3 layer was identified as a cause of the shortage. The results of layer analysis were shown on **Fig 4**. Generally, layer analysis was not performed in such detailed observation. But in this case, a failure site was successfully localized to an area of about 5 μm × 1 μm by an absorbed current image. Thus, we concentrated on analyzing this area, and then the physical root cause of the failure was determined.

High resistance failure in Via

Analysis example of AC failure in an hp 90 nm SoC product is described here. This failure is a temperature-dependent SCAN failure. We localized a failure site using the flowchart
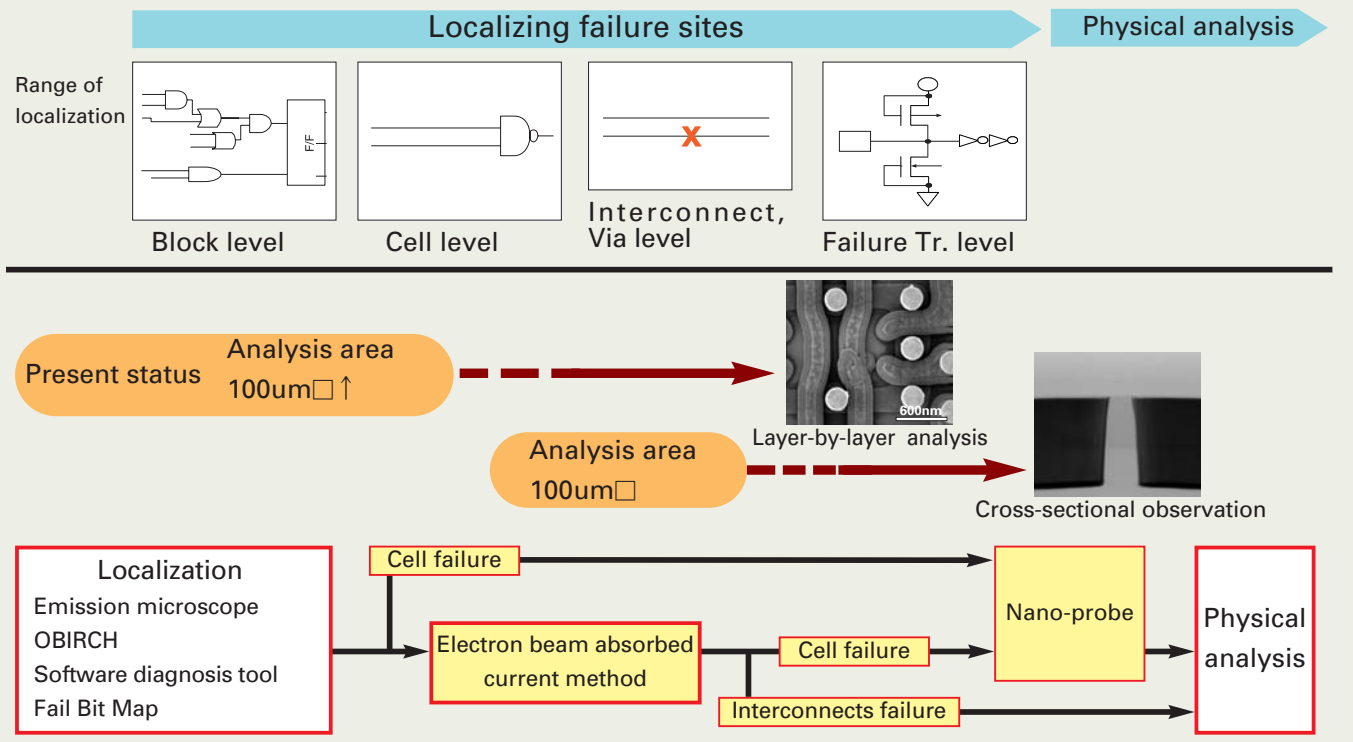
3500, Matsuoka, Oita, 870-0197, Japan

E-mail : makoto.todome@tosmec.toshiba.co.jp

Fig.1 Flowcharts for localizing failures sites.
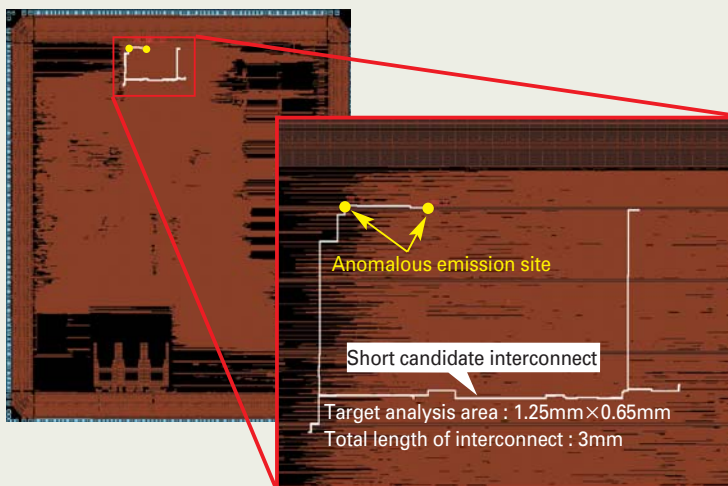
Fig.2 Short candidate interconnect.
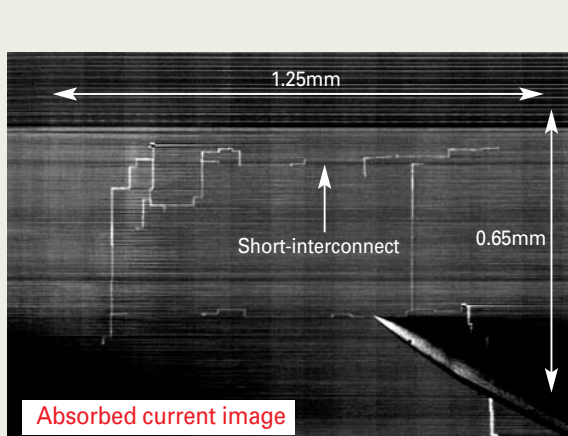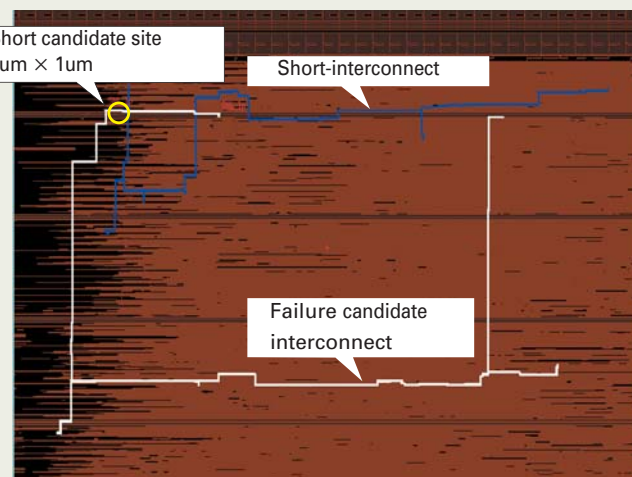
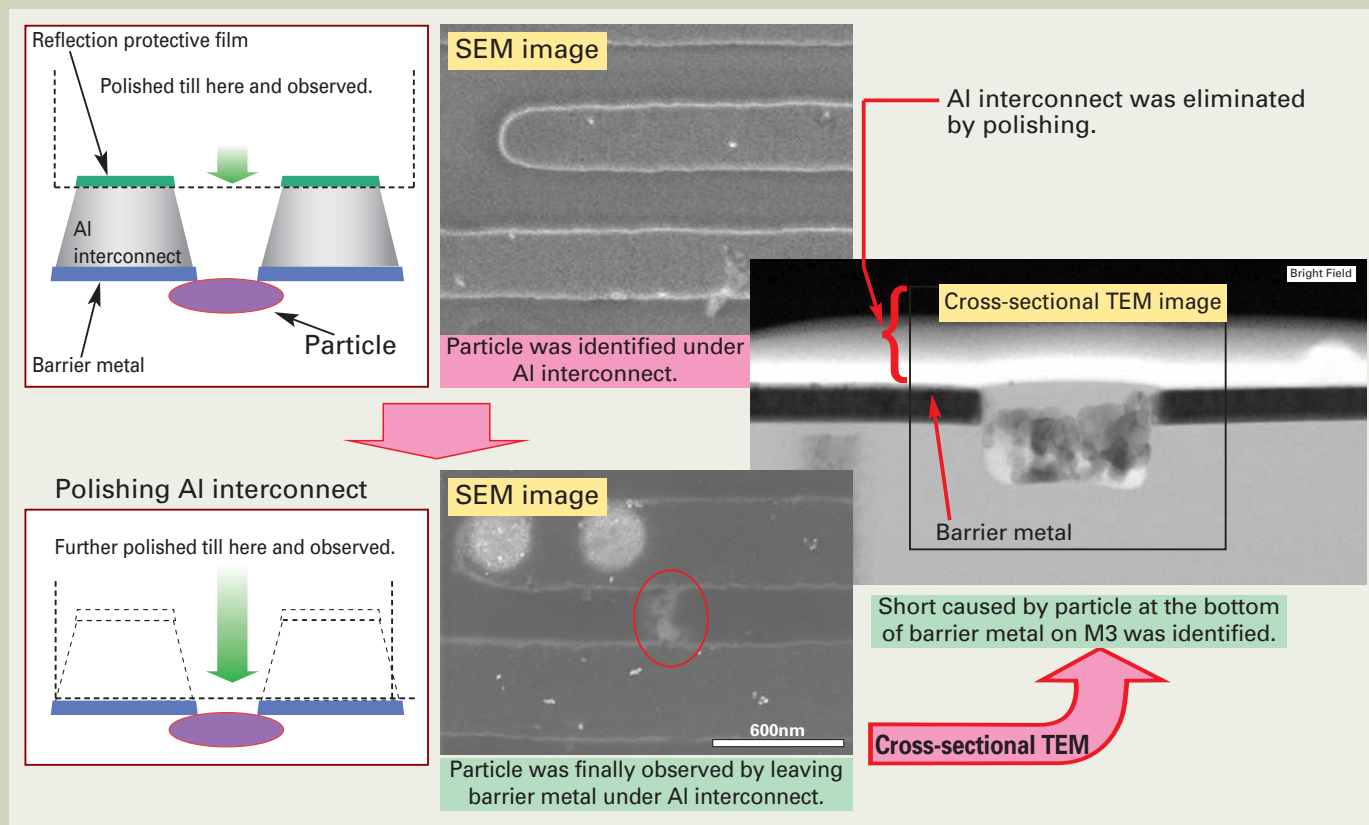Fig.3 Absorbed current image and short candidate.
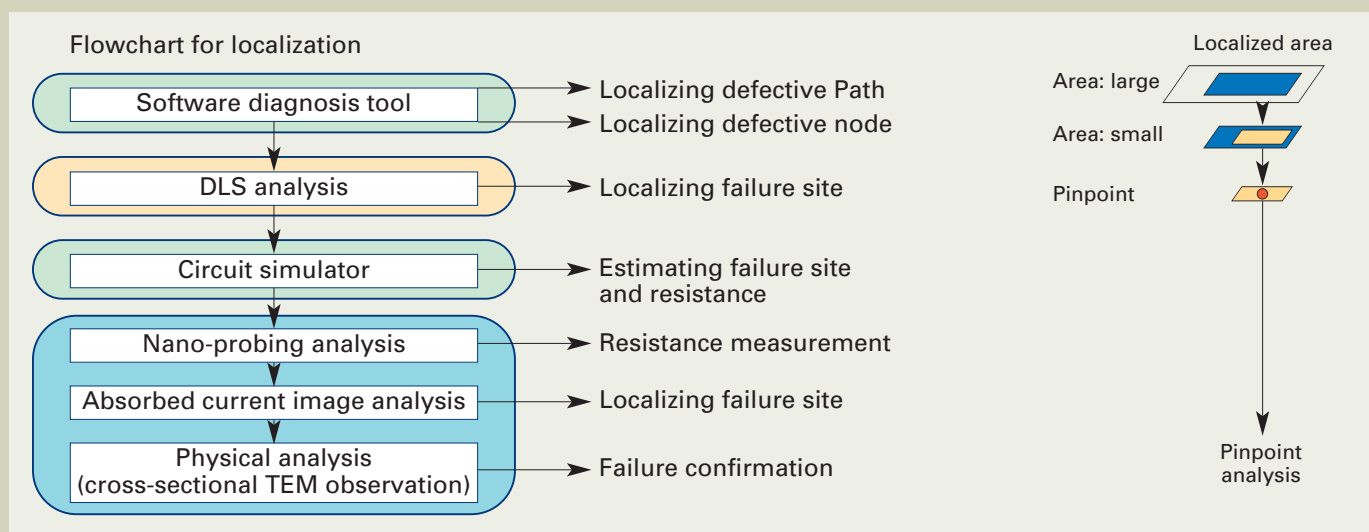
Fig.4 Results of layer analysis.

Fig.5 Flowcharts for localizing AC failure.

shown in **Fig 5**.

Since this failure has a temperature dependence, Dynamic Laser Stimulation (DLS) was applied to a candidate of defective interconnect and node, both of which were extracted from a software diagnosis tool. (Although DLS is generally referred to Soft Defect Localization (SDL), we call DLS in this paper.) DLS result and a superimposed image of a defective node with DLS mapping are shown in **Fig 6**. This result indicated that the DLS sensitive area exists on the node extracted from the software diagnosis tool, so the failure site was highly assumed to be in this area.

On a circuit simulator, we increased the resistance at failure candidate site with several times, and simulations were carried out. Then the reproducibility of the failure phenomenon had been confirmed when a resistance increased to several million Ω. After this confirmation, the resistance of this interconnect was measured with a Nano-probing technique. From this Nano-probing measurement, it was confirmed that the resistance at room temperature was about 12 MΩ and that at high temperature was about 300 Ω. These resistances corresponded to the results of simulations.

Furthermore, from the absorbed current image of this interconnect, the contrast of defective interconnect was changed in the site shown in **Fig 7**. This result also corresponded to the DLS analysis. As a result of comparing with layout diagram, it was revealed that Via exists in this site. Then, a cross-sectional observation of this Via was performed, indicating that a void exists in the Via. This void was considered to be caused during filling process of the hole.

In this example, all results from various analysis tools were in good agreement, so it was said that the accuracy of the localization was sufficiently high. Also, it was found that the Electron Beam Absorbed Current method could give useful information for failure localization.

Low resistance failure in Via

Figure 8 shows an analysis example of function failure on an hp 90 nm SoC product.

In this example, an emission microscope analysis detected anomalous emission and this result suggested an open failure in the interconnect between the cell and the emission site. As a result, cross-sectional TEM observation indicated open Via in this interconnect. However, in the process of the localizing, an
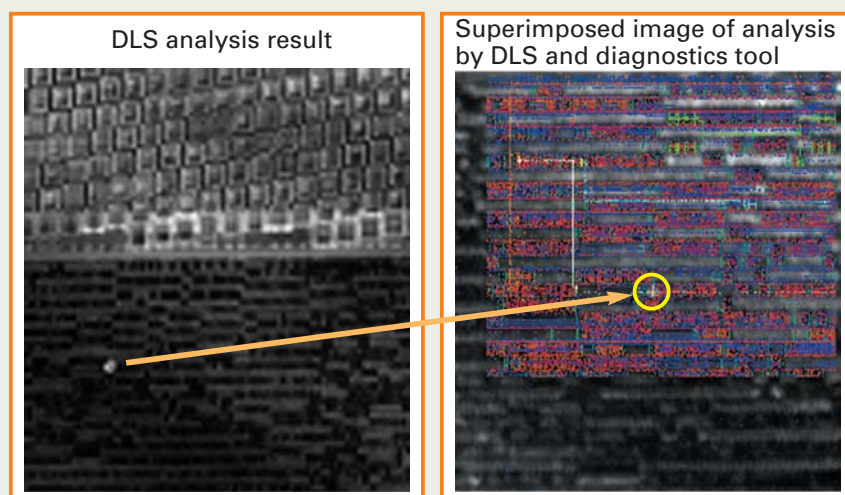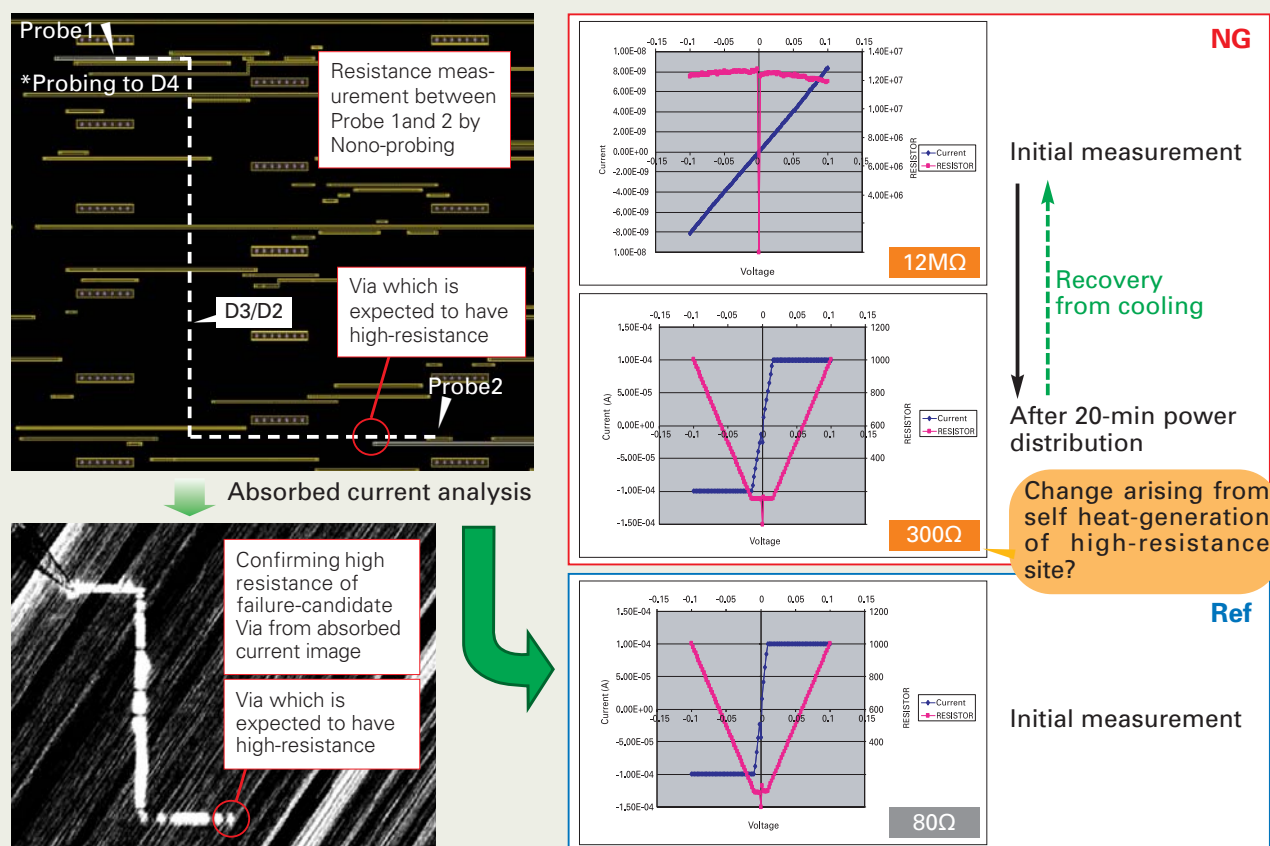
Fig.6 Results of DLS analysis.

Fig.7 Results of Nano-probing mesurement.

image of Electron Beam Absorbed Current method did not give any contrast at open Via. An absorbed current image by Beam Tracer and the cross-sectional image of open site by Transmission Electron Microscope (TEM) are shown in Fig. 8. In the absorbed current image, whole interconnect, which combined the cell and the emission site was able to be observed. From this result, we took it for granted that there was no failure sites along this interconnect. However, from the result of emission microscope, there should be a failure site along this interconnect, so we concentrated on just Via along this interconnect then performed cross-sectional TEM observation, then we identified the open Via shown in Fig. 8.

The result of cross-sectional TEM observation clarified that the space between the Via and the interconnect is very thin about 17 nm. This suggests that a resistance at this point should be relatively low.

To detect such a low-resistance failure site using the Electron Beam Absorbed Current method, we found that a lower primary electron beam current was required. **Figure 9** shows the variations of absorbed current images when the probe current was set to 36 pA and 530 pA while the accelerating voltage was varied from 10 kV, 13 kV, to 15 kV. In the case of a probe current of 530 pA, regardless of the accelerating voltage (10 kV, 13 kV, 15 kV), whole interconnect appeared on the images. On the other hand, in case of a probe current of 36 pA, the boundary of the contrast at the failure site was recognized at an accelerating voltage of 10 kV. However, when the accelerating voltage was increased to 13 kV and 15 kV, it became difficult to recognize the

boundary at the failure site. In Fig.8, although the interconnects are located on the same fourth metal layer (M4), the absorbed current image showed a featureless dark contrast. Thus, the open failure is expected to exist on the Via between the interconnects on the fifth metal layer (M5).

This result indicates that, in order to detect a low-resistance open failure, it is necessary to reduce the probe current and the accelerating voltage. However, by suppressing the probe current and the accelerating voltage, the image contrast becomes poor, so to increase the detection rate of low-resistance open failure and to get fare contrast of the image are a trade-off relation. In general, in order to improve the image contrast, the probe current and the accelerating voltage are set relatively higher. However, when the prioritizing the
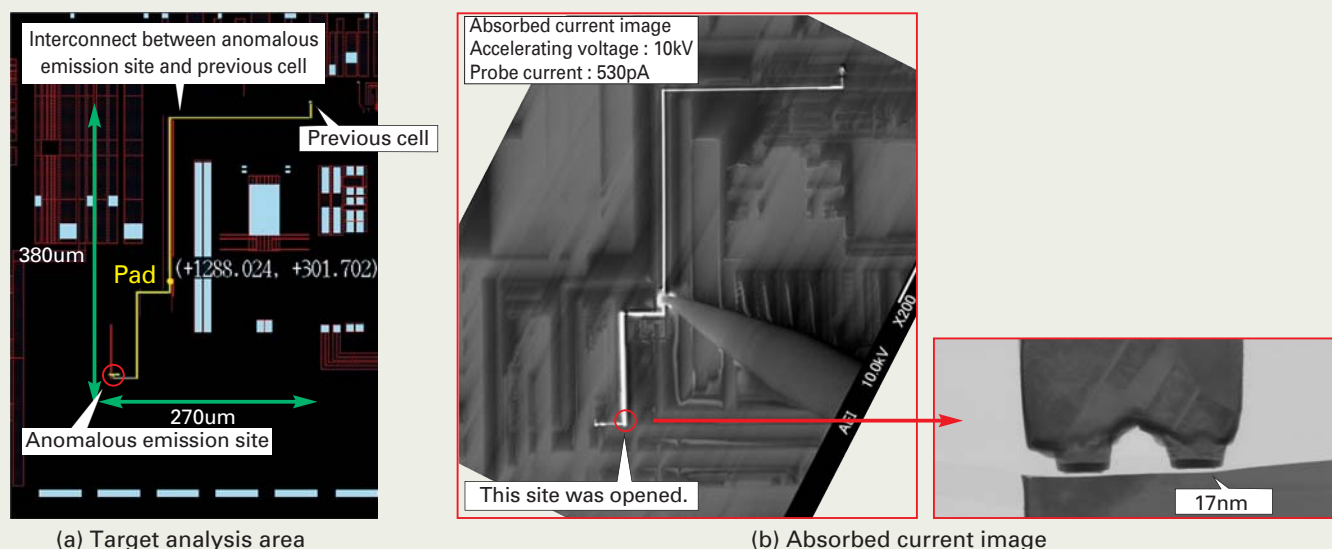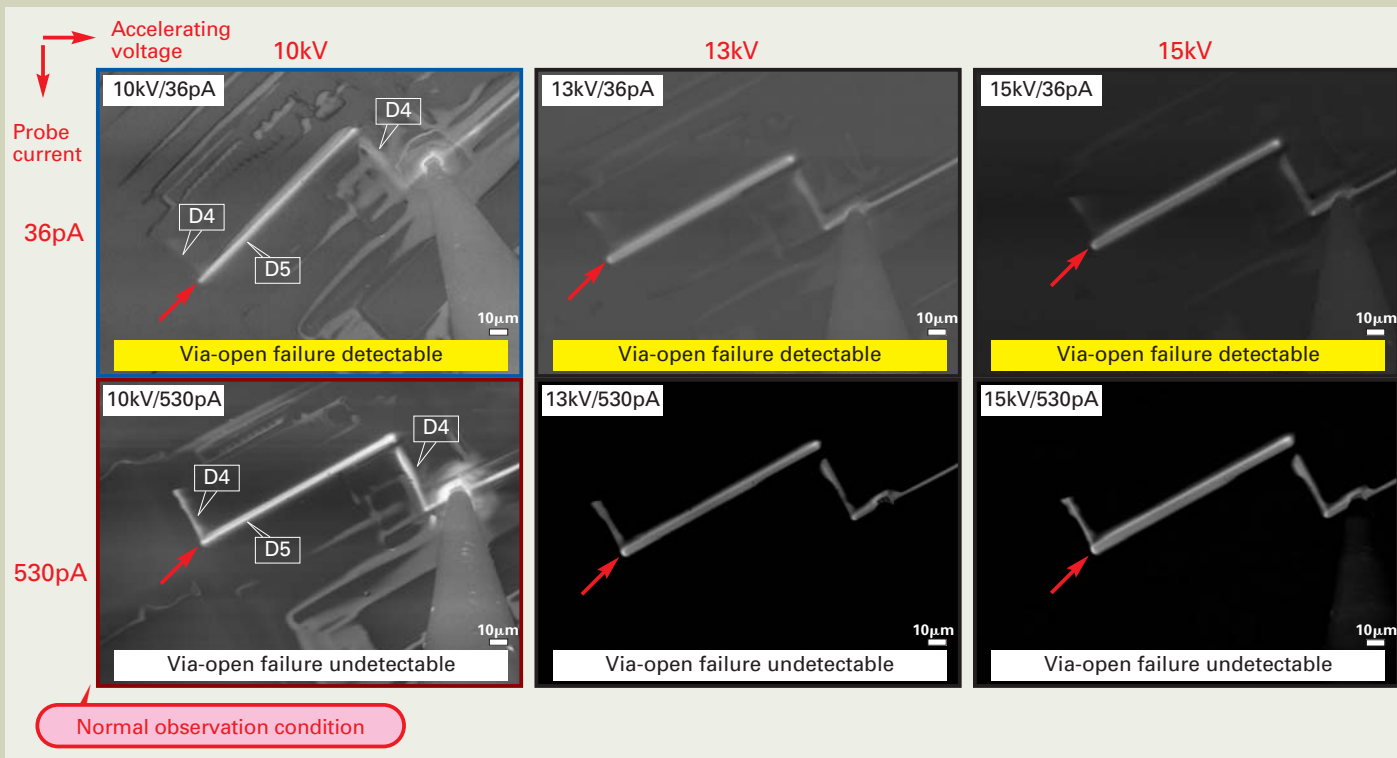
Fig.8 Results of absorbed current analysis.

(a) Target analysis area

Interconnect between anomalous emission site and previous cell

Previous cell

380um

Pad (+1288.024, +301.702)

270um

Anomalous emission site

(b) Absorbed current image

Absorbed current image
Accelerating voltage : 10kV
Probe current : 530pA

This site was opened.

17nm

Fig.9 Absorbed current image with variations of probe current and accelerating voltage.

Accelerating voltage

Probe current

10kV   13kV   15kV

36pA

10kV/36pA   D4   D4   D5
Via-open failure detectable

13kV/36pA
Via-open failure detectable

15kV/36pA
Via-open failure detectable

530pA

10kV/530pA   D4   D4   D5
Via-open failure undetectable

13kV/530pA
Via-open failure undetectable

15kV/530pA
Via-open failure undetectable

Normal observation condition

prevention of improper contrast at the low-resistance open failure, it is necessary to start observation from lower probe current and lower accelerating voltage to higher.

On this sample, observation by two probes method was also performed. **Figure 10** shows absorbed current images obtained with one probe and two probes, respectively. In the case of one probe, whole interconnects are appeared on the image at a probe current of 36 pA and 500 pA. No boundary of the contrast is recognized at the open failure site. On the other hand, in case of two probes, a clear boundary of the contrast appears at the open failure site at both 36 pA and 500 pA. This result demonstrates that when two probes method is available, the low-resistance open failure can be detected regardless of high and low probe current.

Discussion on an undetectable low-resistance open failure

In the present study, when one probe was used for detecting the absorbed current, some results showed that whole interconnects were seen as the absorbed current image even if these interconnects contained a low-resistance open failure. This will lead to the misunderstanding of failure localization process in LSI failure analysis. Thus, in order to prevent misunderstanding of failure sites localization process, we made a physical model for this phenomenon and obtained the optimum observation conditions.

Figure 11 shows the equivalent circuits for device, where an Electron Beam Absorbed Current method was applied. In addition, Fig. 11 also shows the total equivalent circuit including an electron microscope, which was considered to be the corresponding power supply. When the probe current is 36 pA, the boundary of the contrast along the interconnect appeared and disappeared depending on the value of accelerating voltage. To keep constant probe current of 36 pA, when the voltage of power supply (accelerating voltage) changes, the output impedance Z of the power supply needs to be changed. When the probe current is 36 pA and an accelerating voltage is 10 kV, that is the condition of $Z \ll R$, low-resistance open failure site can be observed. Here, R denotes the resistance at failure site. And when the probe current is 36 pA and an accelerating voltage is set to 13 kV or more, that is the condition of $Z \gg R$, low-resistance open failure site cannot be observed. This model is considered to hold even for the case where the probe current is changed at a
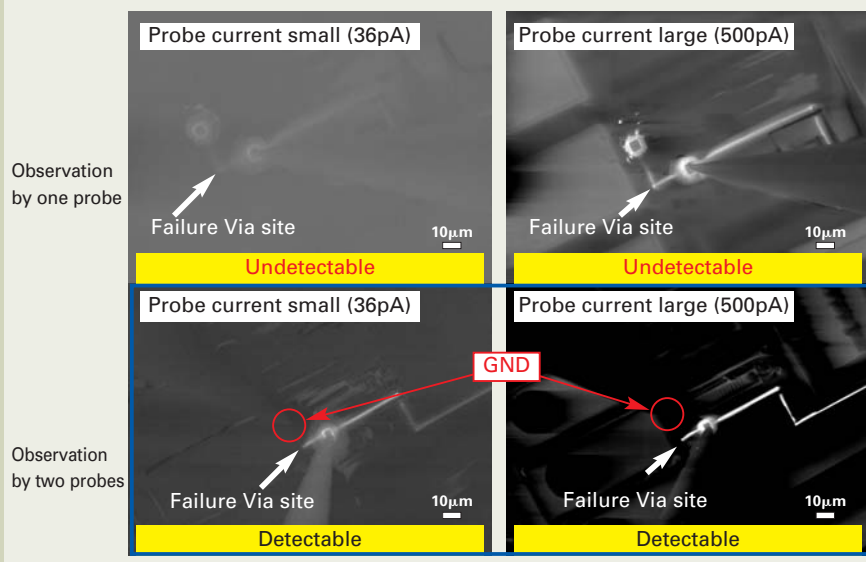
Fig.10 Comparison of absorbed current image obtained with one probe and two probes.
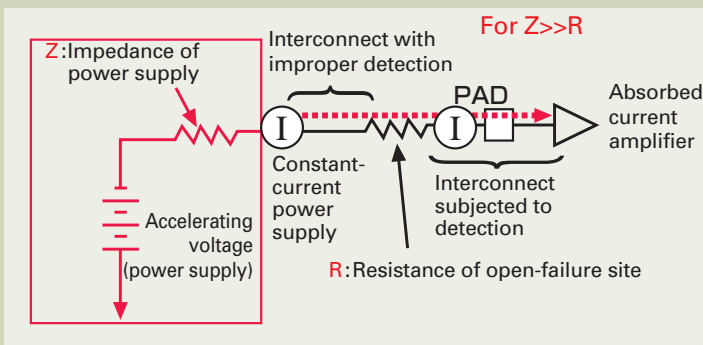

Fig.11 Equivalent circuits for device, including an electron microscope considered as the corresponding power supply.
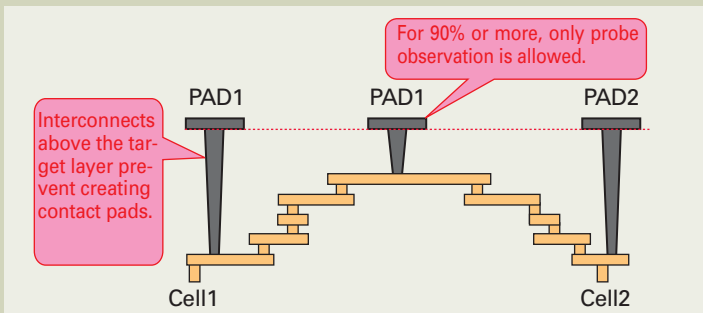

Fig.12 Restrictions for two probe observation.

constant accelerating voltage.

This model equation for impedance Z of the power supply is described as below.

Z = a (sample depending constant)× Vacc (accelerating voltage)× Ip (probe current)

Further examination and experiment will be expected in the future for this model equation.

In observation by two probes, one probe is connected to ground potential. Thus, no matter how high the impedance Z is, an open-failure site is recognized in the absorbed current image. But in the failure analysis for actual devices, limitations of the layout prevent us from using two probes method. So, about 90 percent or more of the devices, only one probe observation can be allowed. In **Fig 12** the limitations are listed for observation by two probes.

In the case of observation by one probe, in order to prevent improper detection of a low-resistance open failure site, it is necessary to set the accelerating voltage and the probe current to lower values.

Conclusion

The Electron Beam Absorbed Current method was applied to the localizing of failure sites of actual devices, and the following knowledge was acquired.

1) By combining a software diagnosis tool, an emission microscope and DLS with the absorbed current image, AC failure sites can be localized.
 The Electron Beam Absorbed Current method can give useful information for improvement of the accuracy to localize failure sites.

2) In observation by one probe, the absorbed

current image may cause improper detection of failure sites under some observation conditions.

Based on the knowledge acquired from this study, we will clarify the model that explains the conditions for improper detection in observation by one probe. And furthermore, we will examine detectable resistance in LSI interconnects.

Acknowledgement

References

[1] Graig Allyn Smith et al., " Resistive Contrast Imaging: A New SEM Mode for Failure Analysis," IEEE Transactions on electron devices, Vol. ED-33, No. 2, Feb. (1986).

[2] K.Mizukoshi, T.Oyamada, Y.Matsumoto, S.yorisaki, A.Simase, T.Majima, K.Koyanagi and M.Nozoe," Fault Localization in LSI-Interconnects Using Electron Beam Absorbed Current Analysis," LSI Testing Symposium 2003 Proceedings(2003) (In Japanese).

[3] Y.Imanaga, S.Nagamine, M.Kurihara and M.Todome, " Failure Analysis of Interconnects in 65nm Node Device Using Electron Beam Absorbed Current Method," LSI Testing Symposium 2005 Proceedings(2005) (In Japanese).

[4] T.Hashimoto, M.kurihara, Y.Imanaga, M. Todome and Y. Ueki, "Failure Localization Technique Utilizing Electron Beam Absorption Current Method." (2006) (In Japanese).

[5] A.Uchikado, T.Okubo, S.Yamahashi, T.Oyamada, S.Kawanabe and A.Shimase, " Analytical Efficiency and Analytical Success Rate Improvemet From Failure Diagnosis To Breakdown Cause Investigation That Use IDDQ Test," LSI Testing Symposium 2005 Proceedings(2005) (In Japanese).

[6] J. Kinashi, Y. Ueki, M. Todome and M.Kurihara, " Enhancement of the Detection Sensitivity of Electron Beam Absorbed Current Method, " LSI Testing Symposium 2006 Proceedings (2006) (In Japanese).

[7] Y. Mizushima, T. Kimura, M. Sato and T. Nakamura, " Failure Analysis of Cu/Low-k Interconnects Using Electron Beam Absorbed Current Images," *JEOL News* **Vol. 42,** No. 1, 31-35 (2007).

[8] Y. Ueki, J. Kinashi, T. Nabeya, Y. Tasaki, T. Kawaguchi and M. Todome, " Case Study on the Failure Analisis by Electron Beam Absorbed Current Method" LSI Testing Symposium 2007 Proceedings (2007) (In Japanese).

[9] S.Ito,Y.Tando and T.SaIkai, " Circuit Analysis of Failure LSI Device Using SDL," LSI Testing Symposium 2005 Proceedings (2005) (In Japanese).

[10] T.Harada, K.Norimatsu, K.Urata, Y.Tasaki, M.Nakamura, Y.Nakanishi, and H.Wakamatsu " Development of the dynamic failure analysis Using DLS method." LSI Testing Symposium 2007 Proceedings (2007) (In Japanese).

Recent Advances in Transmission Electron Microtomography for Materials Research

Hiroshi Jinnai

**Department of Macromolecular Science and Engineering,
Graduate School of Science and Engineering,
Kyoto Institute of Technology**

This featured article summarizes recent advances in an emerging three-dimensional (3D) imaging technique, transmission electron microtomography (TEMT), and its applications to a class of "soft materials", i.e., polymer-related materials such as nanocomposites and block copolymers. With some recent developments made in TEMT, it is now possible to obtain *truly* quantitative 3D structural data in subnanometer resolution. It is also demonstrated that, with the combination of TEMT and other experimental technique, e.g., the scattering, it becomes possible to study nano-structures that have been difficult to characterize before. The structural information obtained from the 3D imaging provides a good opportunity not only to gain essential insight into the physics of self-assembling processes and the statistical mechanics of long chain molecules but also to establish the "structure-property" relationship in polymeric materials.

Introduction

Polymer materials are ubiquitous in our daily life. They often consist of more than one species of polymers and thus become multi-component systems. The most simple and representative examples are polymer blends [1, 2] and block copolymers [3]. Due to repulsive interaction between the constituent polymers, the multi-component polymer materials often involve "phase-separation." Studies to characterize the phase-separated structures inside the materials have been growing intensively over the past three decades. Academic interest in the complex fluids (to which polymeric systems belong) as well as a ceaseless industrial need for developing new materials activated such studies.

In academia, pattern formation and self-assembling processes of polymer blends are one of the most fascinating research themes in non-linear, non-equilibrium phenomena. The block copolymers, consisting of multiple, chemically dissimilar sequences covalently linked together, likewise self-organize (equilibrium) phase-separated nanometer-scale

Matsugasaki, Sakyo-ku, Kyoto 606-8585, JAPAN

hjinnai@kit.ac.jp

structures (termed as "microphase-separated structures") due to the presence of chemical junctions inside the molecule. When phase-separated, the block copolymers need to place their chemical junctions at the interface between the microdomains and the block chains must uniformly fill the corresponding microdomains in the most entropically favored way. Due to such constraint, the block copolymers normally form hightly-periodic nano-structures. In industry, deep understanding of such phase-separated polymer systems is also important to create nanomaterials with superior physical properties. The structure-property relationship in multi-component polymeric materials is of significant importance, basic studies on which eventually render new design of polymer materials satisfying the diverse requirements of industry.

Up to now, morphological studies of the multi-component polymeric materials have been carried out by various microscopic and scattering methods. Optical microscopes, transmission electron microscopes (TEM), scanning electron microscopes (SEM) and atomic force microscopes (AFM) are commercially available and widely used. The biggest advantage of the microscopy is to provide real-space representations of morphologies. However, when it comes to "measurements,"

especially in a quantitative manner, the microscopy sometimes lacks statistical accuracy due to the small field of view. In contrast, the scattering methods provide much superior statistical accuracy to the microscopy simply because the observation volume is much larger than that of the microscopes. One must remember, however, that the scattering methods require "(hypothesized) models" for data analysis: The scattering methods *do not* provide intuitive insight into the morphologies as the microscopy does. After all, for the complete characterization of the morphology, one may need to know the morphologies first by the microscope and subsequently to evaluate the structural parameters by the scattering on the basis of the morphology: The two methods are complementary.

Recently, the phase-separated structures, especially the microphase-separated structures, are becoming increasingly complicated with the advance of the precision polymerization. Identification of such complex morphologies becomes more and more problematic. Micrographs taken by TEM are often inconclusive, which makes the interpretation of the accompanying scattering data difficult. The microscopes mentioned above take two-dimensional (2D) (transmitted or surface) images of three-dimensional (3D) objects. The

more complicated the morphologies are, the less convincing the 2D images usually become. It is quite natural to develop new microscopes that are capable of obtaining 3D images.

Laser scanning confocal microscopy (LSCM) has been developed in the 1980s and widely used first in the biological community for 3D direct observations of cell morphologies. After a slight delay, it has become popular in the materials community. In polymer society, LSCM was first used to observe the bicontinuous morphology of a polymer mixture during the spinodal decomposition [4-6]. X-ray computerized tomography (X-ray CT) is another technique for 3D imaging that has similar spatial resolution: a micrometer-resolution. The biggest advantage of X-ray CT to LSCM is the strong penetrative power of the X-ray so that it can be readily used for opaque materials. Although quite useful, these two microscopes are not appropriate for nanometer-scale structures.

Transmission electron microtomography (TEMT) is an emerging technique for the 3D structural observations for polymer nanotechnology. Although the first paper using TEMT appeared as early as 1988 by Spontak *et al.* [7] in polymer society, it has not been extensively used until recently when the high-speed and large-scale computing became available to the scientific community. In the new millennium, TEMT is becoming more frequently used around the world not only in polymer science [8, 9] but also other materials science [10-12] and biology [13]. Thus, the contents of the present featured article can be universally applicable to many fields of science.

Recent Development in Transmission Electron Microtomography (TEMT)

In the TEMT experiments, a series of tilted transmitted images (projections) is taken by TEM, which is used to reconstruct tomograms on the basis of computerized tomography (CT). The tomograms are then stacked to generate a 3D reconstructed image ("3D reconstruction"). There is an intrinsic limitation of angular range for the tilting experiment available in TEM, resulting in a "missing wedge" of structural information in the Fourier space [see the following section for details]. Due to the missing wedge, resolution along the direction parallel to the optical axis of the microscope (the dimension perpendicular to the plane of the specimen), i.e. the Z-direction, is reduced compared to that in the specimen plane [14]. In addition to this primary effect, a less appreciated but probably critical effect of the missing wedge is that the imaging of objects in the 3D reconstruction, especially anisotropic ones, depends strongly on their angle relative to the tilt axis. This effect will be detailed in the forthcoming section below. Although the cylindrical and lamellar morphologies of the block copolymers could be influenced by the latter effect in the TEMT observations, none of the previous studies considered the effect [7].
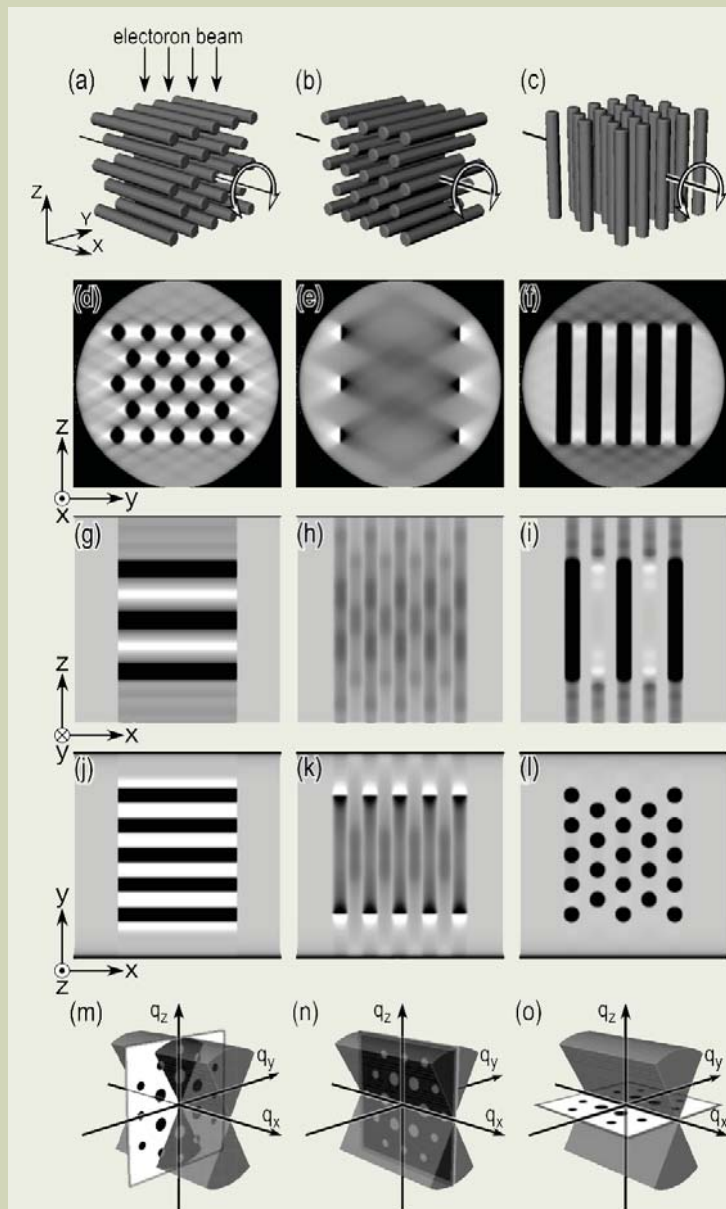

Fig.1 Demonstration of the effect of geometrical relationship between the direction of tilt axis and the orientation of cylindrical nanodomains on 3D reconstruction. There are three types of geometrical relationships. Each column shows a model, three cross sections of 3D reconstruction and a "missing wedge" in the Fourier space (shown by the gray volume), from top to the bottom. The cylindrical nanodomains rotate around the tilt axis from - 60° to 60° with a 1° increment. Tilt axis is always along the X-direction. The electron beam comes from the top (from the Z-direction). An X-Z cross section is a tomogram where the filtered back projection (FBP) is carried out. In the bottom-most row, diffraction patterns from the infinitely-long cylinders are shown together with the missing wedge. Because the missing wedge is the volume where no projections can be sampled, diffraction spots within this wedge cannot contribute to the resulting 3D reconstruction.
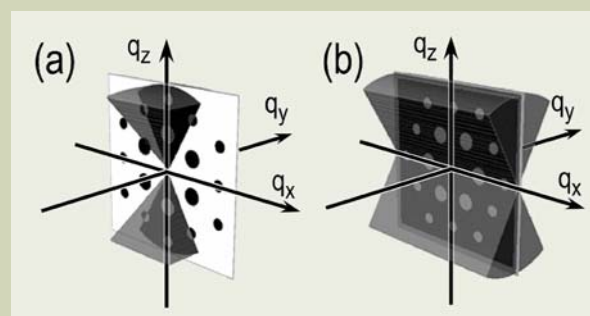
Fig.2 Comparison of the missing volume in the Fourier space between (a) dual-axis tomography and (b) single-axis tomography. Directions of the tilt axes in the dual-axis tomography are along q_x and q_y axes. In single-axis tomography, the tilt axis is along the q_x axis. Hexagonally-packed infinitely-long cylindrical morphology aligned along the Y axis as shown in Fig. 1(b) gives a diffraction pattern only in the q_x - q_z plane. Some of the diffraction spots are outside the "missing pyramid" and hence the cylinders can be reconstructed in dual-axis tomography [part (a)], while all diffraction spots are inside the "missing wedge" in single-axis tomography [part (b)].

Dual-Axis TEMT

A problem in a single-axis TEMT: The "Missing Wedge" problem

Figure 1 shows a simulation of the single-axis TEMT for cylindrical morphologies. As shown in Fig. 1(a) to 1(c), three different geometries of the cylinders with respect to the tilt axis and orientation were simulated. In these figures, the hexagonally-packed cylinders orient in three different directions while the tilt axis is fixed to the X-direction. The cylinders were tilted around the tilt axis typically from - 60° to 60° with an increment of 1°, from which the filtered back projection method [15, 16] was used to obtain tomograms. Figures 1(d) to 1(l) display cross sectional images of the 3D reconstruction. In the Y-Z plane, the cross sections (d) and (f) that correspond to the model (a) and (c) were properly reproduced. On the other hand, the cross section (e) from the model (b) was poorly reconstructed; The horizontal stripes should be

observed. Figs. 1(g) to 1(i) and Figs. 1(j) to 1(l) show, respectively, the X-Z and X-Y planes. Although the cross sections relevant to the model (a) and (c) were obtained with reasonable accuracy, again, the cross sections corresponding to the model (b) [see Figs. 1(h) and 1(k)] were not correctly reconstructed. In fact, judging only from the cross sectional images obtained from the model (b), i.e., Figs. 1(e), 1(h) and 1(k), one could misidentify the 3D structure with the lamellar morphology whose lamellar normal aligned to the X axis. Thus, if the orientation of the cylindrical nanodomains geometrically satisfies the relation with the tilt axis as shown in Fig. 1(b), it is very likely that the cylinders *do not* appear in the 3D reconstruction.

This problem can be understood by considering a relationship between a projection in the real space and the Fourier space. The "central slice theorem," upon which CT relies, states that the Fourier transformation of a projection at a given angle is a central section at the same angle through the Fourier transform of that

object [15]. Namely, each projection will equate to part of an object's Fourier transform. Therefore, in principle, tomographic reconstruction is possible from an inverse Fourier transform of the superposition of a set of Fourier transformed projections. If some projections are missing due to the limited angular range of TEM, then the Fourier space is undersampled in those directions. The unsampled volume in the Fourier space becomes wedge-shaped and thus is called the "missing wedge." As a consequence of this unsampled volume, the back transform, the tomogram of the object, will be degraded. Figures 1(m) to 1(o) demonstrate the missing wedge in the Fourier space (translucent gray volume) and "diffraction patterns" of the cylindrical nanodomains relevant to the geometries shown in Figs. 1(a) to 1(c), respectively. In the case of Figs. 1(m) and 1(o), part of and all of the diffraction spots are outside the missing wedge, and hence it is feasible to obtain the reasonable 3D reconstructions. In fact, the image quality of the 3D reconstruction of model (c) appears to be the
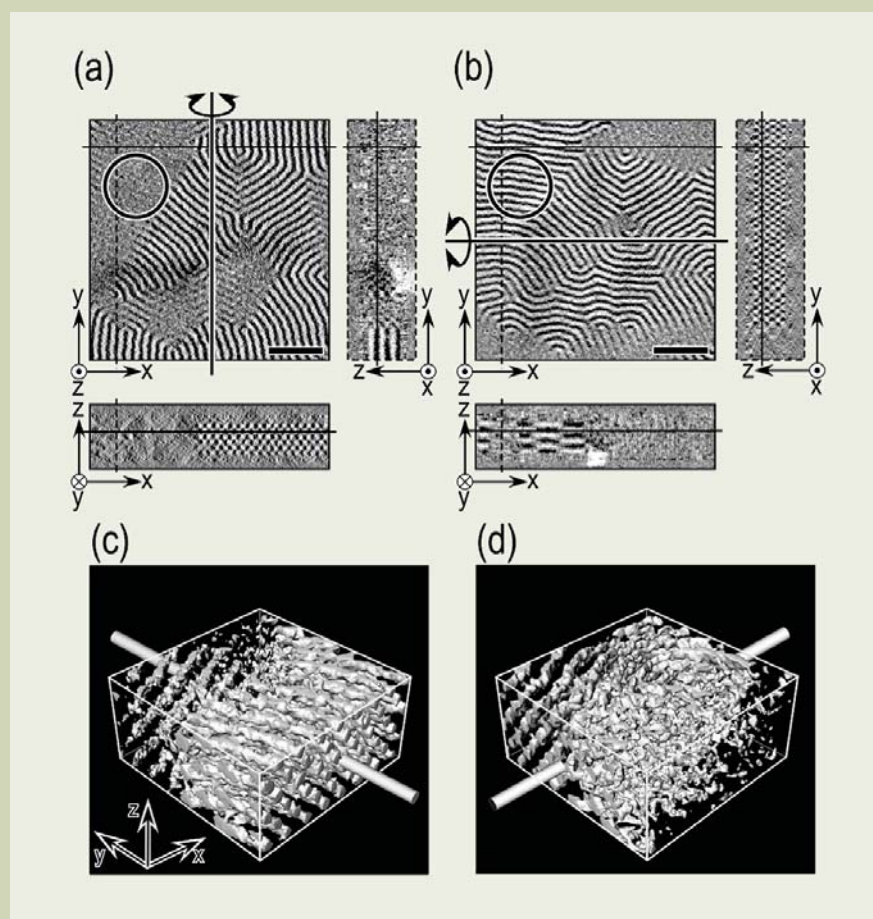

Fig. 3 Orthogonal cross sectional views of two 3D reconstructions at the same position of the specimen. Tilt axes lie along (a) Y- and (b) X- direction, respectively. In parts (a) and (b), as indicated by the circles, some cylindrical nanodomains were not reproduced in part (a) but were nicely reconstructed in part (b) and vice versa. Solid and dashed lines in the cross sections represent positions where each slice was cut in the 3D reconstructed data. Parts (c) and (d) show surface-rendered 3D images, where the PS region has been made transparent. Tilt axes are indicated by solid rods. Scale bar in parts (a) and (b) shows 200 nm. Box size of the 3D image is 250 nm × 250 nm × 115 nm.
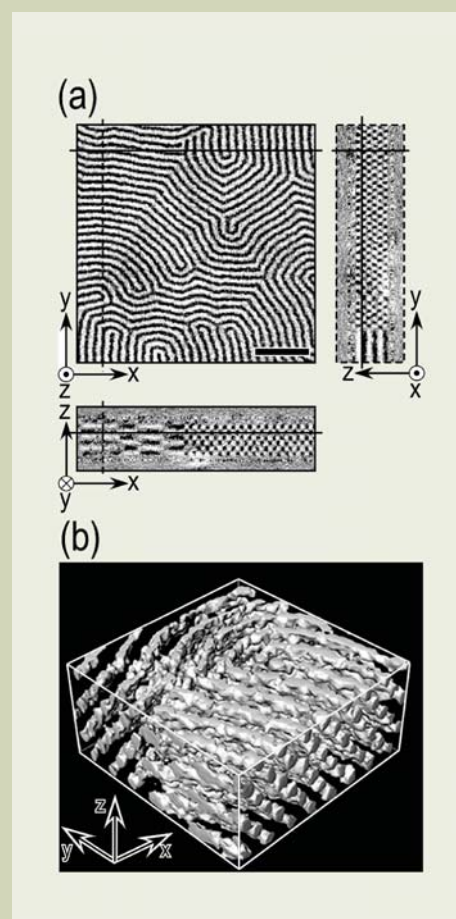
Fig. 4 (a) Orthogonal cross sectional views of 3D reconstructions obtained from dual-axis tomography. Positions of the cross sections are exactly the same as those in Fig. 3. Black phase is PI microdomain. Cylindrical microdomains are completely reconstructed not only in the X-Y plane but also in the other two orthogonal cross sections. Scale bar shows 200 nm. (b)Surface-rendered 3D images obtained from dual-axis tomography, where the PS region has been made transparent. Box size of the 3D image is 250 nm × 250 nm × 115 nm.

best among the three geometries [see Fig. 1(l) for example]. On the other hand, all the diffraction spots are inside the missing wedge in Fig. 1(h), resulting in an insufficient 3D reconstruction.

One of the most effective ways to solve this problem is to minimize the volume of the missing wedge. Increasing the tilting angle of the specimen may be one possible way, however, this strategy would not help much especially in the case of the 3D observation of cylindrical morphology as demonstrated in Fig. 1(b). Another strategy is to have another tilt axis in addition to the first one. **Figure 2** demonstrates such "dual-axis tomography": In Fig. 2(a) the unsampled volume of the dual-axis tomography is shown. Compared with the missing wedge shown in Fig. 2(b) [that is the reproduction of Fig. 1(n)], the unsampled volume in the dual-axis tomography, called the "missing pyramid," becomes *considerably* smaller than the missing wedge. Some of the diffraction spots of the cylindrical nanodomains are now outside the missing pyramid even in the case of the geometry shown in Fig. 1(b), Penczek *et al.* [17] pioneered the dual-axis tomography for thick biological sections, followed by Mastronarde [18].

Dual-axis TEMT on a cylindrical microphase-separated structure

Figure 3 shows the results of a 3D reconstruction of a cylinder-forming poly(styrene-*block*-isoprene) (SI) copolymer. Experimental details can be found elsewhere [14].

Figures 3(a) and 3(b) display, respectively, orthogonal views of the two 3D reconstructed volume data with the tilt axes in different directions, i.e., the Y- and X-directions. The solid and dashed lines in each cross sectional slice represent positions of the other two orthogonal slices. The thickness of the each digitally-sliced cross section in Figs. 3(a) and Figs. 3(b) is equal to the edge length of a voxel, i.e., 1.9 nm. These images were outstandingly clear due to essentially no overlap of the nano-structure. The cross sectional slice will be called a "digital slice" throughout this paper. We note here that one of the biggest advantages of TEMT is that it obtains truly 3D information on intact block copolymer morphology by digital sectioning, instead of physically cutting the materials into slices.

The two 3D reconstructions show exactly the same volume of the specimen except for the direction of the tilt axis. It is clear that the SI block copolymer exhibited PI cylindrical morphology. The cylinders lay parallel to the film surface. The thickness of the film was determined to be ca. 160 nm from the cross sections in the X-Z plane in Fig. 3(a) and Y-Z plane in Fig. 3(b). It was found that there were 6 layers of cylindrical nanodomains in the film as observed from the X-Z plane in Fig. 3(a) and Y-Z plane in Fig. 3(b).

It is quite intriguing that some parts of the 3D reconstruction either in Fig. 3(a) or in Fig. 3(b) were not properly reconstructed: the horizontally-oriented cylinders shown by a circle in the X-Y plane of Fig. 3(a) were *vaguely* visible, while they were *clearly* visible in the X-Y plane of Fig. 3(b). As described earlier, the cylinders in this area fulfilled the geometrical relation as shown in Fig. 1(b), and hence they were not properly reconstructed in Fig. 3(a).

On the other hand, the same cylinders were parallel to the tilt axis (X-axis) in Fig. 3(b), corresponding to the situation shown in Fig. 1(a). Thus, they were successfully reconstructed [Fig. 3(b)].

The interface between the PI and PS nanodomains were found by binarizing the morphologies in the X-Y plane and was modeled according to the marching cubes algorithm (MCA) [19]. Figures 3(c) and 3(d) show surface-rendered 3D images of the SI block copolymer corresponding to those displayed in Figs. 3(a) and 3(b), respectively. The tilt axes are indicated by rods. The volume fraction of the PI microdomains evaluated from Figs. 3(c) and 3(d) were, respectively, 0.16 and 0.15, in contradiction to the known composition of the copolymer, 0.22.

The two 3D reconstructed data were combined in the Fourier space, the detailed protocol of which can be found elsewhere [14]. Orthogonal views of the combined 3D reconstruction are displayed in **Fig. 4**(a) together with a corresponding surface-rendered 3D image in Fig. 4(b). Because the positions of the orthogonal views in Fig. 4(a) are exactly the same as those in Figs. 3(a) and 3(b), it is now obvious how much the dual-axis tomography can improve the single-axis 3D reconstructions: Not only in the lateral plane (X-Y plane) but also in the cross sectional planes, i.e. the X-Z and Y-Z planes, cylindrical microdomains were visible regardless of their orientations. The volume fraction of the PI domains evaluated from the surface-rendered image was ca. 0.22.

TEMT without "missing wedge"

In the previous section, the dual-axis TEMT was introduced to reduce the missing wedge in TEMT. Although the missing region in the Fourier space can be significantly reduced by the dual-axis TEMT, the most faithful tactics for the CT is to tilt the specimen over ±90°. In this section, we demonstrate a complete rotation of a rod-shaped specimen of a zirconia/polymer nanocomposite made by a
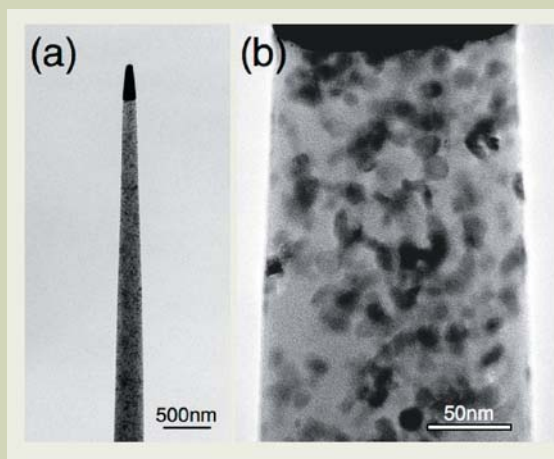
Fig.5 (a) An electron micrograph of a rod-shaped polymer nanocomposite containing zirconia fillers. A black region at the tip of the specimen was the tungsten deposited before the fabrication by FIB.
(b) An enlarged electron micrograph of the thinnest region of the rod-shaped specimen.

Fig.6 Orthogonal views of 3D reconstruction of zirconia/polymer nanocomposite. The lines in each cross section represent the positions of the other two orthogonal cross sections (dotted line, X-Z plane; dashed line, X-Y plane; dot-dashed line, Y-Z plane).

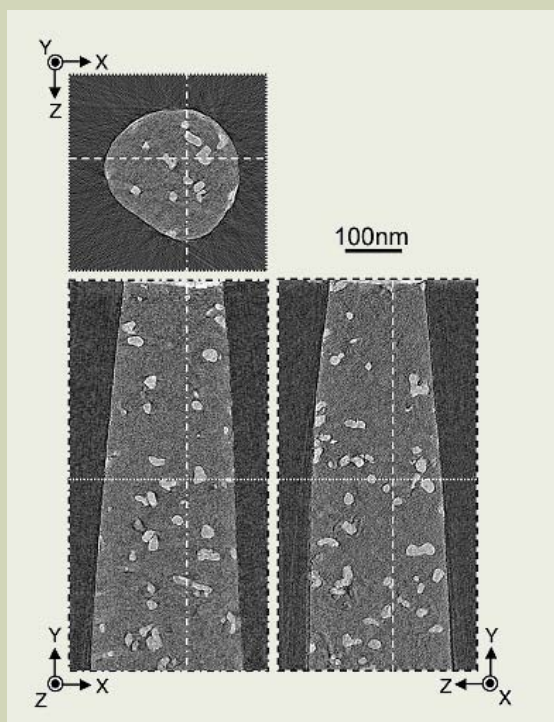focused ion beam (FIB) method that was attached at the tip of a specially modified specimen holder without any supporting film. A complete set of tomograms has been generated from 181 projections that were taken over the angular range of ±90° on a nm scale [20].

Figure 5(a) shows an electron micrograph of the rod-shaped specimen. The 5 ~ 20 nm zirconia grains were observed as black domains in the polymer matrix in the enlarged electron micrograph [Fig. 5(b)]. No sign of damage occurring in the FIB fabrication process, such as melting by the gallium ion beam or the re-deposition of contaminations, was observed on the surface of the rod-shaped specimen. Note that the applicability of the FIB to polymer materials has also been confirmed on an SI block copolymer [21].

An orthogonal view of the reconstructed 3D image of the zirconia/polymer nanocomposite is shown in **Fig. 6**. The gray region and white small objects are, respectively, the thermoset polymer matrix and zirconia domains. The FBP calculation has been carried out in the X-Z plane, in which the edge of the rod-shape specimen and the zirconia domains were observed. The conventional TEMT in which the angular range is limited to ±60° shows artifacts at the top and bottom of the X-Z plane, and the objects are elongated along the Z-axis [see also **Fig. 7**] [22]. It is quite impressive that the 3D reconstruction of the nanocomposite is totally free from such artifacts. Moreover, the Y-Z plane, which usually exhibits the worst image quality in the conventional TEMT, appeared as clear as the other two cross sectional slices.

Image artifacts due to the limitation of the angular range prominently appear in the X-Z plane. Because we have the complete data set with ±90° angular tilting, it is worthwhile to demonstrate how the maximum tilt angle affects the image quality in the TEMT experiments. A series of 3D reconstructions with various maximum tilt angles, α, was made. Namely, 3D images were reconstructed from exactly the same TEM tilt series and alignment within the angular range of ±α°. Figure 7(a) shows the X-Z cross sections of the same region of the rod-shaped specimen from α = 40° to α = 90° in 5° increments. As α decreased, the image quality, especially the contrast between the zirconia grains and polymer matrix, became worse, and also the edge of the rod-shaped specimen became more like a "pear-shape." Note that the angular range is normally limited to α = 60° ~ 70° in the conventional TEMT observations using planar sections. Although the positions and approximate shapes of the zirconia grains can be observed especially in the case of a small α, they were elongated and some details of the structure were lost.

It is of particular interest in material science as to how accurately one can determine the structural parameters, e.g., volume fraction, ϕ, of the zirconia grain. ϕ was measured as a function of α and is displayed in **Fig. 8**(a). The error bar in each measurement was associated with some uncertainty of the threshold in the binarization. ϕ decreased as α increased and approached a certain asymptotic value for a high α ($\alpha > 80°$). The known composition of the zirconia grain was 0.055 ±0.005 from the preparation of the sample (dotted line), which is in excellent agreement with the measured asymptotic value, i.e., 0.055. The elongation of the zirconia grains and low signal-to-noise (S/N) ratio of the tomograms may be the cause of deviation from the true value at small α. It is worthwhile to note that we observed a 27% error in ϕ for the conventional TEMT, i.e., α = 60°, in our zirconia/polymer nanocomposite. Furthermore, we recognized that the angular range of α ~ 70° may be required in order to attain a 10% error in ϕ in the nanocomposite.

A New Structural Analysis Based on TEMT

TEMT [23] is an ideal tool to characterize nano-structures and, as such, it has proven useful for providing high-resolution 3D information on a variety of polymeric structures, e.g., block copolymer nano-scale microphase-separated structures [7, 24-27, 8], polymer/clay nanocomposite materials [28], carbon black/natural rubber composites [29], *etc*. Some of these studies provided *quantitative* structural analysis as well as 3D pictures. For example, topological features, e.g., connectivity of the network, can be also evaluated from 3D images [30].

Although TEMT is used alone to characterize the nano-scale morphologies in most cases, it provides even richer structural information when used together with other techniques. One example is the "TEMT-assisted computer-simulations" in which the simulations are carried out on the basis of 3D images obtained from TEMT. The stress-strain (S-S) behavior of a rubbery material was simulated using the combined technique of TEMT and 3D FEA (Finite Element Analysis) [31]. The virtually obtained S-S behavior was in good agreement with the experimental results obtained by stretching the actual macroscopic specimens. Moreover, the combined technique provides local strain upon stretching inside the materials. Similarly, the local frustration of the block chains, being essential in the block copolymer self-assembly, can be evaluated by the combined method of TEMT and 3D meso-scale computer simu-

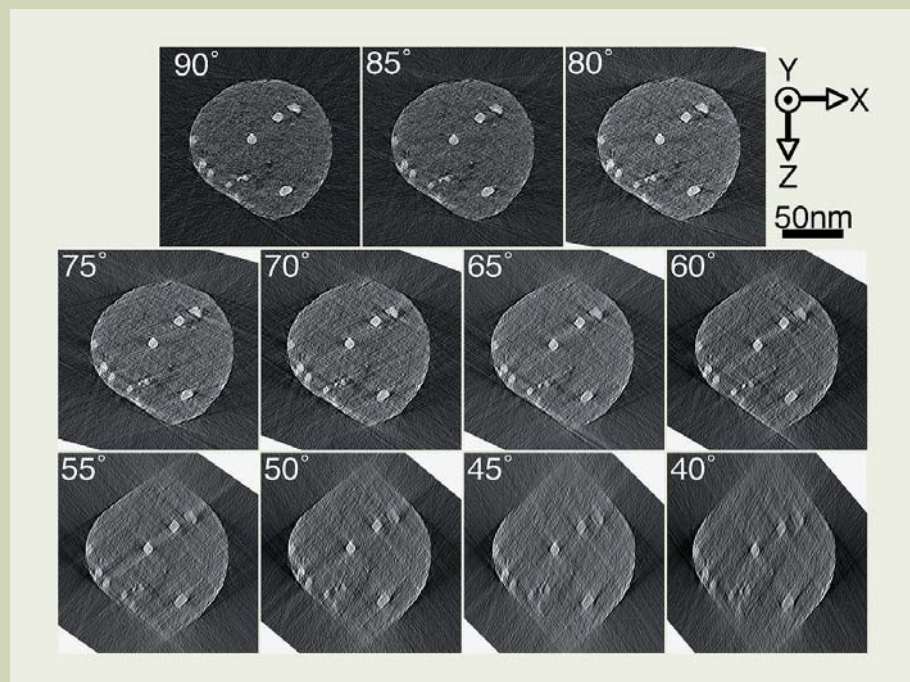
Fig.7 A series of X-Z cross sections of the same region in the rod-shaped specimen reconstructed with various maximum tilt angles, α, from 40° to 90° in 5° increments.
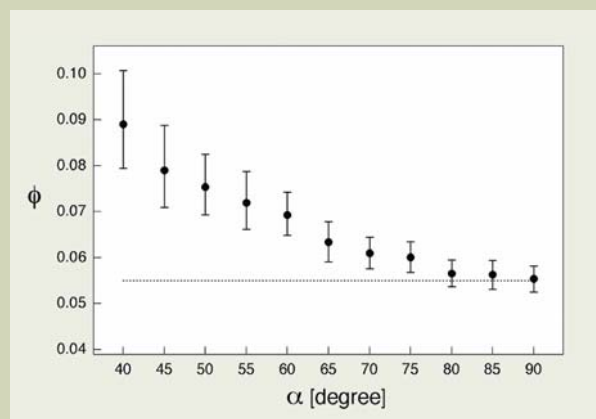

Fig.8 Plot of volume fractions of zirconia, ϕ, experimentally determined from the 3D reconstruction series from α = 40° to α = 90°. Dashed line represents the known composition of the zirconia grain.

lations [32]. We will show two examples in which spectroscopic and reciprocal-space methods are used together with TEMT, respectively, in the two forthcoming sections below.

A nanocomposite consisting of nano-fillers in a rubbery matrix: Element-specific TEMT

Nanocomposites have attracted substantial interest from researchers because they often exhibit unexpected properties synergistically derived from the two or more components [33, 34]. Nanometer size particulate fillers, e.g., carbon black (CB), silica (Si) nano-particles, etc., form hybrids with organic polymers. They show a significant increase in both static and dynamic moduli [35], strength [36], thermal and electrical conductivity [37, 38]. It is therefore important to understand the structure-property relationship in order to achieve better properties in the nanocomposites. TEMT offers detailed 3D characterization of the nanocomposites through various new structural parameters, some of which would never be obtained from other experimental techniques [28, 29, 39].

Among various types of nanocomposites, as a representative example, 3D direct observation and characterization of a nanocomposite with two kinds of particulate fillers in a rubbery matrix [29] will be presented here. One typical example is a composite of CB and Si nano-particles in a rubbery matrix. Hereafter, we call the nanocomposite CB&Si/NRBR [the matrix is a blend of natural rubber (NR) and polybutadiene (BR)]. In this composite, the CB increases the strength of the elastomer [40, 41] and thus acts as a reinforcing filler, while the Si nano-particles may add tear strength, abrasion resistance and a reduction in the heat built-up. In order to improve and maximize such functionalities, it is first necessary to *independently* visualize the two kinds of fillers in the matrix and to determine their 3D spatial distributions.

Until recently, the filled polymers have been observed by TEM and other experimental techniques, e.g., scattering methods [42]. There are, however, several experimental difficulties for an accurate structural analysis: (i) It is often difficult to distinguish the CB from the Si nano-particles under TEM in spite of their relatively large electron-density difference. Even though the fillers are discernible in principle by TEM, because there is an overlap of the fillers in the depth direction of the specimen (Z direction), in reality, it is difficult to distinguish one filler from the other. (ii) TEM provides only a 2D projection of a 3D structur-

al body. For the former problem, electron energy loss spectroscopy (EELS) [43, 10, 44], which enables us to obtain an elemental-mapped image, would be useful. For the latter problem, TEMT [23, 8, 9] is a solution. Thus, the two techniques are combined. "TEMT-EELS" will provide elemental-mapped 3D image of materials. Detailed information about the nanocomposite and experimental protocols, especially about TEMT-EELS, can be found elsewhere [29].

Figures 9(a) and 9(b) show the digital slices of the TEMT and TEMT-EELS volume data at the same position of the CB&Si/NRBR specimen. A corresponding TEM micrograph is shown in Fig. 9(c). From the TEM micrograph [Fig. 9(c)], it is possible to judge the extent of the dispersion of the fillers in the rubbery matrix. However, because the fillers overlapped along the Z-direction and resolution along this direction is lost in the TEM, the identification of each filler was impossible. In contrast, the digital slice of the 3D reconstruction [Fig. 9(a)] had a higher contrast than the TEM and the detailed features, i.e., the spatial arrangements of the fillers, were clearly observable. What is intriguing is that there are two kinds of fillers appearing differently in Fig. 9(a): One appeared solid, while the other was rather transparent in the middle with their
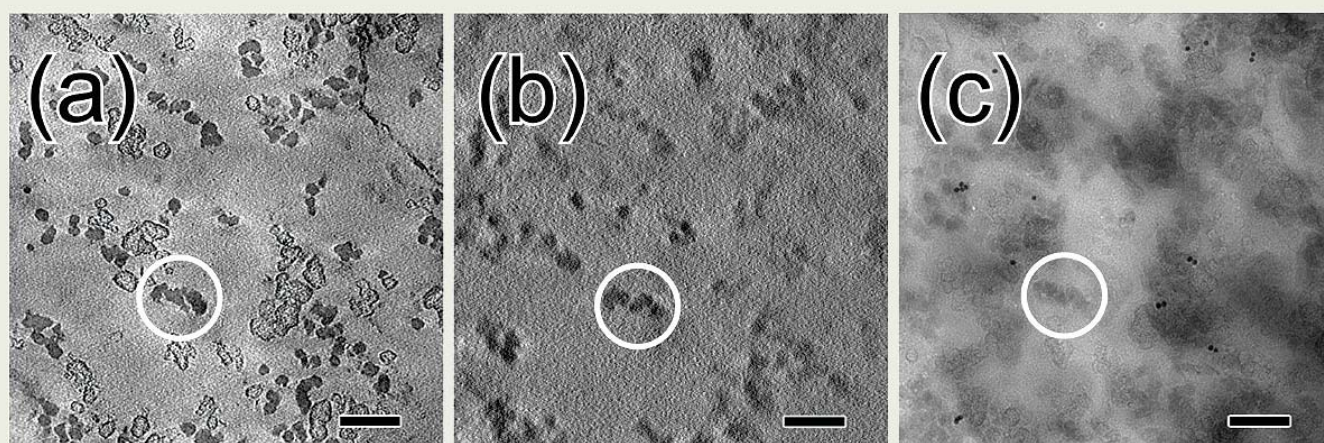

Fig.9 (a) A digital slice of TEMT, (b) A digital slice image of 3D reconstruction from TEMT-EELS, and (c) TEM micrograph in the same field of view of the CB&Si/NRBR system. White circles indicate the same aggregate, i.e., Si aggregate, in the three pictures. Bar shows 100 nm.
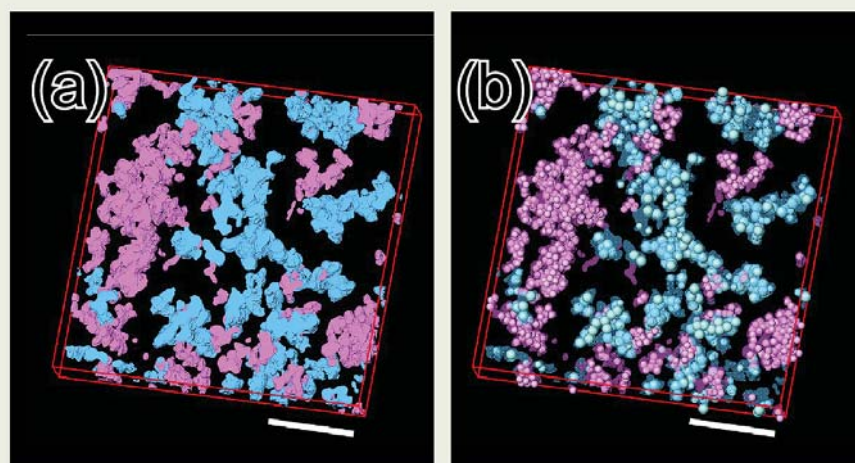

Fig.10 (a) 3D reconstruction of CB&Si/NRBR system. Blue and red regions consist of CB and Si nano-particles, respectively. (b) 3D reconstruction of CB&Si/NRBR system after the particle-packing analysis. The blue and red balls represent the CB and Si nano-particles whose diameters are 22 and 17 nm, respectively. The CB and Si regions are translucent in part (b). Bar shows 200 nm.

edges having a strong contrast, somewhat like hollow spheres. Assignment of these two kinds of particles either to the CB or to the silica particle is necessary in order to understand the 3D morphology of the CB&Si/NRBR system.

In the TEMT-EELS experiments, a 3D reconstruction was carried out from the series of energy-filtered Si mapped projections. Thus, the black particles in Fig. 9(b) correspond to the Si nano-particles. The image quality of the digital slice in the TEMT picture [Fig. 9(a)] is better than that in the TEMT-EELS [Fig. 9(b)] mainly due to the lower signal-to-noise ratio (S/N) of the Si-mapped projections and also due to the larger angular increment in the data acquisition of the TEMT-EELS experiment. Nevertheless, the position of the Si nano-particles was clearly seen.

Comparing Figs. 9(a) and 9(b), it was found that the aggregates of fillers marked by a circle in each part of Fig. 9 were silica aggregates. Close examination of the two digital slices provides the following important result: Among the two kinds of fillers observed in Fig. 9(a), the hollow and solid particles are, respectively, the CB and Si nano-particles.

Based on the results found in Fig. 9, the arrangement of these two kinds of fillers can be directly visualized in 3D [see **Fig. 10**(a)]. It was found that the aggregates consisted of only one species of the nano-particles. Namely, the CB and Si aggregates are made only of the CB and Si nano-particles, respectively. The size of each aggregate can be measured by separating the aggregates one from the other using the particle analysis algorithm [29, 45].

Although the 3D image shown in Fig. 10(a) exhibits by far richer structural information itself than the TEM micrograph [see Fig. 9(c)], it only shows the outer shape of each aggregate. An algorithm based on the Monte Carlo method called a "particle-packing" algorithm was proposed to virtually pack as many spherical particles as possible inside the aggregates [29]. Figure 10(b) shows the 3D images after applying the particle-packing analysis to the original TEMT-EELS image shown in part (a). The volume fractions of the CB and Si nanoparticles after the particle-packing analysis turned out to be slightly smaller than the volume fractions evaluated from the 3D reconstructions: The virtual CB and Si nano-particles did not fully occupy the corresponding regions, and hence the particle-packing algorithm is only semi-quantitative. Considering the fact that the CB and Si nano-particles are neither perfect spheres nor monodispersed, we regarded that the agreement of the volume fraction before and after the particle-packing analysis was reasonably good. Most importantly, the shape of the aggregates was well preserved even after the particle-packing analysis, and thus the analysis provides an intuitive understanding of the distribution of the primary nano-particles.

Such spatial position of each primary particle, i.e., individual CB and Si nano-particles, should be quite useful for correlating the internal morphology with various properties, e.g., the mechanical and electrical properties. For example, knowledge of the spatial arrangement of the nano-particles in the composite can be used to estimate the mechanical properties on the basis of FEA [31, 46], which would be a more accurate model than the conventional one in which the nano-particles have been *virtually* and *manually* arranged based on the insufficient 2D TEM images. Moreover, the persistent length of each aggregate, an important measure for understanding the electric conductivity of the nano-composite materials, will be evaluated by examining the connectivity of the primary nano-particles [47]. Such a study is in progress.

Besides the CB&Si/NRBR system, TEMT was also applied to a polymer/clay nanocomposite, an organophilic montmorillonite (MMT) dispersed in poly(ethylene-*co*-vinylacetate) (EVA). Unlike the nanocomposite described here, the clay minerals are plate-like nano-fillers. It is also well-known that the improvement in such properties strongly depends on their dispersion and orientation of the clay layers inside the polymer matrix [48, 49]. 3D morphology of a polymer/clay nanocomposite was studied by TEMT with particular emphasis on the shape and orientation of each clay layer [45].

A block copolymer thin film: Combination with reciprocal-space method

Background

As described in the first section, there are advantages and disadvantages in microscopy and scattering methods. In this section, we demonstrate a novel structural analysis that combines the real space (TEMT) and the reciprocal space (Neutron reflectivity, NR) methods in order to investigate a block copolymer thin film [50].

When the microphase-separated structures are confined in a thin film whose thickness is on the order of 10 to 100 nanometers, the surface interaction (between the block copolymer and substrate or between the block copolymer and air surface) as well as the confinement significantly affects the microphase-separated structures [51]. The block copolymer thin films have drawn considerable attention in many technological areas such as microelectronics [52-55] and nanoporous films [56, 57]. Guarini *et al*. reported that block copolymer thin films can be used as the mask layers for dense nanoscale dot patterning [52]. Applications of block copolymer thin film morphologies to the high surface area substrates for capacitors and biochips, quantum dot arrays for nonvolatile memories, silicon pillar arrays for vertical transistors or field-emission displays may be possible [52].

In order to understand the self-assembling morphologies of the block copolymer thin films, it is particularly important to study the self-assembling processes and the resulting morphologies. NR is one of the most useful methods for investigating microphase-separated structures of block copolymer thin films [58]. It provides a concentration (density) profile of one of the components with the very high precision of 0.5 *nm*. Some important pieces of structural information about block copolymer thin films, e.g., the location of junctions between dissimilar sequences, chain ends inside the microdomains and the interfacial thickness, have been investigated using NR [59-62].

Although powerful, NR first requires a hypothesized concentration profile for data analysis. The concentration profile assumed along the Z direction, i.e., the direction normal to the substrate, is used to fit the experimentally-obtained NR profile [63]. This "fitting" protocol of the concentration profile to the NR profile *heavily* depends on the initial concentration profile [64]. Therefore, until recently, NR has been more or less limited to rather simple morphologies that can be easily hypothesized, e.g., a lamellar morphology parallel to the substrate [59-62].

Although some applications seek to take advantage of the cylindrical microdomains in the block copolymer thin film, there are only a few studies dealing with cylinders [65, 66] and, to the best of our knowledge, no studies dealing with other types of microphase-separated structures in the block copolymer thin films due to some difficulties in assuming the appropriate initial concentration profiles for these morphologies. Therefore, it is critical to establish a methodology to estimate the initial concentration profiles. In the section below, we demonstrate that the combination of TEMT and NR would be capable of characterizing block copolymer thin films regardless of the type of morphologies.

Neutron Reflectivity measurements

A poly(deuterated styrene-*block*-2-vinylpyridine) (dPS-*b*-P2VP) block copolymer that forms a cylindrical morphology in the bulk state was used [50]. We observed the specular reflection using white neutrons. The measured NR profile from the dPS-*b*-P2VP, R_{exp}, is shown by the open circles in **Fig. 11** where the reflectivity, R, is plotted versus the magnitude of the scattering vector along the Z-direction, q_z. A rather featureless NR profile was obtained from the thin film, indicating that the microphase-separated structure inside the thin film was not very ordered.

The microphase-separated structure with hexagonally-packed cylindrical microdomains in the thin film [as illustrated in Fig. 11(b)] may be the first choice to start analyzing the NR profile. The cylinders are assumed to be aligned parallel to the substrate according to the results from previous studies [14, 65, 67]. The hypothetical model is based on the structural parameters determined in the bulk state and from the film thickness separately measured by AFM. The scattering length density profile along the direction perpendicular to the film surface was calculated from the model, b/v_{model}, which is shown by the dashed line in Fig. 11(c). Because the b/v is smaller for P2VP than for dPS, the peak-top and peak-bottom in the b/v correspond to the dPS and P2VP phases, respectively (b and v are the scattering length and the molar volume, respectively). There are five bottoms in Fig. 11(c), each of which correspond to the layer of the P2VP cylinders. It is obvious that the R_{model} did not reproduce the NR profile over the entire range of q_z.

The algorithm proposed by Parratt based on a recursive calculation method [63, 64] was employed to fit the R_{model} to R_{exp}. The resulting best-fit profile and the corresponding b/v are shown by the solid line in Figs. 11(a) and 11(c), respectively. Although the NR profile after the fitting approached R_{exp}, there was still a considerable deviation especially for the large q_z. This result again indicates that the

Fig.12 Volume rendered 3D images of the dPS-*b*-P2VP thin film from two different viewpoints, in which the dPS microdomain was made transparent. The box size of each 3D image is 720 × 90 × 344 *nm*. Arrows on the right of the 3D image indicate the P2VP layers. The 3D image was cropped along the *Y*- direction for viewing clarity (the total thickness in the *Y*- direction was 200 *nm*). Bar shows 200 *nm*.
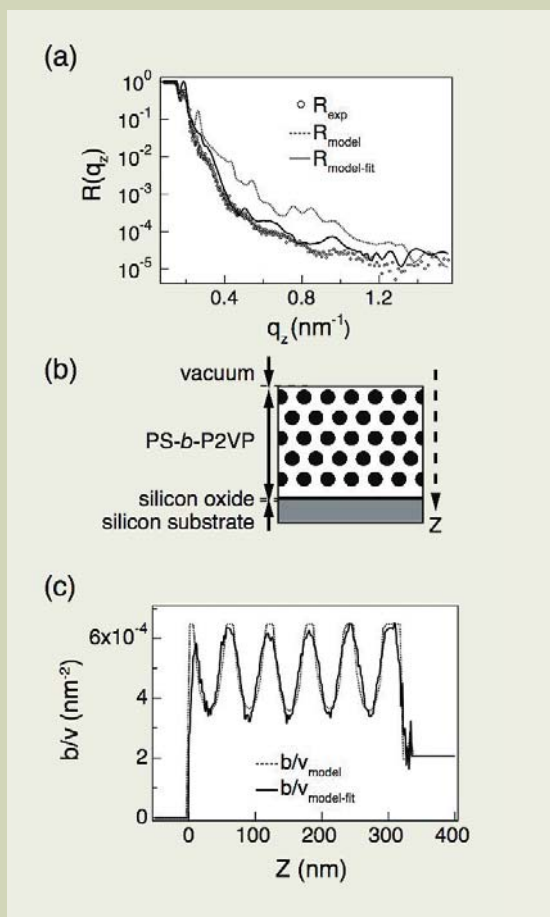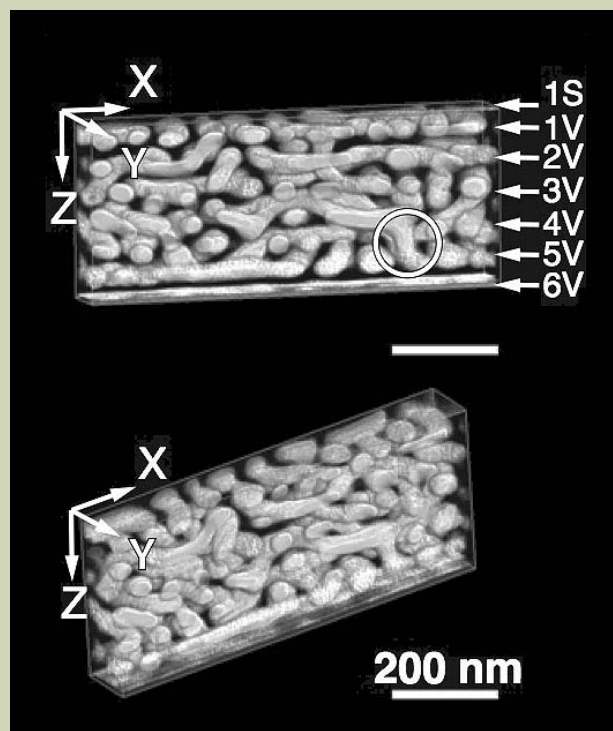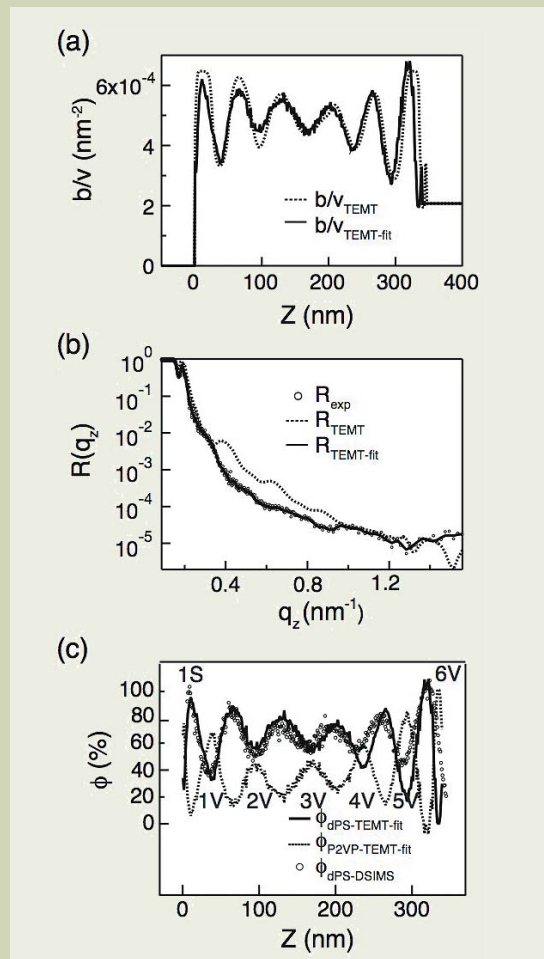
Fig.11 (a) NR profile of the dPS-*b*-P2VP thin film (open circles). The dashed line is the calculated reflectivity profile based on the hypothetical model in which the hexagonally packed cylinders are aligned parallel to the substrate. The corresponding *b/v* is shown by the dashed line in part (c). The dashed line was used as an "initial guess" in the fitting protocol [63, 64]. The solid line represents the best-fit NR profile after the fitting [the corresponding *b/v* is the solid line in part (c)]. (b) A cross sectional view of the hypothesized initial model of the dPS-*b*-P2VP thin film cast on a Si substrate. Dark circles and white domain are the edge-on view of the P2VP cylinder and the dPS matrix, respectively. The Z-direction in normal to the film surface. (c) Scattering length density profile, *b/v*, of the dPS-*b*-P2VP. The dashed line is the calculated profile from the hypothesized model shown in part (b). The solid line is the calculated *b/v* profile from the best-fitted reflectivity profile.

Fig.13 (a) Scattering length density profile (*b/v*) of the dPS-b-P2VP. The dashed line is the calculated *b/v* profile from the 3D image obtained by TEMT. The solid line shown in part (b) is the calculated *b/v* profile from the best-fit reflectivity profile. (b) Reflectivity profile of the dPS-*b*-P2VP thin film. Open circles are the measured NR profile. The dashed line and the solid line represent the calculated reflectivity profile from the initial model obtained by TEMT and the best-fit reflectivity profile, respectively. (c) The concentration profiles of the dPS-*b*-P2VP thin film, ø. The solid and dashed lines correspond to the concentration of dPS and P2VP, respectively. Letters on the peaks ofø are used to specify the layers of dPS or P2VP where S and V denote dPS and P2VP, respectively. Open circles are the measured concentration profile of dPS by DSIMS.

microphase-separated morphology was not a simple one as hypothesized. Because the NR profile did not show distinctive peaks, it is intrinsically difficult to have a precise and unique best-fit profile unless we have a realistic model for b/v as the initial guess. Therefore, we employed TEMT to directly visualize the 3D morphology of the dPS-b-P2VP thin film, which will be used as the initial hypothesized model as shown in the following section.

A new method: Combination of NR and TEMT

A cross sectional section (specimen) for the TEMT experiment was prepared by the FIB method from exactly the same spun-cast sample used in the NR experiments. The reconstructed 3D images of the dPS-b-P2VP thin film are displayed in **Fig. 12** from two different viewpoints, in which only the P2VP phase is shown (the dPS phase is transparent). In Fig. 12, the Z-direction corresponds to the depth direction of the dPS-b-P2VP thin film. The details of the 3D morphology of the dPS-b-P2VP thin film are visible in the figure. Although the majority of the cylindrical microdomains were oriented parallel to the substrate and formed six layers as indicated by arrows in Fig. 12, they did not form hexagonally-packed cylinders as hypothesized in Fig. 11(b). In addition, the cylindrical microdomains aligning normal to the film surface that connected the adjacent layers are also displayed by the white circle in Figure 12. It seemed that the cylindrical microdomains were interconnected through such vertical cylinders.

The scattering length density profile obtained from the TEMT image shown in Fig. 12, b/v_{TEMT}, is shown by the dashed line in **Fig. 13**(a). The NR profile based on this b/v_{TEMT} was obtained from the TEMT experiments, R_{TEMT}, and shown in Fig. 13(b). Comparing the previous results in Figs. 11(a) and 11(b), i.e., R_{model} and b/v_{TEMT}, (i) R_{TEMT} exhibited a more accurate NR profile than the R_{model} did, and (ii) b/v_{TEMT} had six peaks (as b/v_{model} did), but their heights were distinctively different from those in the b/v_{model}, especially in the middle of the thin film (100 $nm \leq Z \leq 250$ nm). R_{TEMT} reproduced R_{exp} very well at a low q_z ($q_z < 0.4$ nm^{-1}), but not in the high q_z region, indicating that the b/v_{TEMT} (and thus TEMT) captures the global feature of the dPS-b-P2VP thin film morphology, but the structural details were lost. In other words, TEMT already provides a statistically-averaged structural information by itself but has inferior spatial resolution compared to NR.

The b/v_{TEMT} was subsequently used as the initial guess for the fitting. The resulting scattering density profile, $b/v_{TEMT-fit}$, and the corresponding reflectivity profile, $R_{TEMT-fit}$, after the fitting [63] are denoted by the solid lines in Figures 13(a) and 13(b), respectively. The $R_{TEMT-fit}$ showed perfect agreement with the R_{exp}, much better than the R_{model} did.

The volume fraction of the dPS and P2VP blocks normal to the substrate ($\phi_{dps-TEMT-fit}$ and $\phi_{P2vp-TEMT-fit}$) were calculated from the scattering density profile obtain from the fitting, $b/v_{TEMT-fit}$, in Fig. 13, which are shown, respectively, by the solid and dashed lines in Fig. 13(c). Alternatively, the concentration profile of dPS was estimated *independently* from the TEMT and NR using Dynamic sec-ondary ion mass spectroscopy (DSIMS), $\phi_{dPS-DSIMS}$ [see the open circles in Fig. 13(c)]. $\phi_{dPS-DSIMS}$ showed excellent agreement with $\phi_{dPS-TEMT-fit}$, clearly demonstrating that the new methodology combining TEMT and NR provides not only a high-resolution (through NR), but also an intuitive (through TEMT) way of characterizing the block copolymer morphologies. Detailed morphological discussion using the TEMT and NR data can be found elsewhere [50].

The novel methodology proposed in this section can be extended to the structural studies of the block copolymer thin film with more complicated and disordered morphologies. In addition, the methodology may also be extended to the off-specular scattering data [64, 68-71] as well as specular scattering data, i.e., the reflectivity because the 3D volume data obtainable from TEMT provide not only the depth but also in-plane structural information.

Concluding Remarks

This featured article summarizes recent advances in TEMT and its applications to polymer-related materials. With the dual-axis tomography and ultimately with full-rotation of the rod-shaped specimen ($\pm 90°$ tilt), it is now possible to obtain quantitative 3D data in sub-nanometer resolution. Although not shown, 3D imaging under stretching of a rubber-composite (Si nano-particles in a rubbery matrix) has been successfully carried out [72]. It would be ideal if one could observe structural changes upon external stimuli, e.g., stretching, in 3D at the same volume of the specimen. In fact, although only 2D,"in-situ" observations under special conditions, e.g., under high pressure and high temperature, upon applying force, etc., are coming into fashion in the electron microscopy society. A special TEM holder that has AFM capability for simultaneous force measurement and imaging is now available. It can be easily imagined that all those TEM techniques will eventually go to 3D, which should be extremely beneficial to morphological research.

Image contrast and electron beam damage on soft materials are always problems. Staining with inorganic metals, e.g., OsO_4 and RuO_4, has often been used for the former problem and cryogenic TEM may be the solution for the latter. Phase-contrast TEM is proven to be quite useful to enhance the image contrast [73], which could be a new solution for the contrast-enhancement. These TEM techniques are used together with CT in the biology field and will also be effective in research.

In some cases, structural elements of the order of sub-micrometer are responsible for materials properties. Moreover, most of the polymer morphologies are hierarchical. However, the maximum thickness of the specimen observable under 200 kV TEMT is normally limited to ca. 300 nm, which is too thin for the sub-micrometer structures. On the other hand, LSCM and X-ray CT do not provide such high resolution (their resolution is slightly less than 1 μm, at most). 3D imaging in sub-micrometer scale is currently the "missing zone." It is therefore necessary to develop new instruments that are capable of filling this resolution gap (the existing TEM with very high voltage of 1 MV or more is an ideal instrument for thick samples but accessibility to such an instrument is not always easy). The scanning electron microscopy combined with a focused ion beam (FIB-SEM) [74, 75], high-resolution X-ray tomography system with focusing optics and scanning transmission electron microscopy (STEM) may be the candidates for this purpose. STEM with better optics, optimized not for the ultra-high resolution but for the thick samples, is eagerly anticipated. The fourth dimension, time, should be added to the 3D microscopy in the future.

From the 3D volume data obtainable by TEMT (and other 3D microscopy), some basic structural parameters, e.g., volume fraction of one of the constituents and interfacial volume per unit volume, can be directly and relatively easily measured. These structural parameters are basic, but they are so far inferred from the 2D images and thus are possibly inaccurate. Characteristic length, being readily measured by use of scattering techniques, is also estimated by taking a Fourier Transform of the 3D images. Crystallographic analysis from the 3D images can be done with at least similar precision to the scattering, sometimes better than the scattering when a single grain can be obtained (Note that multiple grains in laser, X-ray and/or neutron beam smear the scattering pattern and accordingly ruin the spot-like pattern).

Moreover, the 3D digital data contains rich structural information that can be extracted with the aid of "cutting-edge" quantitative image analysis. It is possible to go farther to evaluate a new set of parameters. Interfacial curvatures are such examples. Connectivity of network domains of the morphologies is likewise important [30,76]. We emphasize that those geometrical and topological parameters have never been evaluated by any other (conventional) experimental techniques besides 3D microscopy. Thus, 3D microscopy together with the 3D digital analysis have great potential for analyzing structures, and we hope that the methodology will unveil hidden physics in materials science and open up new research areas in the future.

Acknowledgment

References

[1] Gunton JD, Miguel MS and Sahni PS, In: Domb C, Lebowitz JL editors., Phase

Transition and Critical Phenomena, vol. 8, Academic Press, New York, 1983, p. 269.

[2] Hashimoto T, Structure of polymer blends, In: Cahn RW, Haasen P, Kramer EJ editors., Structure and Properties of Polymers, **vol. 12** of *Materials Science and Technology,* VCH, Weinheim, 1993, p. 251.

[3] Bates FS and Fredrickson GH. *Phys. Today* 1999; 52: 32.

[4] Jinnai H, Nishikawa Y, Koga T and Hashimoto T. *Macromolecules* 1995; **28**: 4782-4784.

[5] Jinnai H, Koga T, Nishikawa Y, Hashimoto T and Hyde ST. *Phys. Rev. Lett.* 1997; **78**: 2248-2251.

[6] Jinnai H, Nishikawa Y, Morimoto H, Koga T and Hashimoto T. *Langmuir* 2000; 16: 4380-4393.

[7] Spontak RJ, Williams MC and Agard DA. *Polymer* 1988; **29**: 387-395.

[8] Jinnai H, Nishikawa Y, Ikehara T and Nishi T. *Adv. Polym. Sci.* 2004; **170**: 115-167.

[9] Jinnai H and Spontak RJ. *Polymer* 2008, submitted.

[10] Midglay PA and Weyland M. *Ultramicroscopy* 2003; **96**: 413-431.

[11] Koster AJ, Ziese U, Verkleij AJ, Janssen AH and Jong KPd. *J. Phys. Chem.* B 2003; **104**: 9368-9370.

[12] Kaneko K, Inoke K, Freitag B, Hungria AB, Midgley PA, Hansen TW, Zhang J, Ohara S and Adschiri T. *Nano Letters* 2007; **7**: 421-425.

[13] Baumeister W, Grimm R and Walz J. *Trends Cell Biol.* 1999; **9**: 81.

[14] Sugimori H, Nishi T and Jinnai H. *Macromolecules* 2005; **38**: 10226-10233.

[15] Crowther RA, DeRosier DJ and Klug A. *Proc. R. Soc. London* 1970; **A 317**: 319-340.

[16] Gilbert PFC. *Proc. R. Soc. London* 1972; **B 182**: 89-102.

[17] Penkzek P, Marko M, Buttle K and Frank J. *Ultramicroscopy* 1995; **60**: 393-410.

[18] Mastronarde DN. *J. Struct. Biol.* 1997; **120**: 343-352.

[19] Lorensen WE and Cline HE. *Computer Graphyics, SIGGRAPH `87* 1987; **21**: 163-169.

[20] Kawase N, Kato M, Nishioka H and Jinnai H. *Ultramicroscopy* 2007; **107**: 8-15.

[21] Niihara K, Kaneko T, Suzuki T, Sato Y, Nishioka H, Nishikawa Y, Nishi T and Jinnai H. *Macromolecules* 2005; **38**: 3048-3050.

[22] Kaneko T, Nishioka H, Nishi T and Jinnai H. *J. Electron Microsc.* 2005; **54**: 437-444.

[23] Frank J, Principles of electron tomography, In: Frank J editor., ELECTRON TOMOGRAPHY, Plenum Press, New York, 1992, pp. 1-16.

[24] Radzilowski LH, Carragher BO and Stupp SI. *Macromolecules* 1997; **30**: 2110-2119.

[25] Jinnai H, Nishikawa Y, Spontak RJ, Smith SD, Agard DA and Hashimoto T. *Phys. Rev. Lett.* 2000; **84**: 518-521.

[26] Yamauchi K, Takahashi K, Hasegawa H, Iatrou H, Hadjichristidis N, Kaneko T, Nishikawa Y, Jinnai H, Matsui T, Nishioka H, Shimizu M and Furukawa H. *Macromolecules* 2003; **36**: 6962-6966.

[27] Wilder EA, Braunfeld MB, Jinnai H, Hall CK, Agard DA and Spontak RJ. *J. Phys. Chem.* B 2003; **107**: 11633-11642.

[28] Nishioka H, Niihara K, Kaneko T, Yamanaka J, Inoue T, Nishi T and Jinnai H. *Compos. Interfaces* 2006; **13**: 589-603.

[29] Jinnai H, Shinbori Y, Kitaoka T, Akutagawa K, Mashita N and Nishi T. *Macromolecules* 2007; **40**: 6758-6764.

[30] Jinnai H, Kajihara T, Watashiba H, Nishikawa Y and Spontak RJ. *Phys. Rev. E* 2001; **64**: 010803(R)-010806(R), 069903(E).

[31] Akutagawa K, Yamaguchi K, Yamamoto A, Heguri H, Jinnai H and Shinbori Y. *Rubber Chem. Tech.* 2008, in press.

[32] Morita H, Kawakatsu T, Doi M, Nishi T and Jinnai H. *Macromolecules* 2008, in press.

[33] Kawasumi M, Hasegawa N, Kato M, Usuki A and Okada A. *Macromolecules* 1997; **30**: 6333-6338.

[34] Maiti P, Nam PH, Okamoto M, Hasegawa N and Usuki A. *Macromolecules* 2002; **35**: 2042-2049.

[35] Busfield JJC, Deeprasertkul C and Thomas AG. *Polymer* 2000; **41**: 9219-9225.

[36] Tsunoda K, Busfield JJC, Davies CKL and Thomas AG. *J. Mater. Sci.* 2000; **35**: 5187-5198.

[37] Yamaguchi K, Busfield JJC and Thomas AG. J. Polym. Sci. Part B: *Polym. Phys.* 2003; **41**: 2079-2167.

[38] Busfield JJC, Thomas AG and Yamaguchi K. J. Polym. Sci. Part B: *Polym. Phys.* 2003; **42**: 2161-2089.

[39] Drummy LF, Wang YC, Schoenmakers R, May K, Jackson M, Koerner H, Farmer BL, Mauryama B and Vais RA. *Macromolecules* 2008; **41**: 2135-2143.

[40] Guth E. *J. Appl. Phys.* 1945; 16: 20-25.

[41] Siegfried W and Degussa A. *Rubber Chem. Technol.* 1996; **69**: 325-346.

[42] Karasek L and Sumita M. *J. Mater. Sci.* 1996; **31**: 281-289.

[43] Egerton RF, Electron Energy-Loss Spectroscopy in the Electron Microscope, Plenum, New York, 1996.

[44] Gass MH, Koziol KKK, Windle AH and Midgley PA. *Nano Letters* 2006; **6**: 376-379.

[45] Nishioka H, Niihara K, Kaneko T, Yamanaka J, Inoue T, Nishi T and Jinnai H. *Compos. Interfac.* 2006; **13**: 589-603.

[46] Hon AA, Busfield JJC and Thomas AG, Constitutive models for rubber iii, Balkema, London, 2003, pp. 301-308.

[47] Tchoudakov R, Breuer O, Narkis M and Siegmann A. *Polymer Engineering and Science* 1996; **36**: 1336-1346.

[48] Lim YT and Park OO. *Macromol. Rapid. Commun.* 2001; **21**: 231-235.

[49] Ray SS, Okamoto K and Okamoto M. *Macromolecules* 2003; **36**: 2355-2367.

[50] Niihara K, Matsuwaki U, Torikai N, Atarashi H, Tanaka K and Jinnai H. *Macromolecules* 2007; **40**: 6940-6946.

[51] Fasolka MJ and Mayes AM. *Ann. Rev. Mater* 2001; **31**: 323-355.

[52] Guarini KW, Black CT, Zhang Y, Kim H, Sikorski EM and Babich IV. *J. Vac. Sci. Technol.* B 2002; **20**: 2788-2792.

[53] Hamley IW. *Nanotechnology* 2003; **14**: R39-R54.

[54] Park C, Yoon J and Thomas EL. *Polymer* 2003; **44**: 6725-6760.

[55] Stoykovich MP, Muller M, Kim S, Solak HH, Edwards EW, Pablo JJ and Nealey PF. *Science* 2005; **308**: 1442-1446.

[56] Widawski G, Rawiso M and François) B. *Nature* 1994; **369**: 387-389.

[57] Freer EM, Krupp LE, Hinsberg WD, Rice PM, Hedrick JL, Cha JN, Miller RD and Kim H. *Nano Lett.* 2005; **5**: 2014-2018.

[58] Russell TP. *Physica B* 1996; **221**: 267-283.

[59] Kenneth R and Russell TP. *Macromolecules* 1993; **26**: 1047-1052.

[60] Mayes AM and Russell TP. *Macromolecules* 1993; **26**: 3929-3936.

[61] Torikai N, Noda I, Karim A, Satija SK, Han CC, Matsushita Y and KawaKatsu T. *Macromolecules* 1997; **30**: 2907-2914.

[62] Noro A, Okuda M, Odamaki F, Kawaguchi D, Torikai N, Takano A and Matsushita Y. *Macromolecules* 2006; **39**: 7654-7661.

[63] Parratt LG. *Phys. Rev.* 1954; 95: 359-369.

[64] Russell TP. *Mater. Sci. Rep.* 1990; **5**: 171-271.

[65] Karim A, Guo L, Rafailovichi MH, Sokolov J, Peiffer DG, Schwarz SA, Colby RH and Dozier WD. *J. Chem. Phys.* 1994; **100**: 1620-1629.

[66] Ge S, Guo L, Colby RH and Dozier WD. *Langmuir* 1999; **15**: 2911-2915.

[67] Knoll A, Tsarkova L and Krausch G. *Nano Lett.* 2007; **7**: 843-846.

[68] Pasyuk VL, Lauter HJ, Gordeev GP, Buschbaum PM, Toperverg BP, Jernenkov M and Petry W. *Langmuir* 2003; **19**: 7783-7788.

[69] Lee B, Park I, Yoon J, Park S, Kim J, Kim K, Chang T and Ree M. *Macromolecules* 2005; **38**: 4311-4323.

[70] Wang J, Leiston-Belanger JM, Sievert JD and Russell TP. *Macromolecules* 2006; **39**: 8487-8491.

[71] Buschbaum PM, Maurer E, Bauer E and Cabitt R. *Langmuir* 2006; **22**: 9295-9303.

[72] Dohi H, Kimura H, Kotani M, Kaneko T, Kitaoka T, Nishi T and Jinnai H. *Polym. J.* 2007; **39**: 749-758.

[73] Tosaka M, Danev R and Nagayama K. *Macromolecules* 2005; **38**: 7884-7886.

[74] Wilson JR, Kobsiriphat W, Mendoza R, Chen HY, Hiller JM, Miller DJ, Thornton K, Voorhees PW, Adler SB and Barnett SA. *Nat. Mater.* 2006; **5**: 541-544.

[75] Kato M, Ito T, Aoyama Y, Sawa K, Kaneko T, Kawase N and Jinnai H. *J. Polymer Sci. B Polymer Phys* 2007; **45**: 677-683.

[76] Jinnai H, Watashiba H, Kajihara T and Takahashi M. *J. Chem. Phys.* 2003; **119**: 7554-7559.

ESR Study of the Fundamentals of Radical Polymerizations

Atsushi Kajiwara

Nara University of Education

ESR spectroscopic studies directed at clarifying the fundamentals of radical polymerizations have been conducted. Optimization of measurement conditions allows direct detection of radicals in polymerization reactions and well-resolved ESR spectra can be obtained. The spectra provide information not only on the structure, properties, and concentration of radicals but also information on the initiating and propagating (oligomeric and polymeric) radicals in radical polymerizations. A combination of ESR and atom transfer radical polymerization (ATRP) provided significant new information on the properties of radicals in radical polymerizations, e. g. dependency of chain length, dynamics, and reactivity (hydrogen transfer) of propagating radicals. Previously, it has been extremely difficult, even impossible, to obtain such information from ESR spectra during conventional radical polymerizations. To overcome this difficulty radical precursors of oligo- and poly(meth)acrylates were prepared by ATRP and purified. Model radicals, with given chain lengths were generated by reaction of the well defined radical precursors with an organotin compound and the radicals were observed by ESR spectroscopy. *tert*-Butyl methacrylate (*t*BMA) radicals with various chain lengths showed clear chain length dependent ESR spectra. Similar findings were also observed in cases of methyl methacrylate, *n*-butyl methacrylate, and benzyl methacrylate. These results will provide supporting information on the kinetics of radical polymerization. For acrylates, each ESR spectrum of dimeric, trimeric, tetrameric, and pentameric *tert*-butyl acrylate (*t*BA) model radicals observed at various temperatures provided clear experimental evidence of the 1,5-hydrogen shift.

Introduction

ESR is the most powerful tool for investigation of radical species in radical polymerizations. When well-resolved spectra can be observed, the spectra provide information not only on the structure, properties, and concentration of radicals but also information on the initiating and propagating (oligomeric and polymeric) radicals in radical polymerizations [1-16]. Direct detection of propagating radicals in radical polymerization by ESR spectroscopy has been very difficult, mainly due to a combination of the labile nature and the extremely low concentration of the propagating radicals.

Nevertheless well-resolved ESR spectra in the radical polymerizations of styrene and its derivatives, diene compounds, methacrylates, and vinyl esters were studied in benzene or toluene solution under normal polymerization conditions (**Fig. 1**) [5 - 7, 10, 12].

An example of an ESR spectrum of the propagating radicals of methyl methacrylate (MMA), observed during a polymerization reaction, is shown in **Figure 2**. It is well-resolved and shows the characteristic feature of hyperfine structures. Since values of hyperfine splitting constants were determined very precisely from the spectrum, it was able to be reasonably well simulated as the corresponding propagating radical, also shown in the Figure. Based on these spectra, kinetic analysis, especially for estimation of propagating rate constants (k_p) of the monomers, was performed. ESR spectroscopy was successfully applied to quantify radical concentration in the

Takabatake-cho, Nara 630-8528, Japan

E-mail: kajiwara@nara-edu.ac.jp

polymerizations. However, the direct detection method did not reveal many points that are very significant in radical polymerization chemistry. For example, the life of propagating chain is not known. In the estimation of k_p, chain length of the observed propagating radicals is considered to be long enough for estimation of k_p. However, there has been no clear experimental information on the actual chain length of the propagating radicals observed by ESR. The chain length was just hypothesized to be "long enough". In order to detect the well-resolved spectra, initiator concentration in some ESR experiments was higher than in usual radical polymerizations. Under such conditions, the chain length of the propagating radicals could be shorter than those formed under normal conditions. The chain length of the resulting polymers in the ESR samples can be estimated by measuring size exclusion chromatography (SEC) after ESR experiments. However, the resulting molecular weights, even if they were high enough, do not guarantee ESR detection of radicals with high molecular weights, because detection of shorter chain radicals is much easier than that of longer chain radicals. Therefore, the effect of the chain length of the propagating radicals in the polymerizations should be examined carefully. Moreover, it is extremely difficult to investigate copolymerization systems by the direct detection method. Copolymerization is a very important technique in radical polymerizations and it contains various kinds of propagating chain ends due to, so-called, penultimate unit effects. These problems have not yet been resolved but the development of controlled radical polymerization techniques, especially atom transfer radical polymerization (ATRP), enables us to solve some of these problems.

ATRP is one of the most widely applied polymerization techniques in the field of controlled/living radical polymerization. ATRP allows the preparation of a wide range of polymeric materials with controlled molecular weights and well-defined architectures [17-26]. The polymers formed in ATRP most frequently contain terminal carbon-halogen bonds. Giese *et al.* has reported that these bonds can be homolytically cleaved by reaction with organotin compounds [27]. Accordingly, various radicals that model the end groups in an ATRP can be formed from the corresponding precursors prepared by atom transfer radical addition (ATRA) and ATRP and the generated radicals can be studied by ESR spectroscopy. For example, polymeric (meth)acrylates with various chain lengths can be prepared as radical precursors by ATRP. Variation of the chain length of these polymeric radical precursors elucidates of the affect of chain length on the ESR spectra of the formed radicals.

The investigations of radical reactions are difficult without using model reactions. Poly(meth)acrylates with various chain lengths can be prepared by ATRP and propagating radicals, with various known chain lengths, can be generated from these model precursors. The ESR spectra of these model radicals at various temperatures are expected to show chain length dependence effects. ESR spectra of propagating radicals of methacrylates observed *in situ* show a clear temperature dependency due to the dynamics of chain ends [5]. This phenomenon can be applied to study chain length dependent spectroscopic variation using model radicals. This method can also be applied to investigate chain transfer reactions
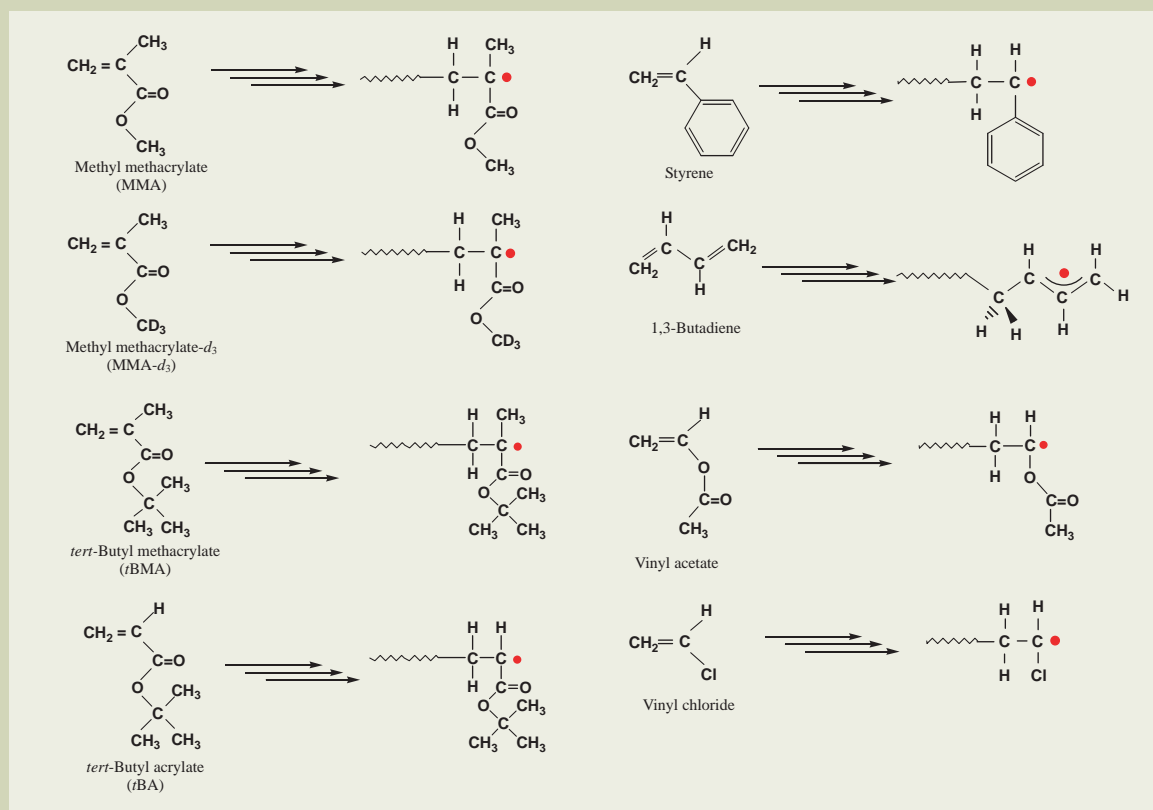
Fig.1 Structures of monomers and propagating radicals generated from corresponding monomers.
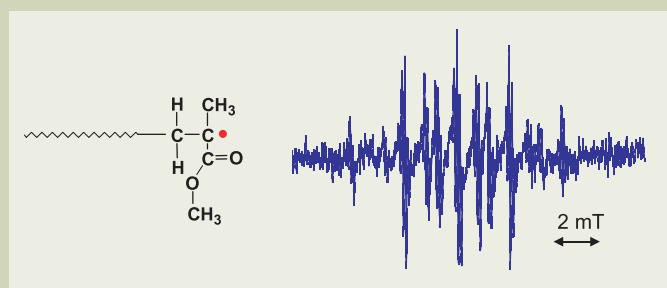

Fig.2 ESR spectrum of propagating radicals of methyl methacrylate (MMA) along with its proposed structure. The spectrum was observed during radical polymerization in a sample cell under irradiation of ultra high pressure mercury lamp. A 1:3:3:1 quartet splitting due to methyl protons of methyl ester was clearly observed (measurement condition; solvent: toluene 30 % (v/v), temperature: 60 °C, modulation: 100 kHz, 0.05 mT, time constant: 0.3 sec, sweep time: 15 mT/16 min).
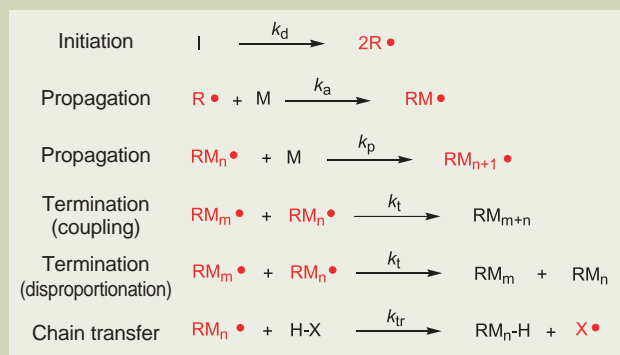

Fig.3 Elementary processes of radical polymerization. "I" is an initiator, "R" is a radical generated from the initiator, "M" is a monomer, "M_n" is a polymer with degree of polymerization of n, and "H-X" is a compound with a hydrogen that easy to abstract. "k" is a rate constant of each reaction." • " represents an unpaired electron of a radical.

for propagating acrylate radicals.

Direct ESR Detection of Propagating Radicals

Progresses of Techniques on the Detection of ESR Spectra of Radicals during Polymerizations

Many technical problems associated with direct measurement of ESR signals from propagating radicals have been overcome. Direct detection of propagating radicals in radical polymerization by ESR spectroscopy had been very difficult, mainly due to both the labile nature and the extremely low concentration of the propagating radicals. This problem was partly solved by the development of the TM_{110}-mode cavity by Kamachi with a help of the JEOL research group. About 20 years ago, Kamachi *et al*. observed the ESR spectra of

propagating methacrylate radicals under conditions similar to those in conventional polymerization by means of a specially designed flat cell and cavity called TM_{110}-mode cavity [5]. The TM_{110}-mode cavity has the same shape as a TE_{011}-mode universal cavity turned sideways. The magnetic field of the irradiating microwave is normal to a horizontal plane, including the cavity axis, and the magnetic flux density in the TM_{110}-mode cavity is lower than that with a TE_{011}-mode cavity, if one uses a conventionally available cylindrical sample tube. Because a larger area is available for the ESR measurements under UV-light irradiation with the TM_{110}-mode cavity, the wider lat cell is useful. ESR spectra were observed at an initiator concentration 1 or 2 orders of magnitude higher than the concentration usual radical polymerization using the TM_{110}-mode cavity. Two important results bearing on the fundamentals of radical polymerizations were

obtained through the development of the TM_{110}-mode cavity. One was the observation of propagating radicals in real radical polymerization systems. The other was clear evidence for the presence of steady state radical concentrations during radical polymerizations. From the beginning of the 1990's, relatively well resolved ESR spectra of propagating radicals have been observed using a commercially available TE_{011}-mode universal cavity and normal sample cell, due to both improvement in ESR spectrometers and careful optimization of the preparation of the sample [5, 10-12].

Difficulty in direct detection of ESR spectra of propagating radicals is also due to a complexity of the radical polymerization reactions. It is well known that a radical polymerization reaction involves several elementary processes. Typical elementary processes are shown in **Figure 3**. In the figure species which have an unpaired electron (•) are paramagnetic and
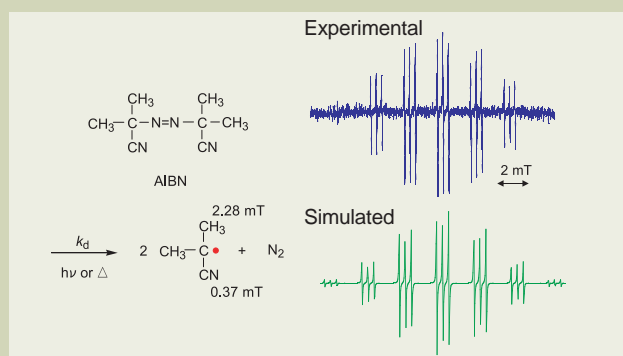
Fig.4 ESR spectrum of radicals generated from UV-irradiation of AIBN along with its simulated spectrum. The spectrum clearly showed equivalent three lines due to nitrogen nuclei. A reaction scheme of generation of the radical and its hyperfine splitting constants are shown at the left hand side of this figure (measurement condition; solvent: toluene, temperature: 0 °C, modulation: 100 kHz, 0.05 mT, time constant: 0.03 sec, sweep time: 15 mT/8 min).

Fig.6 ESR spectrum of propagating radicals of *tert*-butyl methacrylate (*t*BMA) initiated by *tert*-butyl peroxide under irradiation at various temperatures along with a scheme of radical formation.
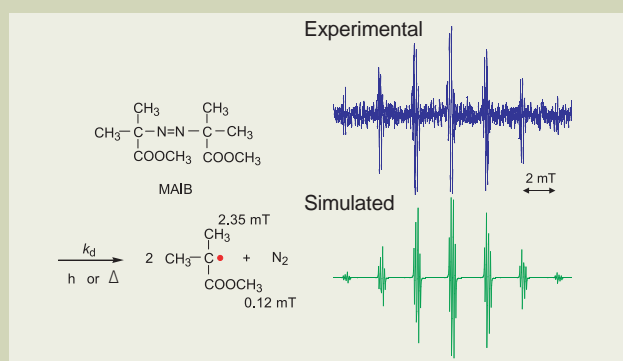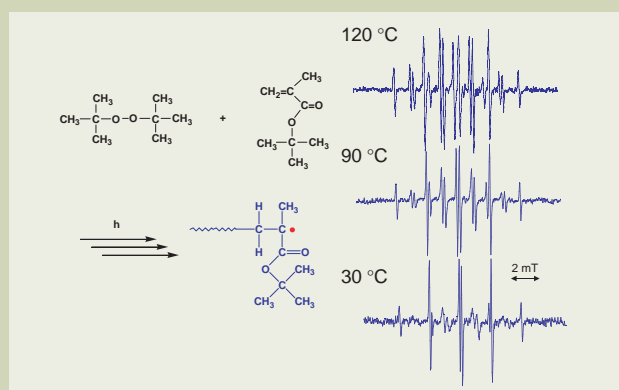

Fig.5 ESR spectrum of radicals generated from UV-irradiation of MAIB along with its simulated spectrum. The spectrum clearly showed 1:3:3:1 quartet lines due to methyl protons at methyl ester. A reaction scheme of generation of the radical and its hyperfine splitting constants are shown at the left hand side of this figure (measurement condition; solvent: toluene, temperature: 0 °C, modulation: 100 kHz, 0.025 mT, time constant: 0.1 sec, sweep time: 15 mT/16 min).
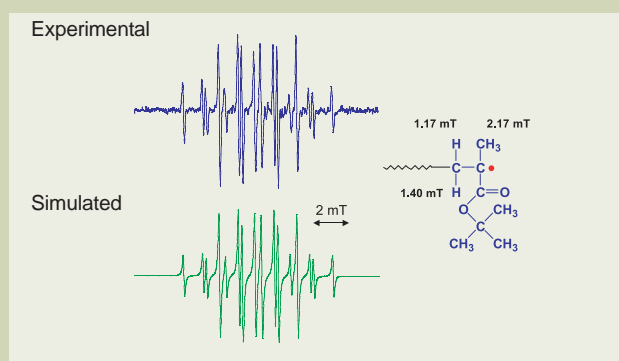

Fig.7 Experimental and simulated ESR spectra of the propagating radical in polymerization of *t*BMA at 150 °C (measurement condition; solvent: mesitylene 30 % (v/v), temperature: 150 °C, modulation: 100 kHz, 0.1 mT, time constant: 0.3 sec, sweep time: 15 mT/16 min).

ESR observable, which means that various kinds of radical species coexist in the polymerization system. In principle, each species can be observed separately as model radicals with the aid of controlled radical polymerization methods as described in the latter part of this paper. However, direct detection of each of the radical species in Figure 3 one by one is very difficult or almost impossible. Especially, the conditions for detection of the propagating radicals during polymerization reactions and measurement of the ESR spectra should be optimized very carefully.

Radicals generated from azo-initiators.

The initiation process is a two steps reaction: the 1st step is decomposition of an initiator to form radicals and the 2nd step is an addition of the radical to a first monomer to form primary propagating radical as shown in Figure 3. The 1st step reaction can be observed by ESR in a separate procedure. The case of 2,2'-Azobis(2-methylpropionitrile) (AIBN) will be shown as an example. AIBN was decomposed by heating (to 60-80 °C) or upon irradiation to generate two copies of the same radical by cleavage of C-N bond and generating N2 gas. This radial can be observed by ESR. The ESR spectrum

of the radical is shown in **Figure 4** along with its simulated spectrum. The primary feature of the spectrum is a relatively large heptet with small equivalent three line splitting due to presence of the nitrogen nuclei (I = 2/2). The values of coupling constants shown in the Figure 4 are reasonable for the structure and the simulated spectrum has features very close to the experimental spectrum.

Similarly, the ESR spectrum of initiating radicals generated from dimethyl 2,2'-azobis(2-methylpropionate) (MAIB) were able to be observed as shown in **Figure 5**. The spectrum displayed a relatively large heptet with small 1:3:3:1 four line splitting due to the methyl protons. Primary propagating radicals (RM•) will be formed by an addition of the radicals to a first monomer.

When an excess amount of monomer is added to the initiator solution, radical polymerization will proceed upon heating or irradiation in a sample cell. The propagating radicals formed in the solution can be observed by ESR.

Direct Detection of Propagating Radical during Radical Polymerization by ESR

Well-resolved ESR spectra of the radicals

present in the polymerization of styrene and its derivatives, diene compounds, methacrylates, vinyl esters, and vinyl chloride were studied in benzene or toluene solution under usual polymerization conditions [5-7, 10-16]. Selected examples of ESR spectra of these propagating radicals observed during polymerization reactions are shown in **Figure 6-13**. They are well-resolved and show the characteristic features of hyperfine structures. Since values of hyperfine splitting constants were determined very precisely from these spectra, all of these spectra were reasonably well simulated as the corresponding propagating radicals, also shown in the Figure.

***tert*-Butyl Methacrylate (*t*BMA)**

When a mixture of monomer and a radical initiator was heated or photo-irradiated in an ESR sample cell, propagating radicals were formed and the polymerization proceeded. Well-resolved spectra of the propagating radicals of *tert*-butyl methacrylate (*t*BMA) have been detected in such polymerization systems at various temperatures as shown in **Figure 6**. 16-line spectra were clearly observed. They were different from the ESR spectra previously reported for methacrylates (13-line or 9-line
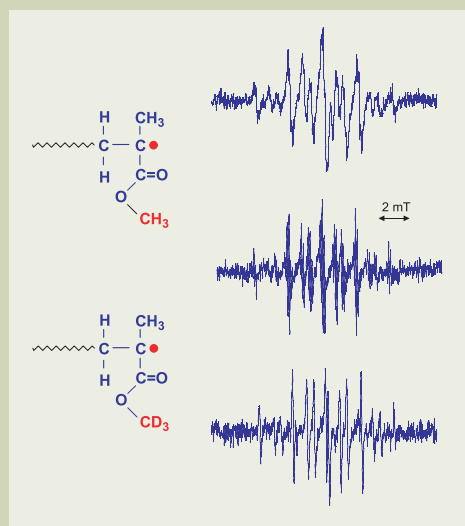
Fig.8 ESR spectra of the propagating radicals in polymerization of MMA. a) ESR spectrum of the propagating radical of MMA (low resolution) (measurement condition; solvent: toluene, temperature: 60 °C, 20 % (v/v), modulation: 100 kHz, 0.2 mT, time constant: 0.1 sec, sweep time: 15 mT/16 min), b) ESR spectrum of the propagating radical of MMA (high resolution) (measurement condition; solvent: toluene, temperature: 60 °C, 20 % (v/v), modulation: 100 kHz, 0.05 mT, time constant: 0.3 sec, sweep time: 15 mT/16 min), c) ESR spectrum of the propagating radical of MMA-d_3 (low resolution) (measurement condition; solvent: toluene 20 % (v/v), temperature: 60 °C, modulation: 100 kHz, 0.1 mT, time constant: 0.1 sec, sweep time: 15 mT/8 min).

Both of low and high resolution spectra recorded under the similar polymerization conditions are shown. (low resolution: measurement condition; solvent: benzene 30 % (v/v), temperature: 25 °C, modulation: 100 kHz, 0.2 mT, time constant: 0.1 sec, sweep time: 10 mT/16 min) (high resolution: measurement condition; solvent: toluene 30 % (v/v), temperature: 0 °C, modulation: 100 kHz, 0.05 mT, time constant: 0.1 sec, sweep time: 10 mT/16 min).
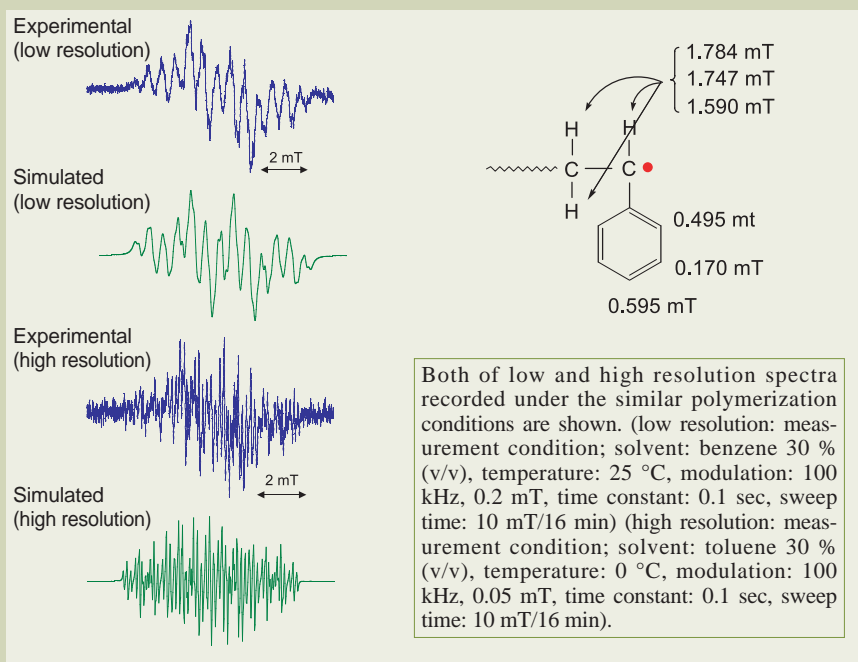
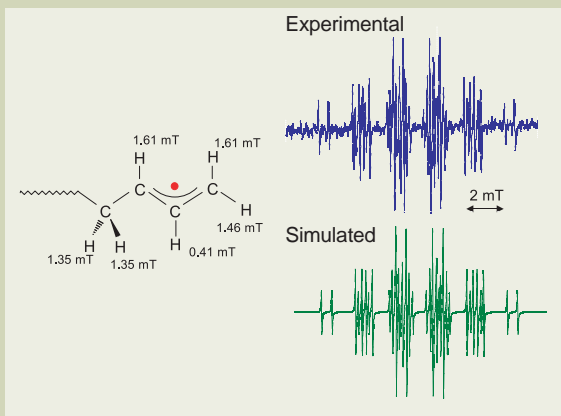Fig.9 ESR spectra of the propagating radicals in polymerization of styrene.

Fig.10 ESR spectrum of the propagating radical of 1,3-butadiene along with its simulated spectrum (measurement condition; solvent: benzene 30 % (v/v), temperature: -30 °C, modulation: 100 kHz, 0.025 mT, time constant: 0.1 sec, sweep time: 10 mT/16 min).

spectra) [5, 10, 28], but were rationally assigned to viable propagating radicals. Since long-range hyperfine structures due to the methyl protons of the *tert*-butyl group in the ester side chain did not appear in the spectra the splitting lines should be due to the three a-methyl protons and the two β-methylene protons. Thus the values of their hyperfine coupling constants were precisely determined. The spectroscopic features of the spectra showed clear temperature dependence which can be interpreted by a hindered rotation model of the two stable conformations [5]. The intensity of the inner 8 lines increased with increasing temperature, indicating that there are two exchangeable conformations whose existence have been shown in the elucidation of ESR spectra of methacrylates [5]. At 150 °C, the intensity of the inner 8 lines increased and the ESR spectrum can be interpreted as a single conformation, indicating that the energy difference between the two conformers is small. The observed ESR spectrum of propagating radicals of *t*BMA at 150 °C is shown in **Figure 7** along with the simulated spectrum. The spectrum is accurately simulated using hyperfine splitting constants of 1.40 mT for one methylene proton (1:1 doublet), 1.16 mT for the other one proton (1:1 doublet), and 2.17 mT for

three equivalent methyl protons (1:3:3:1 quartet) as shown in Figure 7.

Methyl Methacrylate (MMA) 13-line and 16-line Spectra

ESR spectra of the propagating radicals present in MMA radical polymerizations are shown in **Figure 8**. A 13-line ESR spectrum has been observed for the propagating radicals in MMA polymerization using TM_{110}-mode cavity. Figure 8a shows an ESR spectrum of the propagating radicals of MMA in radical polymerization at low resolution. This is the so-called 13-line spectrum that has been observed for MMA polymerization systems. The resolution of the spectrum can be improved by choosing smaller values of modulation width and the resulting highly resolved ESR spectrum of the MMA propagating radicals is shown in Figure 8b. This spectrum was recorded under almost the same conditions employed in Figure 8a. A small 1:3:3:1 quartet splitting due to methyl protons in methyl ester can be observed in the well resolved spectrum. The presence of small quartet splitting clearly indicates that the structure of the radical is the same as that we have estimated as shown in Figure 8. On the other hand, the interpretation of the spectrum turned out to be more compli-

cated by an overlapping of the spectroscopic lines and lowering the S/N ratio due to the presence of the small quartet splitting.

Therefore deuterated MMA (MMA-d_3) was used as a monomer in order to simplify the spectra by selective observation of only the α-methyl and β-methylene protons as in the case of *t*BMA. In MMA-d_3 three methyl protons of the methyl ester are replaced by deuterium and since splitting due to deuterium nuclei is 1/6 smaller than that of hydrogen nuclei it is coalesced in the line width. Therefore, only the splitting due to α-methyl and β-methylene protons were observed in the spectra. The spectrum obtained during the polymerization of MMA-d_3 is shown in Figure 8c. It is a 16-line spectrum that can be interpreted just like that of *t*BMA as discussed above.

Now, we can say that the 13-line and 16-line spectra are essentially the same spectrum. The detection of 16-line spectrum also indicates that the propagating MMA radical has a sufficiently long chain length for kinetics study, especially for estimation of k_p as discussed later.

Styrene

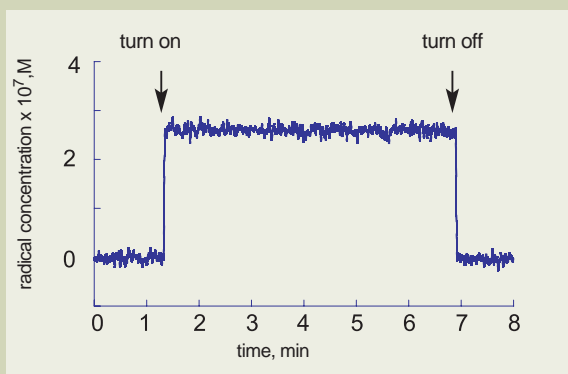ESR spectra of the propagating styrene radicals were clearly observed in a bulk polymer-

Fig.11 Time-dependence of the signal intensity of the ESR spectrum at constant field of 1,3-btadiene.
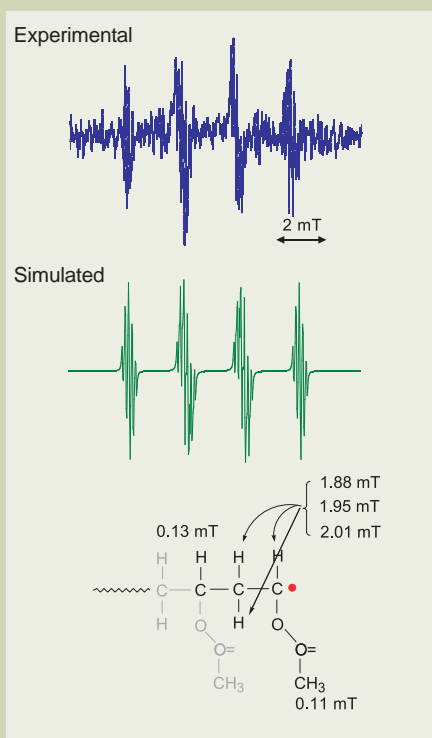

Fig.12 ESR spectrum of the propagating radical of vinyl acetate along with its simulated spectrum (measurement condition; solvent: benzene 30 % (v/v), temperature: 5 °C, modulation: 100 kHz, 0.05 mT, time constant: 0.3 sec, sweep time: 10 mT/16 min).

ization at various temperatures under irradiation. A typical example of the ESR signal of a propagating styrene radical in a conventional radical polymerization is shown in **Figure 9**. Simulation of the spectrum provides a close fit with the observed spectrum of the styrene propagating radical; both low and high resolution spectra are shown. These spectra were observed with different modulation width under almost the same conditions. The concentration of the propagating radicals can be precisely estimated by the low resolution spectrum because it has better S/N ratio. Hyperfine splitting constants can be measured precisely using the high resolution spectrum.

1,3-Butadiene

A well-resolved ESR spectrum was observed in the radical polymerizations of the 1,3-butadiene with *t*BPO, although a higher concentration of initiator than usually employed for a radical polymerization (5 mol% for monomer) was necessary to obtain a sufficiently resolved spectra to allow investigation of the behavior of the propagating radical(**Fig. 10**) [15]. Moreover, the steady state of the radical concentration in the polymerization was confirmed by the time dependency of the intensity of the ESR signal at constant magnetic field

during irradiation with light (**Fig. 11**) [15]. The steady state radical concentration had been an assumption in a kinetics study of radical polymerizations. Now, ESR provides experimental evidence for the steady state [5,10].

Vinyl Acetate

The ESR spectrum of propagating radicals observed during radical polymerization of vinyl acetate at 5 °C is shown in **Figure 12** along with its simulated spectrum. Resolution of the experimental spectrum is much improved from that observed using a TM$_{110}$-mode cavity. The spectrum shows splitting due to one α-proton and two β-methylene protons. Values of these couplings can be precisely measured from the spectrum, although one by one critical assignment is impossible only from these values. Each line split by α- and β-protons exhibits further splitting due to not only methyl protons but also γ-proton because more than five splitting lines can be observed.

Vinyl Chloride

Measurements of ESR spectra of propagating vinyl chloride radicals were performed by photo-initiated polymerizaitons with *t*BPO in benzene solution [29]. The spectrum is reasonably assigned to be a normal vinyl chloride

propagating radical with hyperfine coupling constants. As shown in **Figure 13**, clear equivalent quartet due to nuclear spin of the chlorine nuclei (I = 3/2; ^{35}Cl) was observed. In principle, coupling of isotope of chlorine (^{37}Cl) should be also considered. However, the spectrum was not sufficiently well-resolved to show the difference in the hyperfine splitting constants between the isotopes. The obtained signal was reasonably well simulated by using the above hyperfine coupling constants, as shown in Figure 13. The hyperfine coupling constant of 1.85 mT due to α-proton is similar to that of the propagating radical of vinyl acetate, suggesting that the radical reactivity of the propagating radical is similar to that of vinyl acetate. To our knowledge, this is the first example of a detection of an ESR signal of propagating vinyl chloride radicals in solution. Careful choice of the conditions is very important to generate the simple, clear, and well-resolved signal.

Results and Outlook

Owing to both continuous development of ESR spectrometers and optimization of measurement conditions, various kinds of spectra for propagating radicals, which were previously extremely difficult to observe, were recorded at high resolution. These spectra can provide significant information on the nature of propagating radicals because they are obtained from actual polymerization systems. From the spectra shown in this paper, detailed structural information can be obtained from the values of the hyperfine splitting constants. Experimental evidence also determined that there is a steady state of radical concentration in the polymerizations. In formation on the dynamics of the terminal radicals can be obtained form the spectra obtained at various temperatures as shown in the case of ESR spectra of methacrylate propagating radicals. Activation energies of the rotational motion of the terminal radicals can be estimated from the results allowing the structures, dynamics, and kinetics of the propagating radicals to be discussed based on these ESR spectra.

On the other hand, many problems remain unsolved. Two rep]resentative problems, and the experiments undertaken to solve the problems by ESR, with the aid of well defined radical precursors prepared by ATRP (**Figs. 14,15**) will be discussed in the following sections.

Combination of ESR and Controlled Radical Polymerization Methods

Generation of Model Radicals from Precursors Prepared by Controlled Radical Polymerization Methods

In the following two sections, two further examples of the application of ESR spectroscopy to conventional radical polymerizations based on information obtained from controlled/living radical polymerizations will be demonstrated. First is estimation of effect of chain length on propagating radials which is elucidated by ESR conducted with the aid of polymers prepared by ATRP. Second, is detection of chain transfer reactions on propagating radicals during the polymerization of *t*BA.

Indeed ESR is one of the most effective methods for estimating values for *kp* and it is a

Experimental
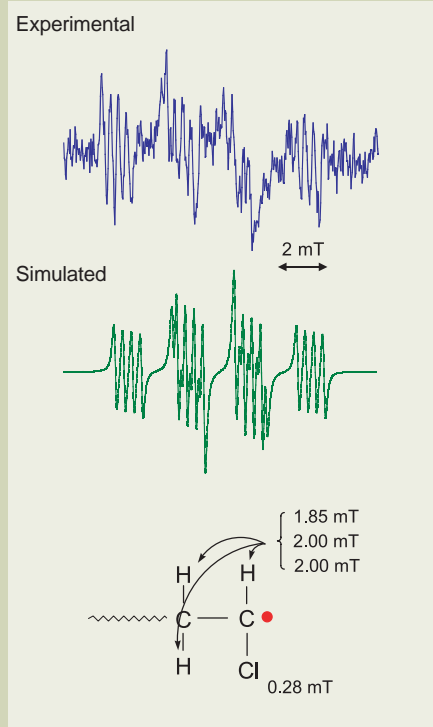
Simulated

2 mT

1.85 mT
2.00 mT
2.00 mT

0.28 mT

Fig.13 ESR spectrum of the propagating radical of vinyl chloride along with its simulated spectrum (measurement condition; solvent: benzene 30 % (v/v), temperature: 25 °C, modulation: 100 kHz, 0.1 mT, time constant: 0.1 sec, sweep time: 10 mT/8 min).
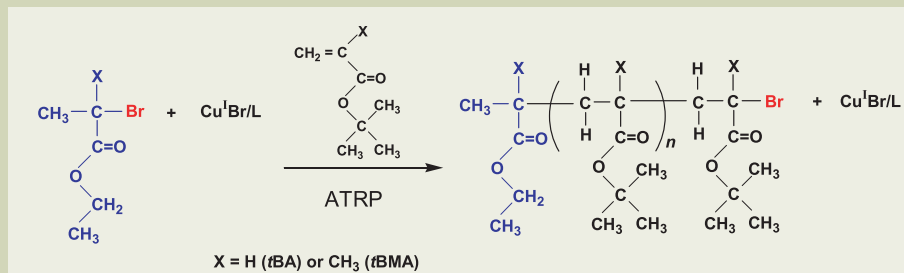

X = H (*t*BA) or CH₃ (*t*BMA)

Fig.14 Atom transfer radical polymerization (ATRP) of tert-butyl (meth)acrylate for preparation of model radical precursors.

Propagating radical

Model radical precursor prepared by ATRP

Model radical with predetermined structure

x=H(acrylate) or CH₃ (methacrylate)
R=methyl,ethyl,*tert*-butyl
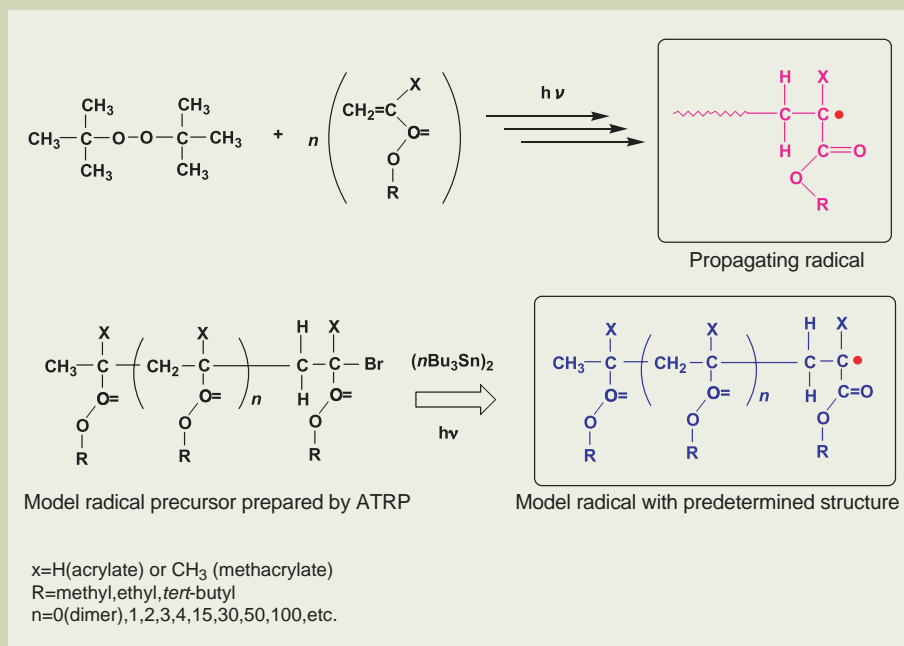n=0(dimer),1,2,3,4,15,30,50,100,etc.

Fig.15 Radicals observed by ESR. Formation of propagating radicals during a standard free radical polymerization (above) and generation of model radicals from radical precursors prepared by ATRP (below).

mutually complementary method to the Pulsed Laser Polymerization (PLP) method. Usually **equation (1)**, and its integrated form **(2)**, have been used to calculate k_p by ESR.

$$\mathrm{R_p} = -\frac{d[M]}{dt} = k_p[P_n{}^{\bullet}][M] \quad \cdots \cdot (1)$$

$$\ln \frac{[M_1]}{[M_2]} = k_p[P_n{}^{\bullet}] \quad \cdots \cdots \cdots (2)$$

The advantage of ESR is that the value of $[P_n{}^{\bullet}]$ in these equations can be determined from the observed ESR spectra of the propagating radicals. Detailed analysis of the spectra provides information, not only on radical concentration, but also on the structure and other physicochemical properties of the radicals. Furthermore, steady state radical concentrations can be confirmed from the spectra. On the other hand, the ESR method makes two important assumptions: one is that we observe the propagating radical with sufficiently long chain length and the other is that we observe real propagating radicals. Therefore ESR was employed to examine and quantify some intermediates in an ATRP which should provide a deeper understanding of the ATRP process,

including identification of the structure and concentration of the paramagnetic species involved in the polymerization [30-33]. Although it is very interesting, and important for investigation of ATRP, the structural features of the paramagnetic transition metal compounds will not be discussed in this paper.

Differentiation of the Chain Length of Propagating Methacrylate Radicals by ESR

The spectrum of a propagating methacrylate radical is completely simulated using hyperfine splitting constants of 1.40 mT for one methylene p]roton (1:1 doublet), 1.16 mT for the other one proton (1:1 doublet), and 2.17 mT for three equivalent methyl protons (1:3:3:1 quartet) as shown in Figure 3b. A characteristic point of this result is estimation of different hyperfine splitting constants for the two methylene protons. This means that the rate of rotation of the end radical is not fast enough to make the methylene protons equivalent on the time scale of the ESR measurement. Thus, it leads to a 16-line spectrum (2 × 2 × 4). If the two β-methylene protons were equivalent, the total number of splitting lines

would be 12 (4 (CH₃-) × 3 (-CH₂-)). The expected spectra for these two cases are simulated and are shown in Figure 4. This suggests the presence of a propagating radical with a long chain that hindered the rotation of the terminal bond to generate the 16-line spectrum and also another oligomeric radical which may show a 12-line spectrum(**Fig. 16**).

If we could observe the ESR spectra of radicals with controlled chain length, chain length dependent phenomena could be precisely examined. In order to clarify the phenomena, model radical precursors were prepared by the ATRP technique. ATRP can provide polymers with controlled molecular weights and low polydispersity, and the resulting polymers have preserved terminal carbon-halogen bonds [14-20]. When the carbon-halogen bonds are cleaved homolytically by reaction with organotin compounds, model radicals of propagating chains with given chain length can be generated (Fig. 15 below) [21].

Differentiating Between Chain Lengths of Propagating Radicals of *t*BMA
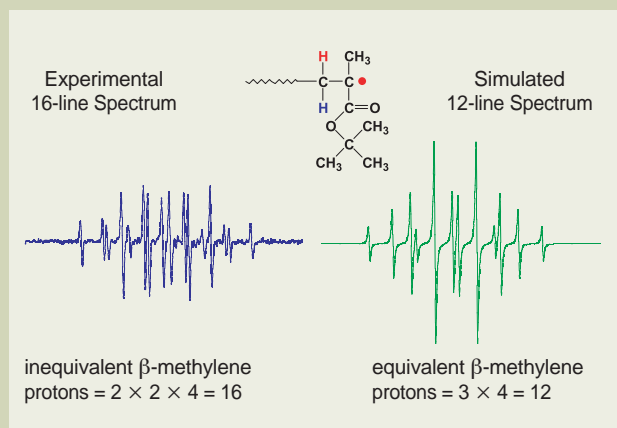
First, a dimeric model radical precursor was

Fig.16 Experimental spectrum for nonequivalent β-methylene protons (16-line spectrum) and simulated spectrum for equivalent β-methylene protons (12-line spectrum) for propagating radical of *t*BMA.
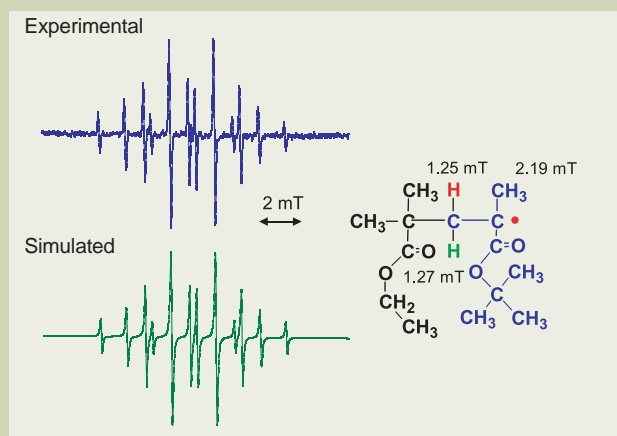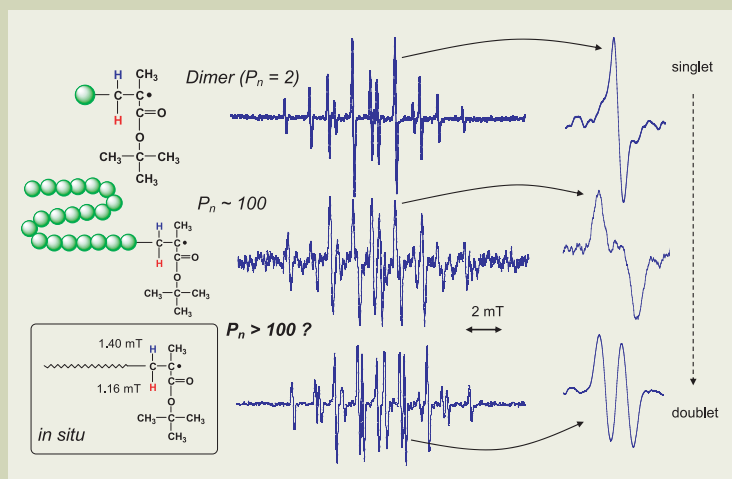

Fig.18 Comparison of ESR spectra of radicals of *t*BMA with various chain length at 150 °C. ESR spectra of dimeric model radical, model radical with P_n = 100, and propagating radial are shown. Characteristic lines were enlarged on the right-hand side.

Fig.17 Experimental and simulated ESR spectra of dimeric model radical of *t*BMA at 150 °C (measurement condition; solvent: toluene, temperature: 150 °C, modulation: 100 kHz, 0.1 mT, time constant: 0.03 sec, sweep time: 15 mT/4 min).
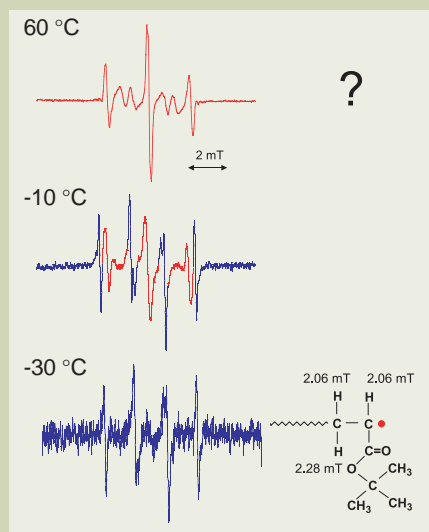

Fig.19 The ESR spectra observed in radical polymerization of *t*BA initiated with *t*BPO under irradiation at -30 °C, -10 °C, and +60 °C (measurement condition; solvent: toluene, 30 % (v/v), modulation: 100 kHz, 0.1 mT, time constant: 0.03 sec, sweep time: 15 mT/4 min).

prepared by ATRP and purified. A model dimeric radical was generated from the precursor. Clear and well-resolved ESR spectra of the model radical were observed at various temperatures. The ESR spectrum of the radical observed at 150 °C showed a 12-line spectrum, as shown in **Figure 17**. The two β-methylene protons are almost equivalent in small radicals at such a high temperature. This finding indicates that rotation of the radical chain end is too fast to detect differences in methylene protons on the time scale of ESR spectroscopy.

In order to estimate the critical chain length which would show splitting resulting in a 16-line spectrum, model radical precursors with degrees of polymerization (P_n) of 30, 50, and 100 were prepared by ATRP. Polymers with calculated molecular weights and low polydispersity were obtained. ESR spectra of radicals generated from these precursors were observed at various temperatures. Although the lifetime of the model radicals are very short at 150 °C, clear and well-resolved spectra were observed. These spectra showed similar temperature dependence to that shown in Figure 6. In the case of P_n = 100, a 16-line spectrum was clearly observed at temperatures lower than 120 °C. The intensity of the inner 8 lines increased with increasing temperature, and seems to coa-

lesce into a single line at 150 °C. Similar ESR spectra were observed in radicals from polymeric precursors with P_n = 50 and 30 where the intensity of the inner 8 lines seems to coalesce more clearly to a single line at 150 °C. The ESR spectra appears to be 12-line spectrum, but the 4 lines coalesced insufficiently, indicating that the rate of the rotation of the end radical is not sufficiently fast for the methylene protons to be detected as equivalent species on the time scale of the ESR experiment. The inner 4 lines of 12-line spectrum begin to separate into two lines at P_n = 30, and the separation becomes larger with increasing Pn owing to the lower rate of rotation. The separation was more clearly observed in the propagating radical, indicating that mobility of the chain end radical is restricted.

Comparison of the ESR spectra of dimeric model radical (Fig. 17), model radicals with P_n = 100, and radicals in polymerization systems (Fig. 7) at 150 °C are shown in one figure, **Figure 18**. A comparison of the separation of the inner lines indicates that P_n of the propagating radical is higher than 100. Values of hyperfine coupling constants measured from these spectra, were plotted against chain lengths. They seemed to show a nearly linear correlation between hyperfine coupling con-

stants and chain lengths in the range up to P_n = 200. Molecular weight (M_n) of the isolated polymers from polymerization system was determined to be 30,000 (P_n = 210) by SEC. The interpretation of the ESR spectra suggests that they correspond to "long" propagating radicals, and are in agreement with SEC. Before these experimental results ESR spectra and overall SEC results did not correlate. However, more experimental results are needed for a comprehensive correlation of kinetic data with ESR spectra.

We can conclude that observation of a 16-line spectrum in ESR measurements can be ascribed to "polymeric" radicals with more than 100 monomer units. Similar differences in ESR spectra were observed for polyMMA radicals generated *in situ* (Fig. 8). Although the spectra are more complicated, with a small quartet due to ester methyl protons, the ESR spectrum of polyMMA recorded during a polymerization showed a basic 16-line spectrum and the dimeric model radical with a terminal MMA radical showed a 12-line spectrum. Therefore ESR spectroscopy has provided structural information on the propagating radicals at their chain ends.

Direct information on the chain length of the radicals from ESR measurements had not been
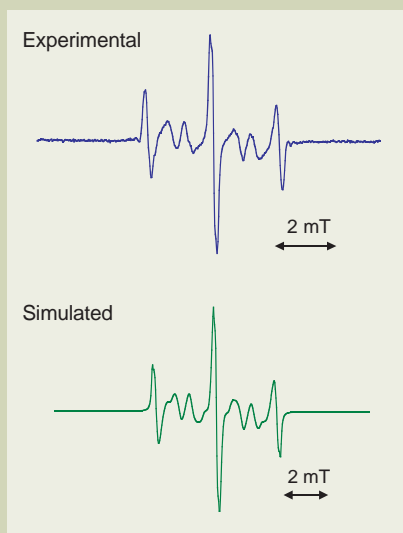
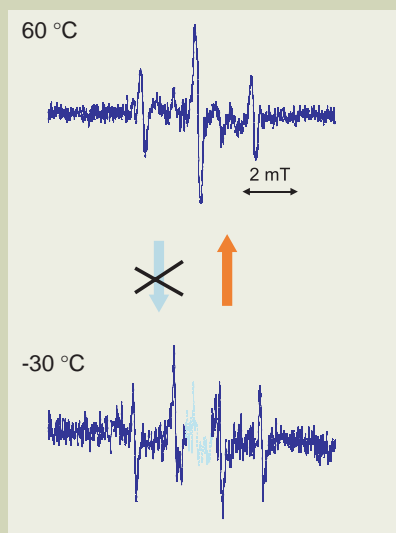Fig.20 Experimental and simulated ESR spectra of radicals in radical polymerization of *t*BA at 60 °C.

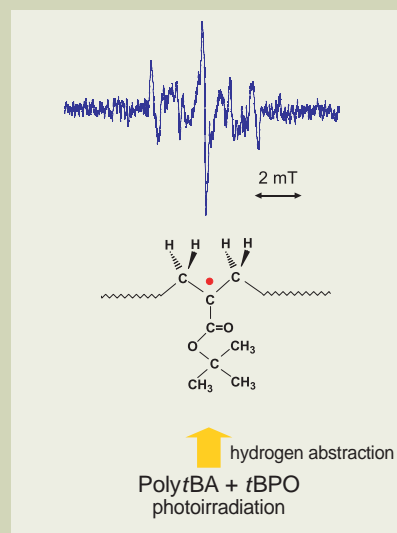Fig.21 ESR spectra of model radical of *t*BA with Pn = 100 at -30 °C and + 60 °C.

Fig.22 EESR spectrum of mid-chain radical generated by hydrogen abstraction from poly*t*BA by peroxide radicals observed at 60 °C.
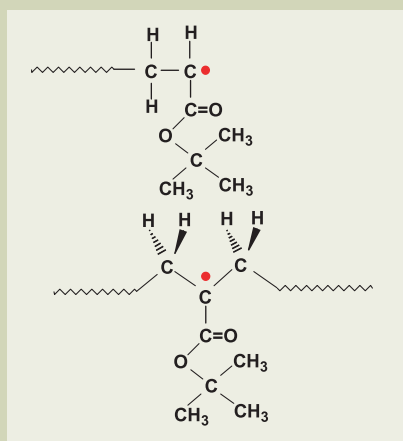

Fig.23 Structure of propagating radical of *t*BA (a) and of mid-chain radical (b).
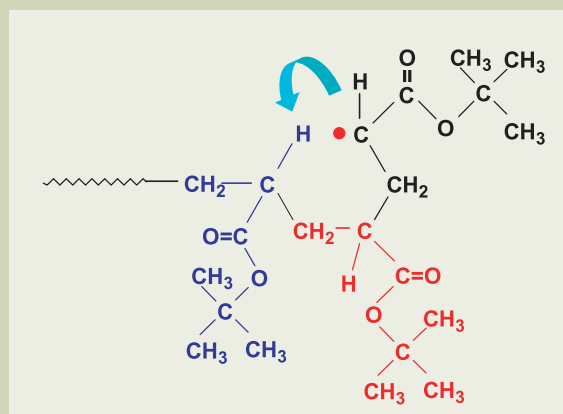

Fig.24 Schematic diagram of potential 1,5-hydrogen shift for propagating *t*BA radical.

reported before and is reported here for the first time.

Further information on the dynamic behavior of the propagating radicals can be obtained from these ESR spectra. The temperature dependence of these spectra can be simulated by consideration of the dynamics of conformational changes of the radicals. The average exchange time between the two conformers was calculated from the simulation of the spectra. The activation energy for rotation of the terminal C_α-C_β bond was estimated to be 21.2 kJ/mol [13].

Clarification of the Mechanism of Chain Transfer Reactions in Radical Polymerizations of Acrylates

ESR Spectra Observed during the Polymerization of *tert*-Butyl Acrylate and Interpretation of the Spectra

Interpretation of ESR spectra observed in acrylate radical polymerizations have been very difficult [34-40]. The ESR spectra observed during radical polymerization of acrylates are very different from those from methacrylates, even under almost identical conditions (**Fig. 19**). Accordingly, it is difficult to interpret the spectrum to be that of propagating radicals. Spectroscopic changes were observed in ESR spectra during the solution polymerization of *tert*-butyl acrylate (*t*BA) as shown in Figure 19. A 6-line spectrum or doublet of triplets with narrow line width was observed at -30 °C. This spectrum can be reasonably assigned to be a propagating radical with two β-methylene protons (1:2:1 triplet) and one α-proton (1:1 doublet). However at 60 °C, a totally different 7-line spectrum with broader line width was observed. The latter spectrum was much easier to observe than the former one, but traces of the 6-line spectrum can be seen in the 60 °C spectrum. However, the amount of species giving rise to the spectrum is 1000 times smaller than the species that are the predominant source of the high temperature spectrum. At -10 °C, overlapped spectra of the first and latter spectrum were observed (Fig. 19). Signal intensity due to the species present in the higher temperature spectrum with broader line width increased with time. These results suggest that the species responsible for the spectrum observed at -30 °C converted to the species providing the spectrum observed at 60 °C. Some reaction should be responsible for such a change. Similar findings were observed for other acrylates, e.g.

methyl acrylate, dodecyl acrylate, phenyl acrylate, and others. Two potential explanations for this change have been considered. One is a chain-length dependence of the spectra and the other is chemical transformation (e.g. transfer). These possibilities were examined by analysis of the ESR spectra of model radicals with various chain lengths generated from polymeric radical precursors prepared by ATRP. This analysis helped to resolve the ambiguity.

Precursors of acrylate $P_n\bullet$ with n = 15, 50, and 100 were prepared by ATRP. Polymers with calculated molecular weights and low polydispersities were obtained. The model radicals were generated by a reaction with organotin compounds and the radicals were observed by ESR spectroscopy [27]. The ESR spectrum observed for $P_n = 100$ are shown in **Figure 20**. The radicals provided almost the same 6-line (doublet of triplets) ESR spectra of propagating radicals present at low temperature (-30 °C) as shown in Figure 19. The observed 6-line spectra changed after raising the temperature to 60 °C, and the change in the spectrum is in agreement with the ESR spectra observed directly during the radical polymerization. The model systems do not contain any monomer and the spectroscopic change occurred without propagation. This suggests

that a chemical reaction is responsible for the observed changes. The chemical reaction maybe a chain transfer reaction from the initially formed terminal radicals to form mid-chain radicals as discussed earlier for radical polymerizations of acrylates.

One additional piece of evidence supporting the formation of a mid-chain radical was obtained from an examination of hydrogen abstraction from polyacrylates. This mid-chain radical can be formed by hydrogen abstraction from polyacrylates by oxygen centered radicals. Poly*t*BA and *tert*-butyl peroxide (*t*BPO) were dissolved in benzene, under irradiation the mixture gave the ESR spectra shown in **Figure 21**. The spectrum was very similar to both the spectra observed in the polymerization system (Fig. 19) and that reported by Westmoreland *et al* [40]. Furthermore, it was convincingly simulated by consideration of the structure of two sets of methylene protons in restricted rotation at both sides of the mid-chain radical, as shown in **Figure 22**. Consequently, the radical observed at high temperatures (Fig. 19) is due to formation of mid-chain radicals.

A 1,5-hydrogen shift to form a mid-chain radical has previously been considered for radical polymerization of acrylates [36-40]. Yamada *et al*. observed ESR spectra similar to those in Figures 19 and 21, and reported that the spectra were due to a mixture of propagating and mid-chain radicals [38,39]. However, there has been no clear experimental evidence or clear explanation for the formation of the mid-chain radicals.

Here, a clear interpretation of the ESR spectra of propagating (**Fig. 23a**) and mid-chain radicals (**Fig. 23b**) was demonstrated with the aid of molecules prepared by ATRP. The proposed mechanism for the 1,5-hydrogen shift is shown in **Figure 24**. Formation of a six-membered ring enables the radical to migrate to the monomer unit two units before the terminal unit. Since this shift needs at least linked three monomer units, it suggests that mid-chain radicals cannot be formed from a dimeric radical. A dimeric radical precursor was isolated from a mixture of oligomeric radical precursors, and the ESR spectrum of the dimeric radical was measured. The ESR spectra of the dimeric model radical showed no change even at relatively high temperature (40 °C). From the same mixture of oligomers, a mixture of oligomers, with tetramer to hexamer (4-6 monomer units) was also separated and radicals were generated from the oligomers. The ESR spectra of the mixture of radicals showed overlapped spectra from two separate spectra from the beginning of the reaction. This absence of chain length dependence and no changes for the dimer strongly suggest a formation of mid-chain radicals in radical polymerizations of acrylates via a 1,5-hydrogen shift reaction.

It is known that polyacrylates prepared by conventional radical polymerization procedure have many branches [41, 42]. An ESR study has now provided direct evidence for the origin of the branching. It should be also noted that an estimate of k_p for acrylates is difficult by ESR which would provide the sum of the concentration of the much more active growing terminal radicals and less active mid-chain radicals.

Clarification of Mechanism of Radical Migration using Uniform Oligomeric Model Radicals

Since changes from low temperature spectrum to the one at higher temperature were clearly observed, even in model radical systems with fixed chain lengths, the possibility of chemical transformation remained. The ambiguity was solved by ESR spectroscopy of several purified oligomeric model radical precursors prepared by ATRP. GPC elution diagrams of model radical precursors of dimer, trimer, tetramer, and pentamer are shown in **Figure 25** along with the GPC of a mixture of the oligomers. As shown in the figure, separation and purification of the oligomers were successful. Model radicals with clearly defined structures were generated by the reaction of the corresponding alkyl bromides (H-ethyl acrylate (EA)-*t*BA-Br, H-EA-*t*BA-*t*BA-Br, H-EA-*t*BA-*t*BA-*t*BA-Br, H-EA-*t*BA-*t*BA-*t*BA-*t*BA-Br) with an organotin compound under irradiation. The resulting radicals had structures of hydrogenated radicals, i.e., H-EA-tBA•, H-EA-*t*BA-*t*BA•, H-EA-*t*BA-*t*BA-*t*BA•, and H-EA-*t*BA-*t*BA-*t*BA-*t*BA• respectively. Each of these radicals was investigated by ESR spectroscopy at various temperatures. Clear well-resolved spectra were observed and precise values for hyperfine coupling constants were determined from the spectra.

The ESR spectrum of the dimeric radical (H-EA-*t*BA·) showed a doublet of triplets in each spectrum taken at various temperatures within the range of -30 to +150 °C. The doublet and triplet can reasonably be considered to be due to the splitting from the α-proton and two equivalent β-methylene protons, respectively. Nothing happened to the dimeric radical even at higher temperatures (**Fig. 26**). On the other hand, model trimeric and tetrameric radicals showed a clear temperature dependent irreversible change, as discussed below.

In the case of the model trimeric radical (H-EA-*t*BA-*t*BA•), the spectrum observed at -30 °C (**Fig. 27**) was very similar to that of the dimeric radical. This spectrum is ascribed to a chain end radical as shown in the figure. ESR spectra were measured every 30 degrees as the temperature was increased from -30 °C to 120 °C. As the temperature was raised, the spectrum gradually and irreversibly changed to a different one. From 0 °C to 60 °C, the observed spectra were attributalbe to two kinds of overlapping spectra. The change was complete at 120 °C. The resulting spectrum, observed at higher temperatures, was totally different from that at lower temperatures (Fig. 27). When a 1,5-hydrogen shift occurs, the
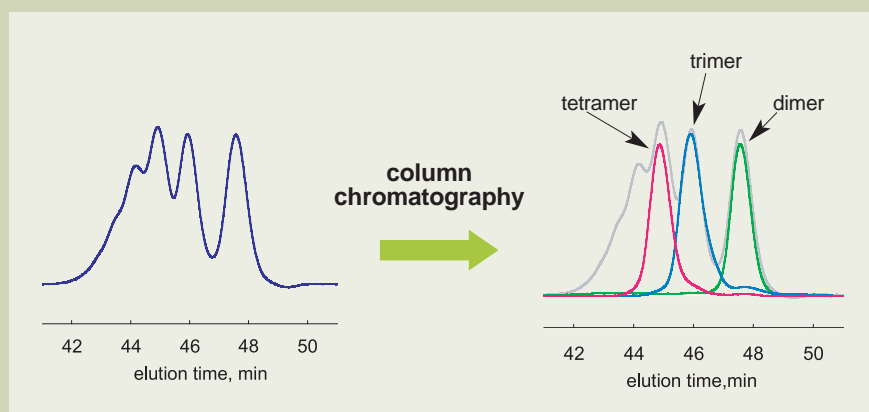

Fig.25 SEC elution diagram of purified dimer, trimer, and tetramer of *t*BA as uniform radical precursor along with that of mixture of oligomers (before purification).
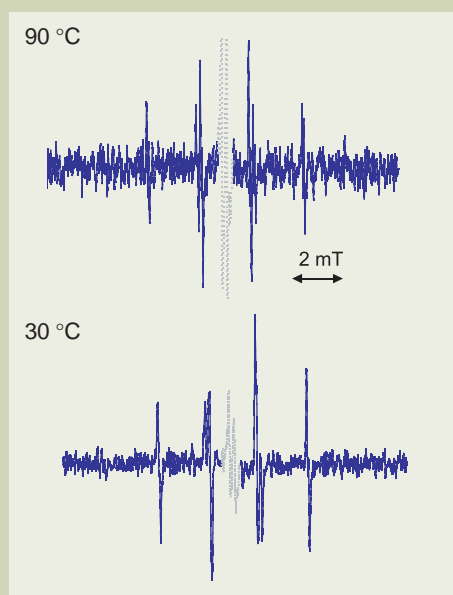

Fig.26 ESR spectra of dimeric model radical of *t*BA at 30 °C and 90 °C in toluene (measurement condition; modulation: 100 kHz, 0.05 mT, time constant: 0.03 sec, sweep time: 15 mT/4 min).

radical should migrate from one end to the other end of the trimeric model radical as shown in Figure 27. The spectrum can be simulated using the hyperfine splitting constants shown in the figure. The most important feature of this simulation is a small triplet that appeared in each spectroscopic line. When this trimer was prepared by ATRP, ethyl 2-bromo propionate was used as the initiator and the initiator fragment was counted as first monomer unit. So, we only had an ethyl ester group at the other chain end. The presence of a small triplet clearly indicates that the radical is located on the first ethyl acrylate unit. Consquently, we can say that the radical migrated from one end to the other end of the trimer.

A similar ESR study was done for the tetrameric model radical (H-EA-*t*BA-*t*BA-*t*BA•). The ESR spectra at -30 °C and 120 °C are shown in **Figure 28**. The low temperature spectrum, observed at -30 °C, was very similar to those from the dimeric and trimeric model radicals. A similar irreversible spectroscopic change took place, as in the case of the trimeric model radical, at higher temperatures. However the final spectrum was different from that of the trimeric model radical. In the case of a tetrameric model radical, a 1,5-hydrogen shift would cause transfer of a radical from the chain end to the first *t*BA unit, which is located

two units before the other end unit, through a six-membered ring structure (Fig. 28). The transferred radical should have mid-chain type structure with methylene groups at both sides (H-EA-*t*BA(•)-*t*BA-*t*BA-H). The spectrum of the radical at 120 °C shown in Figure 28 is ascribable to such a mid-chain radical. These findings provide clear experimental evidence of a 1.5-hydrogen shift at the propagating chain end of acrylate radical polymerizations.

A pentameric model radical was also generated and observed by ESR and a similar temperature dependent spectroscopic change to those seen in the case of the trimer and tetramer was observed. The resulting high temperature spectrum is very similar to those observed in polymeric acrylate radicals.

These findings strongly suggest that the mechanism of the chain transfer reaction in an acrylate radical polymerization is a 1,5-hydrogen shift that ocurrs through a six-membered ring structure. Formation of a six-membered ring is a kinetically favored process and the transfer occurred from a secondary radical to form a thermodynamically more stable tertiary radical. One further piece of information can be obtained from the result of the pentamer radical since the pentamer provides one more chance to migrate from a mid-chain radical to the other chain end. However, this migration

was not observed for the pentameric model radical which has H-EA-*t*BA-*t*BA-*t*BA-*t*BA• structure. The reason for this is unresolved.

Although there may be some minor contribution of intermolecular chain transfer, these systematic studies have provided a clearer perspective of the mechanism of the chain transfer reaction of propagating acrylate radicals. With increasing molecular weight, other factors also are becoming more important like conformation (rigidity), side group bulkiness and statistics. Further investigation will provide decisive proof of the mechanism.

Summary and Perspective

When the ESR spectra obtained by direct detection in a radical polymerization processes are compared with those of model radicals generated from well defined radical precursors prepared by ATRP, it is easier to understand what happens at each step of the elementary processes involved in radical polymerizations. This information help define the reaction mechanisms, which otherwise have been speculated upon without direct experimental evidence. ESR spectroscopy has provided unambiguous proof of the process for several reactions involved in radical polymerization with
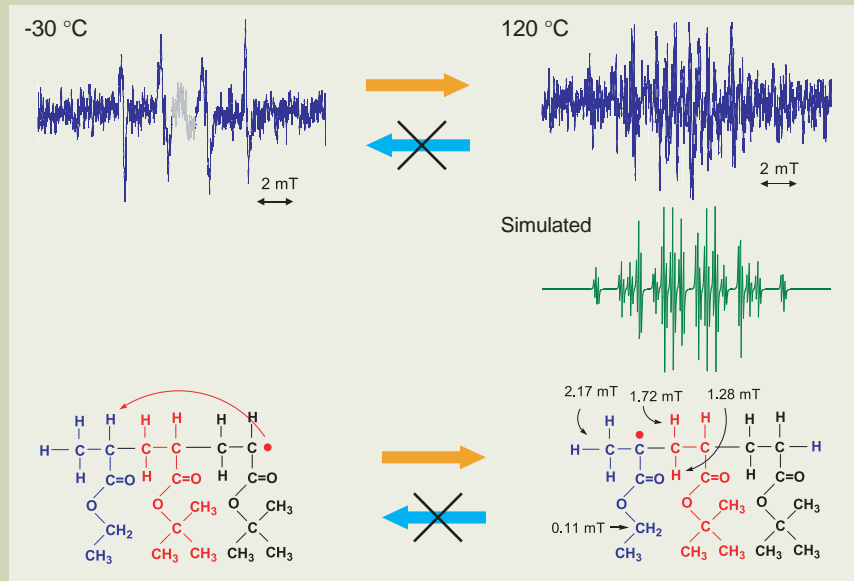

Fig.27 Temperature dependent spectroscopic change in ESR spectra of trimeric model radical of *t*BA Raise of the temperature caused remarkable spectroscopic change from -30 °C to + 120 °C (measurement condition at -30 °C; solvent: toluene, modulation: modulation: 100 kHz, 0.1 mT, time constant: 0.03 sec, sweep time: 15 mT/4 min, at +120 °C; solvent: mesitylene, modulation: 100 kHz, 0.05 mT, time constant: 0.03 sec, sweep time: 15 mT/4 min).

Fig.28 Temperature dependent spectroscopic change in ESR spectra of tetrameric model radical of *t*BA Raise of the temperature caused remarkable spectroscopic change from -30 °C to + 120 °C (measurement condition at -30 °C; solvent: toluene, modulation: modulation: 100 kHz, 0.1 mT, time constant: 0.03 sec, sweep time: 15 mT/4 min, at +120 °C; solvent: mesitylene, modulation: 100 kHz, 0.05 mT, time constant: 0.03 sec, sweep time: 15 mT/4 min).
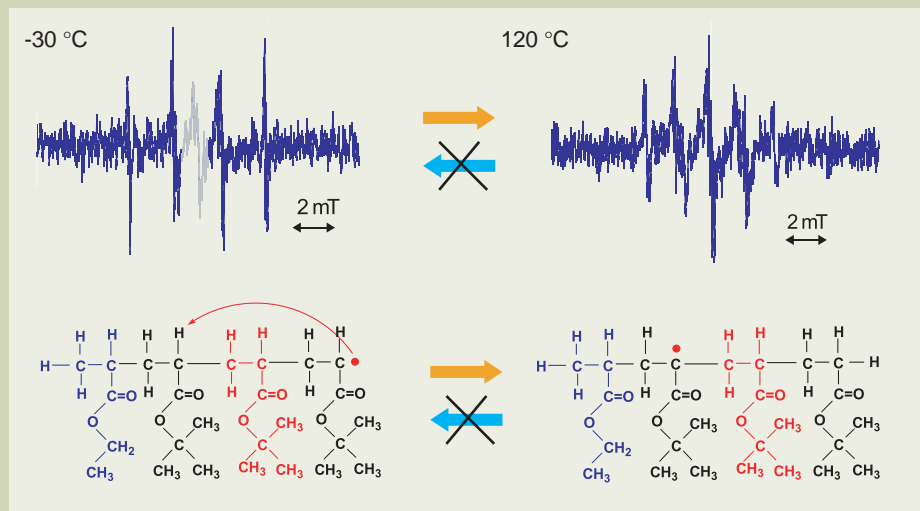
the aid of materials prepared by controlled radical polymerization techniques. In general this approach can be applied to any chemical reaction, not only a radical reaction, which has well-defined starting materials and final products but ambiguous intermediate products.

Research using uniform oligomeric model radicals provides the possibility for expansion of the research field. In general, precise quantum chemical calculations are difficult to apply for polymeric radicals with long chain lengths but theoretical calculations can be conducted for such small radicals. The small radicals can provide highly resolved ESR spectra and they can provide precise values of hyperfine splitting constants. Polymeric radicals usually show larger line width making the precise determination of the splitting constants more difficult. The values are strongly related to electronic nature of the radicals and can be evaluated by the results of the calculations. ESR itself is a quantum mechanical phenomenon. The combination of ESR, ATRP, and theoretical calculations lead the way to study of a deeper connection between experimental results and theoretical calculations.

ESR was also employed to examine and quantify some intermediates in ATRP, to provide a deeper understanding of the ATRP process, including identification of the structure and concentration of the paramagnetic species involved in the process [14, 30, 43-48]. Although it is very interesting and important for investigation of ATRP, the structural features of the paramagnetic transition metal compounds will not be discussed in this paper.

Experimental

Monomers, initiators, copper salts, and ligands were purified in the usual manner. Presence of carbon-bromine terminal groups and chain lengths of the radical precursors were checked by measurements of Electron Spray Ionization (ESI) mass spectra. Generation of model radicals from precursors was conducted by a reaction with an organotin compound under irradiation. ESR spectra of radicals were recorded on a JEOL JES RE-2X spectrometer operating in the X-band, utilizing a 100 kHz field modulation, and a microwave power of 1 mW. A TE_{011} mode universal cavity was used. Measurement temperature was controlled by JEOL DVT2 variable-temperature accessory. ESR measurements were mainly performed in mesitylene at 150 and 120 °C and in toluene at 90, 60, 30, 0, and -30 °C. Spectroscopic simulations were carried out by JEOL IPRIT Data Analysis System. Molecular weights and molecular weight distributions were roughly estimated using a TOSOH CCP&8020 series GPC (SEC) system with TSK-gel columns. Polystyrene standards were used to calibrate the columns.

Acknowledgements

References

[1] H. Fischer, *Adv. Polym. Sci.,* **5**, 463 (1968).

[2] H. Fischer, "Polymer Spectroscopy" D. O. Hummel, ed., Springer Verlag, Berlin (1974), pp. 289-354.

[3] H. Fischer, *Z. Naturforsch.,* **19a**, 866 (1964)

[4] H. Fischer, *Z. Naturforsch.,* **19a**, 866 (1964)

[5] M. Kamachi, *Adv. Polym. Sci.*, **82**, 207 (1987).

[6] B. Yamada, D. G. Westmoreland, S. Kobatake, and O. Konosu, *Prog. Polym. Sci.,* **24**, 565 (1999).

[7] A. Matsumoto and B. Giese, *Macromolecules*, **29**, 3758 (1996)

[8] M. Spichty, B. Giese, A. Matsumoto, H. Fischer, and G. Gescheidt, *Macromolecules*, **34**, 723 (2001).

[9] H. Tanaka, T. Kagawa, T. Sato, and T. Ota, *Macromolecules*, **19**, 936 (1986).

[10] M. Kamachi, *J. Polym. Sci., Part A:. Polym. Chem.*, **40**, 269 (2002).

[11] M. Kamachi and A. Kajiwara, *Macromol. Symp.*, **179**, 53 (2002).

[12] A. Kajiwara and K. Matyjaszewski, "Advanced ESR Methods in Polymer Research", Wiley Interscience, NJ. **2006**, Chapter 5, pp. 101-132.

[13] A. Kajiwara, K. Maeda, N. Kubo, and M. Kamachi, *Macromolecules*, **36**, 526 (2003).

[14] A. Kajiwara, K. Matyjaszewski, and M. Kamachi, "Controlled/Living Radical Polymerization", ACS Symposium Series 768, K. Matyjaszewski, ed., American Chemical Society, Washington, DC (2000), pp. 68-81.

[15] M. Kamachi and A. Kajiwara, *Macromolecules*, **29**, 2378 (1996)

[16] A. Kajiwara and M. Kamachi, *Macromol. Chem. Phys.*, **201**, 2160 (2000).

[17] "Controlled Radical Polymerization", ACS Symposium Series, 685, K. Matyjaszewski, ed., American Chemical Society, Washington, DC (1998).

[18] "Controlled/Living Radical Polymerization", ACS Symposium Series, 768, K. Matyjaszewski, ed., American Chemical Society, Washington, DC (2000).

[19] "Advances in Controlled/Living Radical Polymerization" ACS Symposium Series, 854, K. Matyjaszewski, ed., American Chemical Society, Washington, DC (2003).

[20] J.-S. Wang and K. Matyjaszewski, *J. Am. Chem. Soc.*, **117**, 5614 (1995).

[21] J.-S. Wang and K. Matyjaszewski, *Macromolecules*, **28**, 7901 (1995).

[22] T. E. Patten and K. Matyjaszewski, *Adv. Mater.,* **10**, 901 (1998).

[23] V. Coessens, T. Pintauer, and K. Matyjaszewski, *Prog. Polym. Sci.,* **26**, 337 (2001).

[24] K. Matyjaszewski and J. Xia, *Chem. Rev.*, **101**, 2921 (2001).

[25] M. Kamigaito, T. Ando, and M. Sawamoto, *Chem. Rev.*, **101**, 3689 (2001).

[26] K. A. Davis and K. Matyjaszewski, *Adv. Polym. Sci.*, **159**, 2 (2002).

[27] B. Giese, W. Damm, F. Wetterich, and H.-G. Zeitz, *Tetrahedron Lett.*, **33**, 1863 (1992).

[28] M. Kamachi and A. Kajiwara, Macromol. *Chem. Phys,.* **198**, 787 (1997).

[29] M. Kamachi and A. Kajiwara, Macromol. *Chem. Phys.*, **201**, 2165 (2000).

[30] A. Kajiwara, M. Kamachi, M. "Advances in Controlled/Living Radical Polymerization", ACS Symposium Series 854, K. Matyjaszewski, ed., American Chemical Society, Washington, DC (2003), pp. 86-100.

[31] A. Kajiwara, *Kobunshi Ronbunshu*, **2004**, 61(4), 237-249.

[32] A. Kajiwara, *Macromolecular Symposia*, 248, **2007**, pp. 50-59

[33] A. Kajiwara, ACS Symposium Series 944; K. Matyjaszewski, ed., American Chemical Society, Washington, DC., **2006**; Chapter 9, pp. 111-124.

[34] M. E. Best and P. H. Kasai, *Macromolecules*, **22**, 2622 (1989).

[35] B. G. Gilbert, J. R. Lindsay Smith, E. C. Milne, A. C. Whitwood, and P. Taylor, *J. Chem. Soc., Perkin Trans.*, 2, **1993**, 2025.

[36] D. C. Doetschman, R. C. Mehlenbacher, and D. Cywar, *Macromolecules*, **29**, 1807 (1996).

[37] Y. Sugiyama, *Bull. Chem. Soc., Jpn.*, **70**, 1827 (1997).

[38] M. Azukizawa, B. Yamada, D. J. T. Hill, and P. J. Pomery, *Macromol. Chem. Phys.*, **201**, 774 (2000).

[39] B. Yamada, M. Azukizawa, H. Yamazoe, D. J. T. Hill, and P. J. Pomery, *Polymer*, **41**, 5611 (2000).

[40] H. R. Chang, W. Lau, H.-Y. Parker, and D. G. Westmoreland, *Macromol. Symp.*, **111**, 253 (1996).

[41] F. Heatley, P. A. Lovell, and T. Yamashita, *Macromolecules*, **34**, 7636 (2001).

[42] N. M. Ahmad, F. Heatley, and P. A. Lovell, *Macromolecules*, **31**, 2822 (1998).

[43] A. Kajiwara, A. K. Nanda, and K. Matyjaszewski, *Macromolecules*, **37**, 1378 (2004).

[44] K. Matyjaszewski and A. Kajiwara, *Macromolecules*, **31**, 548 (1998).

[45] A. Kajiwara and K. Matyjaszewski, *Macromol. Rapid Commun.*, **19**, 319 (1998).

[46] A. Kajiwara and K. Matyjaszewski, and M. Kamachi, *Macromolecules* **31**, 5695 (1998).

[47] A. Kajiwara and K. Matyjaszewski, *Polym. J.* **31**, 70 (1999).

[48] B. Knuehl, T. Pintauer, A. Kajiwara, H. Fischer, and K. Matyjaszewski, *Macromolecules*, **36**, 8291 (2003).

Characteristic Features of JIB-4500 MultiBeam System

Toshiaki Suzuki

Metrology Inspection Division, JEOL Ltd.

Introduction

The JIB-4500 is a multifunctional MultiBeam System that combines both a high-resolution SEM (scanning electron microscope) and a high-performance FIB (focused ion beam) into one chamber. It enables you to perform cross-sectional milling, SEM observation, and X-ray analysis in one instrument. In this paper, a brief overview of the instrument and its applications are given.

Features of JIB-4500

The JIB-4500 is a MultiBeam System that incorporates a SEM equipped with a high-brightness LaB_6 electron gun and a high-performance FIB in one chamber. **Figure 1** shows the appearance of the JIB-4500 and **Table 1** lists its principal performance. This instrument can perform SEM observation and various analyses such as EDS (energy dispersive spectroscopy), without exposing a specimen to the atmosphere after cross-sectional milling by FIB. This feature offers not only greatly reduced experiment time but also observation and analysis of the specimen with an uncontaminated surface, because the surface of the specimen is not exposed to the atmosphere. Thus, this instrument is very useful for obtaining true specimen information. **Figure 2** shows SEM images (BEI: backscattered electron image and SEI: secondary electron image), an SIM (scanning ion microscope) image and EDS analysis results of a chip capacitor subjected to cross-sectional milling. In addition, this instrument allows live monitoring of SEM BEI collected by a backscattered-electron detector during the specimen milling with an ion beam. This capability enables you to stop milling at a suitable depth. **Figure 3** shows an example of live monitoring of cross-sectional milling applied to silver wax.

Furthermore, a special feature of this MultiBeam System is a function that mills the specimen multiple times at a constant step, and automatically acquires SEM images for every step (S^3 TM: Serial Slicing and Sampling). The use of this innovative function enables you to intuitively grasp the accurate three-dimension-al (3D) structure of the specimen. Moreover, using a 3D reconstruction software program, a 3D reconstructed image can be created. S^3 TM is particularly useful because this function can be applied to a relatively large structure with a thickness from several micrometers to several tens of micrometers, which is difficult to analyze by TEM Tomography. **Figure 4** shows sequential SEM BEIs obtained by S^3 TM and reconstructed images of silver wax. **Figure 5** shows sequential SEM SEIs and reconstructed images of pollens of pine, which are obtained in the same manner as shown in Fig. 4.

The JIB-4500 incorporates a large specimen stage that accommodates a specimen with a diameter up to 76 mm. **Table 2** shows the performance of the specimen stage. To make various analysis applications possible, the JIB-4500 is provided with attachment ports for EDS, EBSD (electron backscatter diffraction), CLD (cathodoluminescenc), etc.

Conclusion

The JIB-4500 MultiBeam System enables efficient FIB cross-sectional milling, SEM observation, and various analyses such as EDS analysis. This instrument is very useful for a wide variety of applications, including material analysis, failure analysis of electronic parts, and specimen preparation for SEM and TEM.

Fig.1 Appearance of the JIB-4500.

Table 1 Principal performance of the JIB-4500.

	FIB	SEM
Emitter	Ga liquid-metal ion source	LaB_6
Accelerating voltage	1 to 30 kV (steps)	0.3 to 30 kV (steps)
Magnification	× 30, × 100 to 300,000	× 5 to 300,000
Image resolution	5 nm (at 30 kV)	2.5 nm (at 30 kV)
Maximum probe current	30 nA (at 30 kV)	1 μA (at 30 kV)

X-ray Mapping

Sn L   Pb M
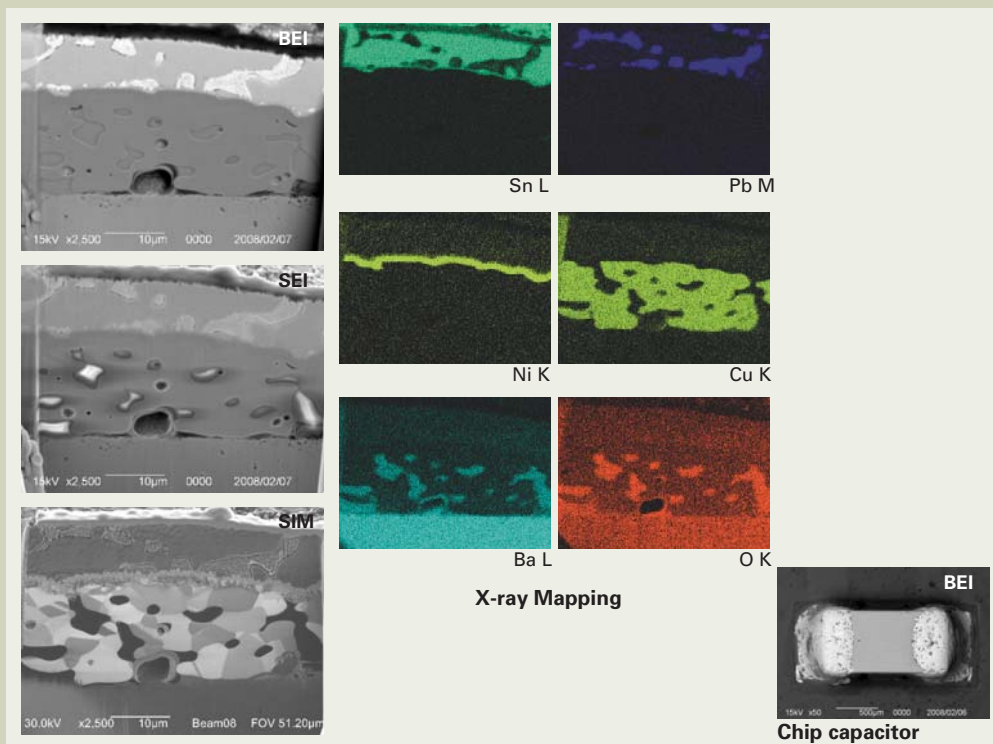
Ni K   Cu K

Ba L   O K

Chip capacitor

Fig.2 SEM images (BEI and SEI), an SIM image and EDS X-ray mapping results of a chip capacitor subjected to cross-sectional milling. A specimen can be imaged with SEM and analyzed immediately after it is subjected to cross-sectional milling by FIB.
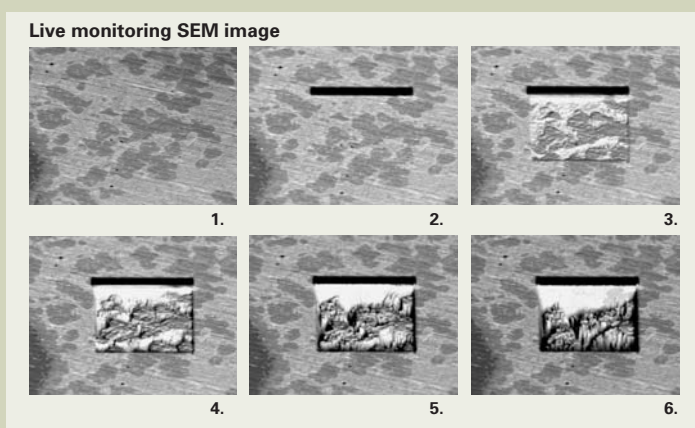
Live monitoring SEM image

1.   2.   3.
4.   5.   6.

Fig.3 SEM (BEI) enables real-time observation of the FIB-milling state.

Reconstructed image

Fig.4 Automatically acquired SEM BEIs obtained by $S^{3\ TM}$ at constant steps, and reconstructed images based on these SEM images (specimen: silver wax).
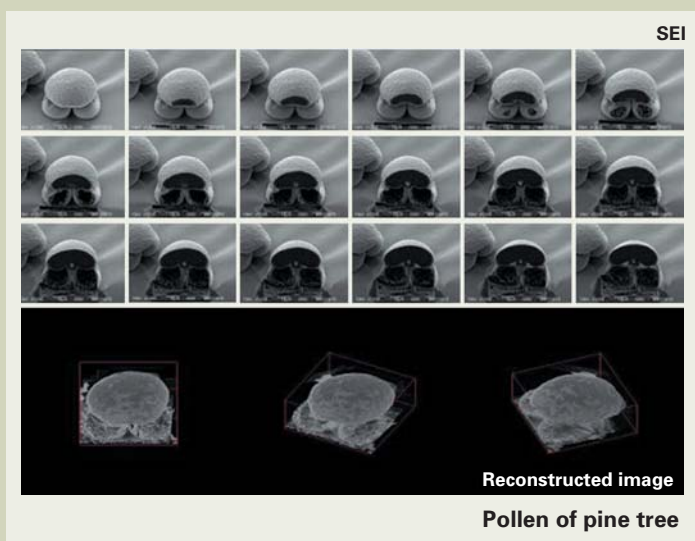

Reconstructed image

Pollen of pine tree

Fig.5 Sequential SEM SEIs acquired by $S^{3\ TM}$ and reconstructed images in the same manner as shown in Fig.4 (specimen: pollens of pine). This function is useful for biological specimens.
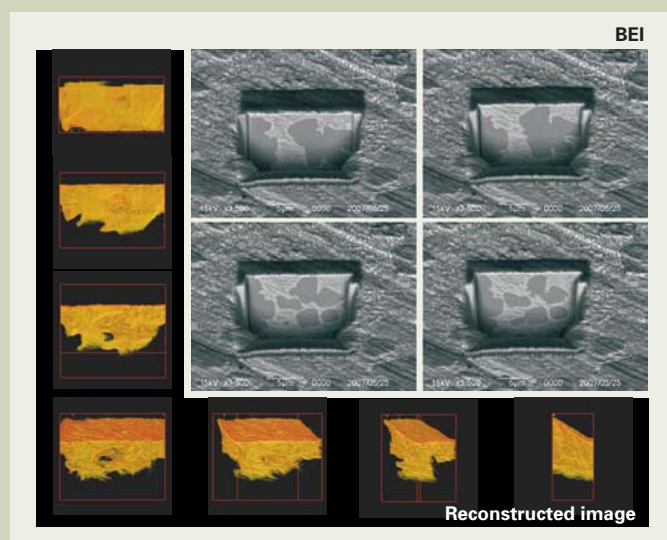
Table 2 Performance of the JIB-4500 specimen stage.

Movement range	X	(mm)	76
	Y	(mm)	76
	Z	(mm)	43
	Fine Z	(mm)	4
	Tilt	(deg)	– 5~60
	R	(deg)	360
Maximum specimen size		(mm)	76 Ø
Airlock chamber standard			

High Power Electron Beam Source Used for Melting Metal Materials

Osamu Sugiyama and Tsutomu Katoh

Industrial Equipment Division, JEOL Ltd.

Introduction

The JEBG-3000UB High Power Electron Beam Source produces a high-power electron beam with a maximum beam output of 300 kW, thus the JEBG-3000UB is used for melting and purifying metal materials. In this paper, an example of applying the JEBG-3000UB High Power Electron Beam Source to the production process of polycrystalline Si, and the features of the JEBG-3000UB are described.

Solar Cell

Photovoltaic power generation has been drawing much attention as clean, recyclable energy, and various materials are studied for this power generation. These materials are divided roughly into three categories, silicon, compound semiconductor and organic material. **Table 1** shows conversion efficiencies for each category and their features [1].

The solar cell using crystalline Si has a high conversion efficiency of 13 to 18%, and also has a long service life of 30 years. Thus, the solar cell dominates about 80% of the total production of photovoltaic power generation. In addition, its applications cover a wide range of fields, such as solar-roof power generation, outdoor lighting, power for RV cars, boats, ships and irrigation pumping, and power for areas isolated from electric transmission lines.

It is predicted that the production of solar cells will rise with a high annual increase rate of 30 to 40%. However, polycrystalline Si materials fall short of this expected production increase. Thus, a major key factor that we are encountering is whether we can supply enough polycrystalline Si materials to satisfy the production needs of solar cells.

Supply of Polycrystalline Si Materials

The production capacity of polycrystalline Si materials in the world, including those for semiconductors, is about 40,000 tons per year. This worldwide production capacity is predicted to be more than 100,000 tons in 2010, as shown in **Fig. 1** [2], [3]. It should be noted that the production capacity in 2007 and subsequent years is an estimate that totals production increases announced in the production plans of semiconductor material companies.

Although a high purity of eleven nines (99.999999999%) is required for Si materials for the semiconductor industry, as for Si materials for the solar cell, a purity of six nines (99.9999%) is enough.

As typical production methods of polycrystalline Si materials, the Siemens method and the melted Si purification method are described.

Siemens method

This method first vaporizes Si metal (purity: 99%) to generate trichlorosilane (SiCl$_3$), and finally purifies Si. Then, the Si is solidified again [4-6]. The procedure is as follows.

1) Si metal and hydrochloric acid (HCl) are reacted to produce liquid trichlorosilane (SiCl$_3$).
2) Distillation and purification of trichlorosilane are repeated to highly purify it.
3) In a deposition chamber (**Fig. 2**), a Si rod is heated to about 1000 °C. By passing trichlorosilane (SiCl$_3$) and hydrogen through the chamber, high-purity poly crystalline Si is deposited on a Si rod. As a result, Si with a high purity of eleven nines is obtained.

Melted Si purification method

The melted Si purification method developed by the NEDO project is described [6], [7].

In this method, Si metal (purity: 99%) is used as a starting material. While Si is kept in the solid phase, impurity elements contained in the Si are removed and Si for solar cells is produced. Si with a purity of six nines is obtained. Although the purity of the Si is low compared with the purity obtained by the Siemens method, the melted Si purification method has several advantages. That is, the energy needed to produce Si is very low, and the capital investment for the production of Si materials can be held down to a low level.

To be more precise, the melted Si purification method consists of the first process and the second process. The first process includes phosphorous (P) removal and rough removal of metal impurities, and the second process

Table 1 Conversion efficiencies and features of various solar cells.

|	Typical category	Power generation efficiency (%)	Main features
Silicon system	Polycrystal type	13 -17	For mass production
	Single-crystal type	16 -18	High conversion efficiency
	Ribbon	16	Slice process not required
	Thin film type	7 -12	Deposition with low temperature, large area, and multi-layers is possible.
Compound semiconductor	Single-crystal type (GaAs)	30 -40	High conversion efficiency High cost
	Polycrystal type (CIGS,CdTe)	13	Rare metal used There is little energy at the time of production.
Organic system	Dye-sensitization type	6	Vacuum and high-temperature process not required Low cost is possible.
	Organic thin film type	4	Research-and-development stage
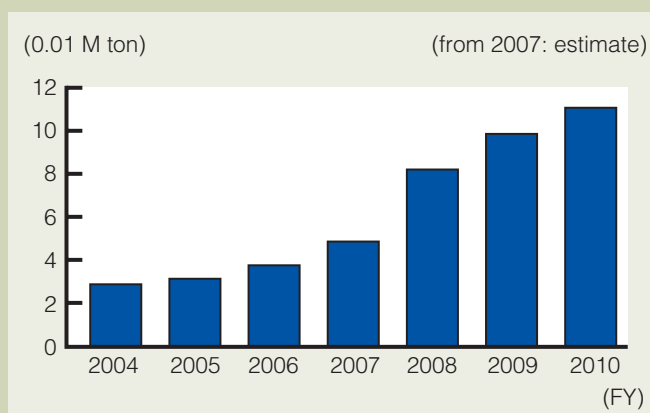
Fig.1 Production capacity of polycrystalline Si in the world.
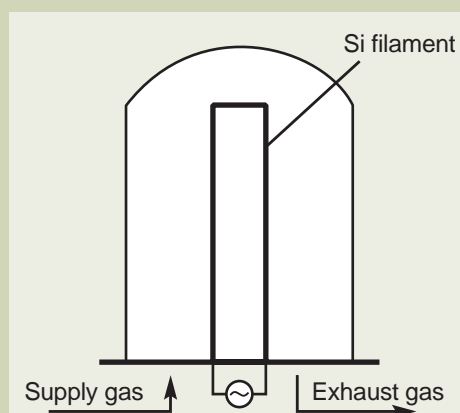(Source : RTS Corporation)

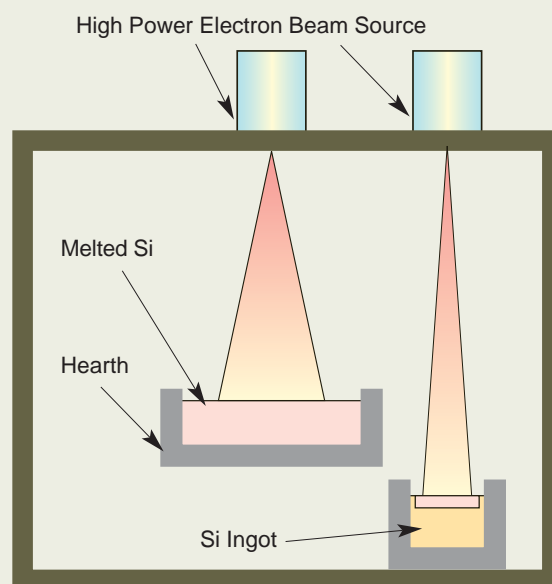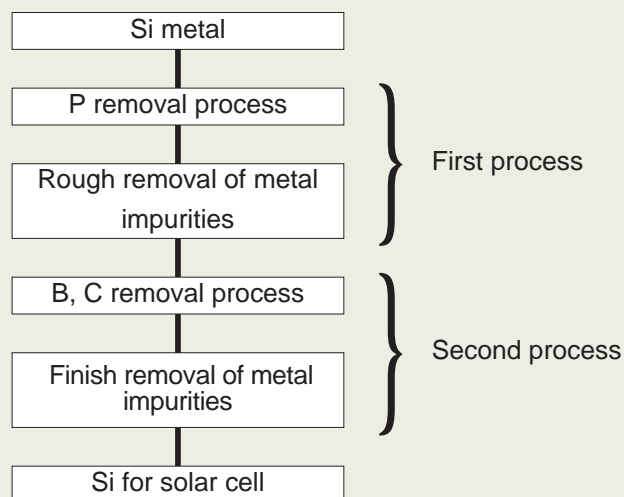Fig.2 Schematic diagram of Siemens method.

Fig.3 Process and schematic diagram of melted Si purification method.

includes boron (B) and carbon (C) removal, and finish removal of metal impurities (**Fig. 3**).

P removal is performed by the electron beam vacuum-melting method. Si metal is irradiated with a high-power electron beam, and the Si metal is dissolved. Depending on the difference of vapor pressure, P is vaporized preferentially and the purity of Si is raised.

JEOL 300 kW High Power Electron Beam Source

The JEBG-3000UB 300 kW High Power Electron Beam Source, developed by JEOL, is used for the purification of polycrystalline Si materials for solar cells by means of the melted Si purification method.

Figure 4 shows the appearance of the JEBG-3000UB.

Specifications

Table 2 shows the specifications for the JEBG-3000UB [8].

The maximum beam output is 300 kW (at an accelerating voltage of 40 kV and a maximum emission current of 7.5 A).

Structures and features

Figure 5 shows the electron optical system of the High Power Electron Beam Source. This electron optical system is roughly divided into three systems.
(1) The illumination system consisting of a filament, a tungsten (W) cathode, a Wehnelt, and an anode.
(2) The imaging system consisting of the 1st lens and the 2nd lens.
(3) The scan system consisting of a dynamic

focusing lens, an astigmatism correction coil, and an X/Y deflection coil.

The bombardment method is employed for the illumination system. The bombardment method generates thermoelectrons with heating of a filament, heats a disk-shaped W cathode, and then generates an electron beam from the W cathode. This bombardment method is superior to the filament method, in terms of the following three points.
(a) An electron beam with higher current density is obtained, (b) The emission of electrons from the surface of the cathode makes it possible to more sharply focus the electron beam, and (c) In the filament method, the filament is directly suffers from ion bombardment, thus it is likely to burn out. In the bombardment method, since the cathode is disk-shaped, it can work for long periods of time.

In addition, a grid-assembly construction of the filament and W cathode leads to one unit

Table 2 Specifications for JEBG-3000UB.

Maximum output	300 kW(-40 kV,7.5 A)
Accelerating voltage	-40 kV
Electron-beam scan width	+/-500 mm
Scanning coil	Two axes (X,Y) (X and Y orthogonal)
Dynamic focusing lens	Option
Astigmatism correction coil	Option
Corresponding power supply	JEOL JST-300C

Fig.4 Appearance of JEBG-3000UB High Power Electron Beam Source.

High viltage cable — Contains insulating oil.

Beam source evacuation port

Filament
Cathode
Wehnelt
Anode

Illumination system
• Cathode heating by the bombardment method.
• Unit geometry of the filament and cathode (grid assembly) simplifies positioning.

1st lens
Air lock valve
2nd lens

Imaging system
• Electron beam is focused by the 1st and 2nd lenses.

Intermediate chamber evacuation port

Dynamic focusing lens
Astigmatism correction coil
Deflection coils

Scan system
• Foucus shift during scanning is corrected.
• The shape of the electron beam during scanning is corrected.
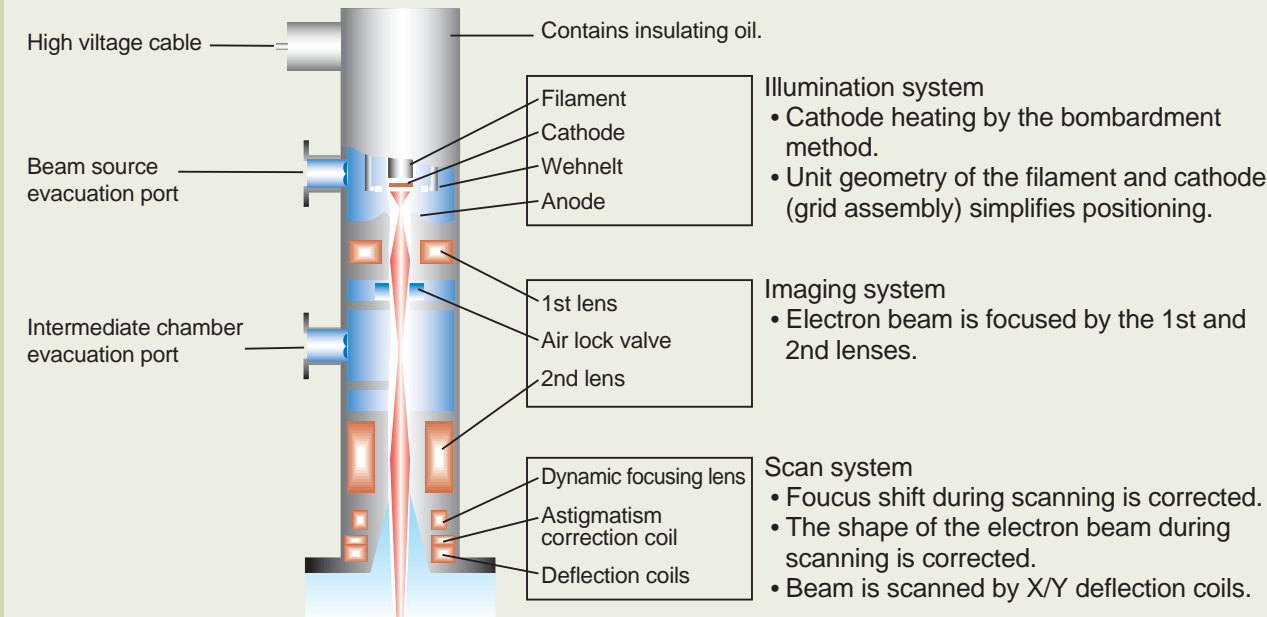• Beam is scanned by X/Y deflection coils.

Fig.5 Electron optional system of High Power Electron Beam Source.

geometry, thus simplifying the positioning and maintenance of the illumination system.

The imaging system has a function to focus the electron beam onto the surface of a material, by means of two lenses of the 1st lens and the 2nd lens.

The scan system performs electron beam scan by means of the X/Y deflection coil. In addition, a dynamic focusing lens and an astigmatism correction coil have functions which respectively correct a focus shift and the shape of the electron beam, during the beam scanning.

Furthermore, the JEBG-3000UB has various scan control parameters to effectively operate as a high power electron beam source. **Figure 6** shows these parameters, including the control parameters for the amplitudes in the X direction (XA), those for the amplitudes in the Y direction (YA), those for rotations in the X and Y directions (X-ROT, Y-ROT), those for dwell time (DT), and those for the beam shape.

Figure 7 shows examples of various scans performed by the JEBG-3000UB, presenting line scan, X-ROT added to line scan, and YA added to line scan. The JEBG-3000UB enables such a variety of scans, making it possible to uniformly dissolve surfaces of materials.

Figure 8 presents the image of applications of the JEBG-3000UB High Power Electron Beam Source to purification of polycrystalline Si materials (P removal).

Conclusion

As described above, the JEBG-3000UB has various features suitable for the production of polycrystalline Si materials. By exploiting these features, it is expected that the JEBG-3000UB will contribute to expanding the applications of solar cells.

References

[1] *Science & Technology Trends*, vol. January 2007, p. 30 (2007) (in Japanese).
[2] *NIKKEI ELECTRONICS*, vol. 2007.6.18, p. 67 (2007) (in Japanese).
[3] NIKKEI INDUSTRY NEWS (newspaper), on March 17, 2008 (2008)   (in Japanese).
[4] *NIKKEI MICRODEVICES*, vol. April 2007, p. 51 (2007) (in Japanese).
[5] SEMICONDUCTOR INDUSTRY NEWS (newspaper), on May 2, 2007 (2007)(in Japanese).
[6] http://www.ostec.or.jp/nmc/TOP/18 (H15.9).pdf (in Japanese).
[7] http://www.nedo.go.jp/kankobutsu/ nedonews/166/1-5.html (in Japanese).
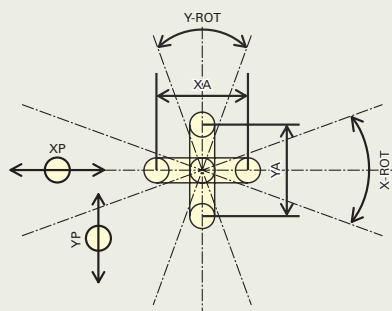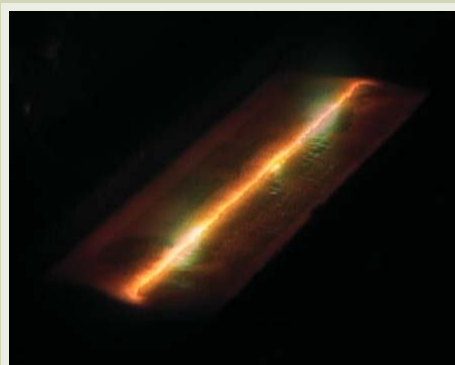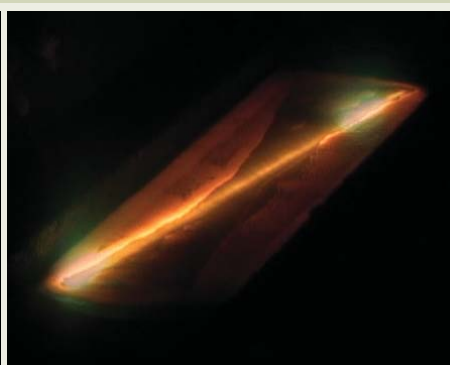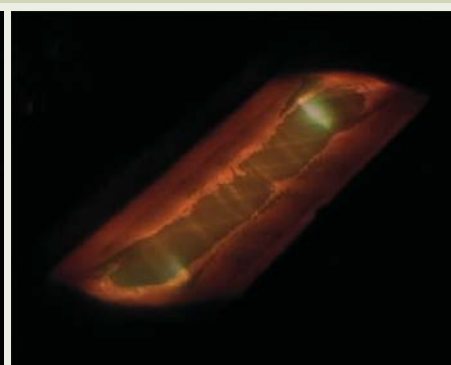[8] JEOL product catalog for High-power Electron Beam Sources and Power Supplies.

Fig.6 Scan control parameters of High Power Electron Beam Source.

Line scan

X-ROT added to Line scan

YA added to Line scan

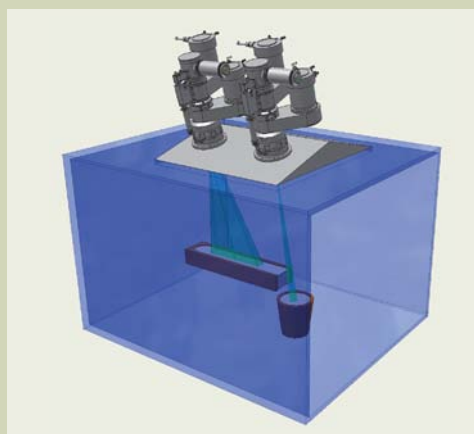Fig.7 Examples of various scans performed by the JEBG-3000UB.

Fig.8 Image of applications of High Power Electron Beam Source to purification of polycrystalline Si materials (P removal).

Introduction of New Products

MultiBeam System
JIB-4600F

The newly developed JIB-4600F MultiBeam System unites the unique imaging and analytical capabilities of the High Power Optics employed in the TFE SEM and a high-performance FIB column in a highly efficient and powerful system. Together with the advanced software developed at JEOL, the JIB-4600F offers an easy-to-use tool for highly automated sample preparation combined with high-resolution imaging and sub-micron analysis of the specimen cross-section.

This tool will help to significantly reduce the time it takes to find the answer for various research and industrial applications requiring materials and defect analysis.

Observation and Analysis

The High Power Optics developed for cross-section nanostructure characterization provides the guaranteed resolution of 1.2 nm at 30 kV, making observation at magnification higher than ×100,000 easily achievable which is important for process monitoring and defect identification.

The JEOL patented High Power Optics is rated to produce a probe current up to 200 nA while maintaining a small probe size. The High Power Optics is suitable for a wide range of applications even at a low accelerating voltage. Under these conditions, the JIB-4600F MultiBeam System can offer enough current even when running the FIB process.

Processing

The newly developed high-performance FIB column achieves high-throughput milling with a beam current of 30 nA at 30 kV, to offer a substantial increase in productivity. It provides a stable and small ion probe even in the high current mode.

The rapid scan mode makes preparation of thin TEM or bulk SEM samples an easy task with high-throughput rough pre-processing. The processing recipe mode offers various settings for process shape, ion beam diameter and ion beam dose at each gas deposition, rough pre-processing and final precise processing.

In addition, the processing recipe helps to guarantee high reproducibility and reliability of results during the preparation of thin TEM samples, making it possible to repeatedly provide specimens having the same shape.

The JIB-4600F offers a three-dimensional reconstruction application called $S^{3\ TM}$ (**S**erial **S**lice and **S**ampling). Based on the unique features of the JEOL 3D system developed for TEM tilt series acquisition and reconstruction, the $S^{3\ TM}$ module provides depth profile images for the sample cross-section in automatic serial processing mode.

SEM image of Cu TEG structure in a semi-conductor
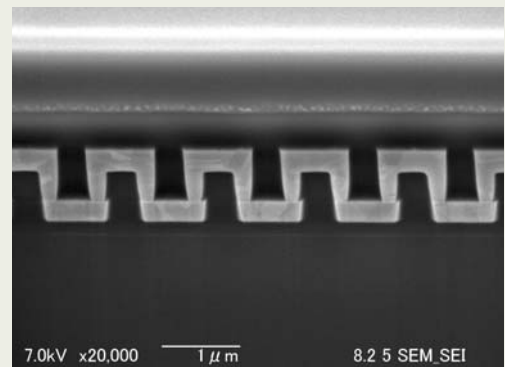
SIM image of Cu TEG structure in a semi-conductor
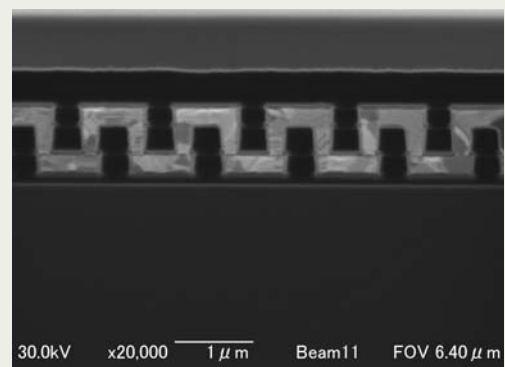
Introduction of New Products

Electron Probe Microanalyzer
JXA-8230

The JXA-8230 is a newly developed Electron Probe Microanalyzer (EPMA). EPMA is an instrument that illuminates the specimen with an accelerated and finely focused electron beam (electron probe), and measures the wavelengths and intensities of characteristic X-rays, as well as the quantities of secondary and backscattered electrons from the specimen. This capability makes it possible to nondestructively analyze the specimen from micro to macro areas, with including constituent elements, concentrations, element distribution, surface morphology and mean atomic number.

The JXA-8230 achieves an integrated control of its various components using a personal computer: wavelength-dispersive X-ray spectrometers (WDS), an energy-dispersive X-ray spectrometer (EDS), an electron optical system, a specimen stage, etc. This sophisticated integration makes the JXA-8230 a state-of-the-art, hybrid EPMA, which enables you to perform measurement utilizing the features of each detector and compile versatile data as analysis results.

Features

Performance improvement in X-ray dispersion

Newly developed analyzing crystals are available. These are effective for very light element analyses and suitable for CHIME (Chemical Th-U-total Pb isochron method) age dating. You can combine these crystals with an optional panchromatic cathodoluminescence detector or an optional CHIME age dating program.

Efficient data acquisition

The JXA-8230 incorporates advanced analysis programs for line analysis and mapping, enabling simultaneous acquisition of electron images (SEI, BEI), WDS (up to five signals) and EDS signals of all detected elements, by means of either electron-probe scanning or specimen-stage scanning. In addition, the JXA-8230 can make use of the "EDS Active Map" function even during simultaneous measurement with multiple WDSs. Furthermore, a combined use with an optional silicon-drift detector (SDD), which requires no liquid nitrogen, enables you to easily perform efficient data acquisition.

Newly designed PC-GUI (graphical user interface)

A series of operations, from observing surface morphology and elemental analysis to data processing and outputting, can be seamlessly performed in a user-friendly personal computer environment. In addition, the new GUI provides "Click Point Analysis" function for starting analysis simply by clicking on a scanning image, and "User recipe" function that enables the creation of a customized recipe for frequently used analytical conditions. With these extensive functions, various operation styles can be chosen according to the level and needs of EPMA users. Highly reliable analysis results are obtainable with easy and efficient operation.

Sophisticated SEM imaging function

Scanning images, such as secondary and backscattered electron images, are displayed in real time with high resolution of 1280×960 pixels, thus enabling you to observe still images in a bright room. In addition, since the operation device and GUI for the JXA-8230 are shared with JEOL FE-SEMs, it is convenient to acquire the skill when you already use an FE-SEM. Furthermore, in the observation of X-ray images, since you can superimpose multiple X-ray images on a scanning image in real time, you can easily search a field of view for analysis (area of interest).

Turbo molecular pump is a standard configuration.

Since a turbo molecular pump is adopted as a main pump, a clean vacuum is obtained and also, operation energy and heat exhausted to the environment can be reduced to a low level.

Introduction of New Products

High Performance Scanning Electron Microscope
-User Friendly SEM-
JSM-6610 Series/JSM-6510 Series

The scanning electron microscope (SEM) is an easy-to-use, fast characterization tool for revealing fine structures of specimens, which cannot be viewed by an optical microscope. In addition, the SEM can rapidly analyze constituent elements in specimens. Thus, the SEM is widely used in all research fields, as well as for industrial applications, ranging from development of new products to quality control. Now, requirement for SEM is much easier operation comparable to optical microscope. To adapt the SEM to versatile applications, JEOL has developed high-performance SEM series that incorporate newly designed software for easier SEM operations.

The JSM-6510 series is equipped with a general-purpose specimen chamber, which enables observation of specimens up to 150 mm in diameter. The JSM-6610 series accommodates a large-specimen chamber and a large specimen stage, for observation of specimens up to 200 mm in diameter.

You can easily search for areas of interest by taking an image of a specimen with a CCD camera and acquiring this color image into stage navigation software. An enlarged CCD image is equivalent to ×1 for the JSM-6610 series, and equivalent to ×2 for the JSM-6510 series. This feature enables you to view wider fields, which are difficult to see with the SEM.

SEM images provide high resolution (several hundreds of times greater than optical microscope), and also, the focal depth of SEM is several tens of times greater than optical microscope. These advantages are suitable for observation of complicated structures, enabling you to easily measure lengths and heights on specimen surfaces.

By installing an energy-dispersive X-ray spectrometer (EDS) in the SEM, you can nondestructively analyze constituent elements in a microarea down to 1 μm size while observing this small area, in a very short time. EDS-embedded analytical scanning electron microscopes (ASEM), —JSM-6510A, JSM-6510LA, JSM-6610A, JSM-6610LA— enable you to efficiently perform overall processes from observation to analysis.

To meet demand for "observation of a nonconductive specimen as it is," low-vacuum SEMs (JSM-6510LV, JSM-6510LA, JSM-6610LV, JSM-6610LA) are available.
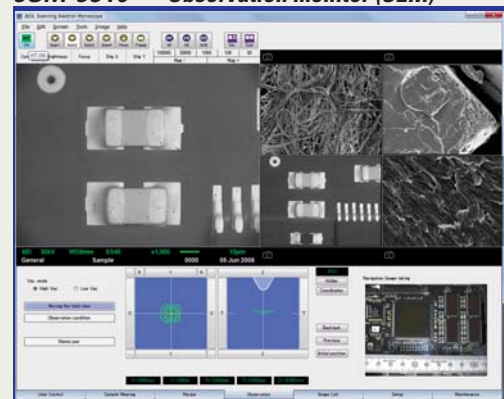
Furthermore, you can easily learn how to maintain the instrument using a video displayed on a SEM monitor screen, for example, the method of replacing a filament. Thus, high performance of the instrument, including a high resolution of 3 nm, can be produced anytime.
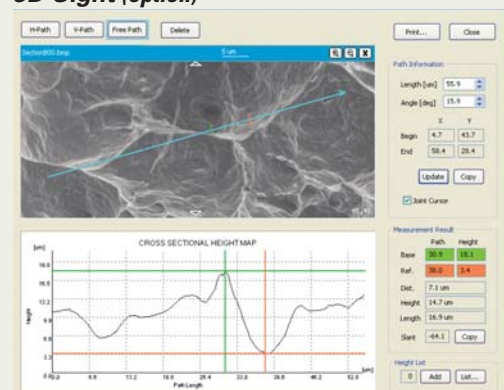

JSM-6610LA

JSM-6510LV

JSM-6610 Observation monitor (SEM)

3D-Sight (option)

Introduction of New Products

Thermal FE SEM
JSM-7600F

The JSM-7600F, a new lineup of JEOL FE-SEM series, is a state-of-the-art thermal FE-SEM that successfully combines ultrahigh-resolution imaging with optimized analytical functionality.
In addition, the JSM-7600F incorporates a large specimen chamber. This uniquely designed chamber, which accommodates a 200 mm diameter specimen, is optimized for a large variety of detectors for secondary electrons, backscattered electrons, EDS, WDS, EBSD, CL, etc.

Features
- Ultrahigh resolution comparable to the cold cathode FE-SEM.
- In-Lens Thermal FEG.
- Aperture angle control lens automatically optimizes the spot size at both high and low currents for both analysis and imaging.
- High probe current up to 200 nA (at 15 kV) for various analytical purposes (WDS, EDS, EBSD, CL, etc.)
- Built-in r-filter enabling user selectable mixture of secondary electron and backscattered electron images.
- Gentle Beam mode for top-surface imaging, reduced beam damage and charge suppression.
- Eco design for energy conservation.

MultiBeam System
JIB-4500

The JIB-4500 MultiBeam System achieves surface/internal 3D imaging and analysis with simple operation. In addition, this innovative system has optimum geometry for all functions from FIB milling, SEM observation to various analyses such as EDS, EBSD and CL.

Features
- Combining a high-resolution LaB_6 SEM and a high-performance FIB.
- Multifunctional specimen chamber.
- High-sensitivity multi-imaging.
- Cross-section preparation for SEM and thin-film preparation for TEM.
- $S^{3 \, TM}$ (**S**erial **S**lice and **S**ampling) for 3D imaging.
- Sophisticated user interface.

JEOL JEOL Ltd.

1-2 Musashino 3-chome Akishima Tokyo 196-8558 Japan   Sales Division ☎(042)528-3381   FAX (042)528-3386

http://www.jeol.com/

ARGENTINA
COASIN S.A.C.I.yF.
Virrey del Pino 4071,
1430 Buenos Aires
Argentina
Telephone: 54-11-4552-3185
Facsimile: 54-11-4555-3321

AUSTRALIA & NEW ZEALAND
JEOL (AUSTRALASIA) Pty. Ltd.
Unit 9, 750-752 Pittwater Road
Brookvale, N.S.W. 2100
Australia
Telephone: 61-2-9905-8255
Facsimile: 61-2-9905-8286

AUSTRIA
LABCO GmbH
Dr.-Tritremmel-Gasse 8,
A-3013 Pressbaum, Austria
Telephone: 43-2233-53838
Facsimile: 43-2233-53176

BANGLADESH
A.Q. CHOWDHURY & CO. Pvt.Ltd.
Baridhara Central Plaza 87,
Suhrawardy Avenue,
2nd Floor Baridhara,
Dhaka-1212, Bangradesh
Telephone: 880-2-9862272, 9894583
Facsimile: 880-2-8854428

BELGIUM
JEOL (EUROPE) B.V.
Planet II, Building B
Leuvensesteenweg 542,
B-1930 Zaventem
Belgium
Telephone:32-2-720-0560
Facsimile:32-2-720-6134

BRAZIL
FUGIWARA ENTERPRISES
INSTRUMENTOS CIENTIFICOS LTDA.
Avenida Itaberaba, 3563
02739-000 Sao Paulo, SPI Brazil
Telephone: 55-11-3983 8144
Facsimile: 55-11-3983 8140

CANADA
JEOL CANADA, INC.
(Represented by Soquelec, Ltd.)
5757 Cavendish Boulevard, Suite 540,
Montreal, Quebec H4W 2W8, Canada
Telephone: 1-514-482-6427
Facsimile: 1-514-482-1929

CHILE
TECSIS LTDA.
Avenida Kennedy 5454 - Piso 5
Vitacura, Santiago, Chile
Telephone: 56-2-401-8520
Facsimile: 56-2-410-8541

CHINA
JEOL LTD., BEIJING OFFICE
Room B1110/11, Wantong New World Plaza
No. 2 Fuchengmenwai Street, Xicheng District,
Beijing 100037, P.R.China
Telephone: 86-10-6804-6321/6322/6323
Facsimile: 86-10-6804-6324

JEOL LTD., SHANGHAI OFFICE
Shanghai Equatorial Hotel Office Building 803,
65 Yanan Road West, Shanghai 200040, P.R. China
Telephone: 86-21-6248-4868/4487/4537/4404
Facsimile: 86-21-6248-4075

JEOL LTD., GUANG ZHOU OFFICE
N3104, World Trade Center Building
371-375, Huan Shi East-Road, Guang Zhou,
510095, P.R.China
Telephone: 86-20-8778-7848
Facsimile: 86-20-8778-4268

JEOL LTD., WUHAN OFFICE
Room 3216, World Trading Bldg.
686 Jiefang Street, Hankou, Wuhan, Hubei 430032
P.R.China
Telephone: 86-27-8544-8953
Facsimile: 86-27-8544-8695

JEOL LTD., CHENGDU OFFICE
1807A Zongfu Building,
NO. 45 Zhongfu Road, Chengdu, Sichuan, 610016
P.R. China
Telephone: 86-28-86622554
Facsimile: 86-28-86622564

CYPRUS
MESLO LTD.
Scientific & Laboraty Division,
P.O. Box 27709, Nicosia Cyprus
Telephone: 357-2-666070
Facsimile: 357-2-660355

EGYPT
JEOL SERIVCE BUREAU
3rd Fl. Nile Center Bldg., Nawal Street,
Dokki, (Cairo) Egypt
Telephone: 20-2-335-7220
Facsimile: 20-2-338-4186

FRANCE
JEOL (EUROPE) SAS
Espace Claude Monet, 1 Allee de Giverny
78290, Croissy-sur-Seine, France
Telephone: 33-13015-3737
Facsimile: 33-13015-3747

GERMANY
JEOL (GERMANY) GmbH
Oskar-Von-Miller-Strasse 1A, 85386
Eching, Germany
Telephone: 49-8165-77346
Facsimile: 49-8165-77512

GREAT BRITAIN & IRELAND
JEOL (U.K.) LTD.
JEOL House, Silver Court, Watchmead,
Welwyn Garden City, Herts AL7 1LT, U.K.
Telephone: 44-1707-377117
Facsimile: 44-1707-373254

GREECE
N. ASTERIADIS S.A.
56-58,S. Trikoupi Str. P.O. Box 26140
GR-10022, Athens, Greece
Telephone: 30-1-823-5383
Facsimile: 30-1-823-9567

HONG KONG
FARMING LTD.
Unit 1009, 10/F., MLC Millennia Plaza
663 King's Road, North Point, Hong Kong
Telephone: 852-2815-7299
Facsimile: 852-2581-4635

INDIA
BLUE STAR LTD. (HQ: Mumbai)
Analytical Instrments Department,
Sahas' 414/2 Veer Savarkar Marg
Prabhadery Mumbai 400 025, India
Telephone: 91-22-6666-4068
Facsimile: 91-22-6666-4001

BLUE STAR LTD. (Delhi)
Analytical Instruments Department,
E-44/12 Okhla Industrial Area,
Phase-II, New Delhi 110 020, India
Telephone: 91-11-4149-4000
Facsimile: 91-11-4149-4005

BLUE STAR LTD. (Calcutta)
Analytical Instruments Department,
7, Hare Street Calcutta 700 001, India
Telephone: 91-33-2213-4133
Facsimile: 91-33-2213-4102

BLUE STAR LTD. (Chennai)
Analyticla Instruments Department,
Garuda Building, 46,
Cathederal Road, Chennai 600 086, India
Telephone: 91-44-4244-4000
Facsimile: 91-44-4244-4190

INDONESIA
PT. TEKNOLABindo Penta Perkasa
Komplek Gading Bukit Indah Blok I/11
Jl. Bukit Gading Raya Kelapa Gading Permai,
Jakarta 14240, Indonesia
Telephone: 62-21-45847057/58/59
Facsimile: 62-21-45842729

ITALY
JEOL (ITALIA) S.p.A.
Centro Direzionale Green Office
Via dei Tulipani, 1
20090 Pieve Emanuele (MI) Italy
Telephone: 39-02-9041431
Facsimile: 39-02-90414343

KOREA
JEOL KOREA LTD.
Dongwoo Bldg. 7F, 458-5, Gil-Dong,
Gangdong-Gu, Seoul, 134-010, Korea
Telephone: 82-2-511-5501
Facsimile: 82-2-511-2635

KUWAIT
YUSUF I.AL-GHANIM&CO.(YIACO)
P.O. Box 435
13005-Safat, Kuwait
Telephone: 965-4832600/4814358
Facsimile: 965-4844954/4833612

MALAYSIA
JEOL(MALAYSIA) SDN.BHD.(359011-M)
205, Block A, Mezzanine Floor,
Kelana Business Center,
97, Jalan SS 7/2, Kelana Jaya,
47301 Petaling Jaya, Selangor, Malaysia
Telephone: 60-3-7492-7722
Facsimile: 60-3-7492-7723

MEXICO
JEOL DE MEXICO S.A. DE C.V.
Av. Amsterdam #46 DEPS. 402
Col Hipodromo, 06100, Mexico D.F.
Mexico
Telephone: 52-5-55-211-4511
Facsimile: 52-5-55-211-0720

PAKISTAN (Karachi)
ANALYTICAL MEASURING SYSTEM (PVT) LTD.(AMS LTD.)
AMS House Plot #14C,
Main Sehar Commercial Avenue,
Commercial Lane 4 Khayaban-Sehar,
D.H.A Phase 7 Karachi, Pakinstan
Telephone: 92-21-5345581/5340747
Facsimile: 92-21-5345582

PANAMA
PROMED S.A.
Parque Industrial Costa del Este
Urbanizacion Costa del Este
Apartado 0816-01755, Panama, Panama
Telephone: 507-303-3100
Facsimile: 507-303-3115

PHILIPPINES
PHILAB INDUSTRIES INC.
7487 Bagtikan Street, SAV Makati,
1203 Metro, Manila Phillippines
Telephone: 63-2-896-7218
Facsimile: 63-2-897-7732

PORTUGAL
Izasa Portugal Lda.
R. do Proletariado, 1
2790-138 CARNAXIDE, Portugal
Telephone: 351-21-424-73-00
Facsimile: 351-21-418-60-20

RUSSIA
JEOL LTD Moscow Office
Pereulok Krasina 16, bld 1. Office 302,
Moscow, Russia
Telephone: 7-495-641-11-14
Facsimile: 7-495-641-28-63

SAUDI ARABIA
ABDULREHMAN ALGOSAIBI G.T.B. (Riyadh)
Algosaibi Bldg., Airport Rd.,
P.O. Box 215, Riyadh 11411, Saudi Arabia
Telephone: 966-1-479-3000
Facsimile: 966-1-477-1374

SCANDINAVIA
JEOL (SKANDINAVISKA) A.B.
Hammarbacken 6A, Box 716, 191 27 Sollentuna
Sweden
Telephone: 46-8-28-2800
Facsimile: 46-8-29-1647

SERVICE & INFORMATION OFFICE
JEOL NORWAY
Ole Deviks vei 28, N-0614 Oslo, Norway
Telephone: 47-2-2-64-7930
Facsimile: 47-2-2-65-0619

JEOL FINLAND
Ylakaupinkuja 2, FIN-02360 Espoo, Finland
Telephone: 358-9-8129-0350
Facsimile: 358-9-8129-0351

JEOL DENMARK
Naverland 2, DK-2600 Glostrup, Denmark
Telephone: 45-4345-3434
Facsimile: 45-4345-3433

SINGAPORE
JEOL ASIA PTE. LTD.
29 International Business Park
#04-02A Acer Building, Tower B
Singapore 609923
Telephone: 65-6565-9989
Facsimile: 65-6565-7552

SOUTH AFRICA
ADI Scientific (Pty) Ltd.
109 Blandford Road, North Riding, Randburg
(PO box 71295 Bryanston 2021)
Republic of South Africa
Telephone: 27-11-462-1363
Facsimile: 27-11-462-1466

SPAIN
IZASA. S.A.
Argoneses, 13, 28100 Alcobendas,
(Poligono Industrial), Madrid, Spain
Telephone: 34-91-663-0500
Facsimile: 34-91-663-0545

SWITZERLAND
JEOL (GERMANY) GmbH
Oskar-Von-Miller Strasse 1,
85386 Eching, Germany
Telephone: 49-8165-77346
Facsimile: 49-8165-77512

TAIWAN
JIE DONG CO., LTD.
7F, 112, Chung Hsiao East Road,
Section 1, Taipei, Taiwan 10023
Republic of China
Telephone: 886-2-2395-2978
Facsimile: 886-2-2322-4655

For Semiconductor Products:
JEOL TAIWAN SEMICONDUCTORS LTD.
11F, No. 346, Pei-Ta Road, Hsin-Chu City 300,
Taiwan, Republic of China
Telephone: 886-3-523-8490
Facsimile: 886-3-523-8503

THAILAND
BECTHAI BANGKOK EQUIPMENT & CHEMICAL CO., Ltd.
300 Phaholyothin Rd. Phayathai, Bangkok 10400,
Thailand
Telephone: 66-2-615-2929
Facsimile: 66-2-615-2350/2351

THE NETHERLANDS
JEOL (EUROPE) B.V.
Lireweg 4, NL-2153 PH Nieuw-Vennep,
The Netherlands
Telephone: 31-252-623500
Facsimile: 31-252-623501

TURKEY
TEKSER LTD.STI.
Acibadem Cad. Erdem Sok, Nº 6/1
34660, Uskudar, Istanbul, Turkey
Telephone: 90-216-3274041
Facsimile: 90-216-3274046

UAE
BUSINESS COMMUNICATIONS LLC. (Abu Dhabi)
P.O. Box 2534, Abu Dhabi UAE
Telephone: 971-2-6348495
Facsimile: 971-2-6316465

BUSINESS COMMUNICATIONS LLC. (Dubai)
P.O. Box 233, Dubai, UAE
Telephone: 971-4-2220186
Facsimile: 971-4-2236193

USA
JEOL USA, INC.
11 Dearborn Road, Peabody, MA 01960, U.S.A.
Telephone: 1-978-535-5900
Facsimile: 1-978-536-2205/2206

JEOL USA, INC. WEST OFFICE
5653 Stoneridge Drive Suite #110
Pleasanton, CA 94588, U.S.A.
Telephone: 1-925-737-1740
Facsimile: 1-925-737-1749

VENEZUELA
GOMSA Service and Supply C.A.
Urbanizacion Montalban III
- Residencias Don Andres - Piso 7 - Apartomento 74
Avenida 3, entre calles 7 y 6
Montalban, Caracas, Venezuela
Telephone: 58-212-443-4342
Facsimile: 58-212-443-4342

VIETNAM
TECHNICAL MATERIALS AND RESOURCES IMPORT-EXPORT JOINT STOCK COMPANY(REXCO)
Hanoi Branch,
157 Lang Ha Road, Dong da District, Hanoi, Vietnam
Telephone: 84-4-562-0516,17/562-0535
Facsimile: 84-4-853-2511